Modeling, Film Formation, and Material Synthesis for Performance Optimization of Mixed Matrix Membranes

A DISSERTATION
SUBMITTED TO THE FACULTY OF THE GRADUATE SCHOOL
OF THE UNIVERSITY OF MINNESOTA
BY

Joshua Alexander Sheffel

IN PARTIAL FULFILLMENT OF THE REQUIREMENTS
FOR THE DEGREE OF
DOCTOR OF PHILOSPHY

Professor Michael Tsapstsis, Advisor

December 2008

Acknowledgements

I have been very fortunate to conduct my graduate research under the direction of Professor Michael Tsapatsis, who I would like to gratefully acknowledge here. The guidance, patience, and good judgment of Michael have enabled me to complete the material presented in this dissertation and have contributed more than anything else to my graduate training.

I would also like to thank those who have worked beside me in the lab and in the classroom during my time as a graduate student. It has been a great honor to spend these years in your company. I would especially like to mention Jungkyu Choi, who I could always count on to stimulate my thinking – about class work, about research, and about life. Jungkyu was always ready with new ideas and a playful outlook; these, and so many other gifts, have made my time in Minneapolis richer. I would also like to thank my classmate, labmate, and officemate Alex Lee, whose unique perspective has been a great challenge and resource during my training. I wish to give thanks to the other members of the Tsapatsis research group as well, past and present, for their help in the lab, conversations about research, and company. Outside our research group, I would like to thank Allison and Anne who, along with Alex, have been my companions for exploring interests that transcend our professional aspirations. Thanks also to the other members of my class here in CEMS – it has been my honor and privilege to study and work with you all.

Abstract

Mixed matrix membranes offer the hope of improving the performance of a separating membrane by dispersing a second phase within it. By combining the processability of a continuous phase (the matrix) with the separation characteristics of a dispersed phase (the flake), mixed matrix membranes aim to provide a step-change improvement in membrane performance without dramatically increasing the cost of membrane technology. In this dissertation, a numerical model for the performance of mixed matrix membranes is presented that accounts for effects such as competitive adsorption and concentration-dependent diffusivities. It is shown that these effects are vital for the modeling of a membrane containing zeolite flakes. This insight is then used to formulate a semi-empirical model for mixed matrix membrane performance that does not require extensive numerical calculations. Through a series of case studies on relevant gas and vapor separations, these models are applied to material and process design for mixed matrix membranes. Finally, experimental aspects of mixed matrix membrane formation are presented, including the synthesis of layered aluminophosphate molecular sieves and the fabrication of mesoporous silica/silicalite-1 zeolite films.

Table of Contents

Chapter 1. Introduction 1

1.1. Mixed Matrix Membranes 1

1.2. Mixed Matrix Membrane Modeling 4

1.3. Outline 6

Chapter 2. A Numerical Model for Mixed Matrix Membrane Performance 8

2.1. Abstract 8

2.2. Introduction and Background 9

2.3. Theory 13

2.4. Results 32

2.5. Discussion 58

2.6. Conclusions 64

Chapter 3. A Semi-empirical Model for Mixed Matrix Membrane Performance 66

3.1. Abstract 66

3.2. Introduction 67

3.3. Theory 69

3.4. Results and Discussion 72

3.5. Conclusions 105

Chapter 4. Inorganic Mixed Matrix Membrane Fabrication 107

4.1. Abstract 107

4.2. Introduction 107

4.3. Experimental 109

4.4. Results and Discussion 114

4.5. Conclusions 126

Chapter 5. Synthesis of layered Aluminophosphates 127

5.1. Abstract 127

5.2. Introduction 127

5.3. Experimental 129

5.4. Results and Discussion 131

5.5. Conclusions 145

Chapter 6. Closing Remarks 146

Appendix A. Derivation of Select Equations 148

Appendix B. Diffusivity of Nitrogen and Methane in Microporous Silica 154

Bibliography 156

List of Tables

Table 2.1: Material properties for microporous silica [71] and clinoptilolite [68]. 35

Table 2.2: Permeabilities of microporous silica and silicalite-1 obtained from Xomeritakis *et. al.* [72] and Lai et. al. [73]. 36

Table 2.3: Summary of the combinations of multicomponent adsorption and diffusion models used in this study. 37

Table 3.1: Dual-site Langmuir adsorption isotherm parameters for normal and isobutane in silicalite-1 [86]. 82

Table 3.2: Normal and iso-butane diffusivity values from the literature. This data was used to construct Figure 3.6. The shaded values were used to model the diffusion of butanes in silicalite-1. 83

Table 3.3: Three-site Langmuir adsorption parameters for carbon dioxide and methane in CHA from [82, 108]. 97

Table 3.4: Diffusion and Reed-Ehrlich parameters for carbon dioxide and methane in CHA from [84]. 97

Table 5.1: Identities and molar amounts for the materials these synthesis studies were based upon. In LAlPO-3, isopropanolamine served as both the SDA and solvent. 130

Table 5.2: Synthesis conditions for the materials that these synthesis studies were based upon. 130

List of Figures

Figure 1.1: Schematic of a mixed matrix membrane.. 2

Figure 2.1: Schematic representation of a mixed matrix membrane. 10

Figure 2.2: One-dimensional microporous membrane. 21

Figure 2.3: Separation factor of a homogeneous membrane obeying Extended Langmuir adsorption as a function of material property, A, for various pressure drop ratios, γ . . 26

Figure 2.4: One-dimensional composite microporous membrane. 27

Figure 2.5: Cussler's Model for diffusion around a flake imbedded in a composite membrane. Assumptions are made in order to reduce an inherently two-dimensional problem to a set of three one-dimensional fluxes. 30

Figure 2.6: Geometry of a mixed-matrix membrane. The membrane is 1μm thick. Each flake is 990 x 33 nm, and the volume fraction of flakes is 0.3. 32

Figure 2.7: 1-dimensional composite membrane. An analytical solution for the species distribution and flux for such a membrane has been derived, and this provides a method for verifying the numerical approach. 33

Figure 2.8: Flux and selectivity predictions for homogeneous, one-dimensional microporous membranes as a function of feed pressure. Feed composition is 50/50 nitrogen/methane, and permeate pressure is zero. 39

Figure 2.9: Adsorption of nitrogen and methane on microporous silica according to the Extended Langmuir model, illustrating that adsorption selectivity is a function of gas phase composition. 41

Figure 2.10: Adsorption selectivity contours for: (a.) microporous silica according to the Extended Langmuir model, (b.) microporous silica according to the Ideal Adsorbed Solution Theory, and (c.) clinoptilite according to Ideal Adsorbed Solution Theory. ... 44

Figure 2.11: Flux and selectivity predictions for homogeneous, one-dimensional microporous membranes as a function of feed pressure. Feed composition is 50/50 nitrogen/methane, and permeate pressure is zero. 48

Figure 2.12: (a.) Flux and (b.) selectivity of a mixed matrix membrane composed of a microporous silica matrix [71] and clinoptilolite flakes [68] as a function of feed pressure according to three different models for multicomponent adsorption: (□) Henry's Law, (◊) Extended Langmuir (Scenario I), and (□) Ideal Adsorbed Solution Theory (Scenario II). 51

Figure 2.13: (a.) Flux and (b.) selectivity of nitrogen and methane as a function of feed pressure for a mixed matrix membrane composed of a microporous silica matrix [71] and clinoptilolite flakes [68]. The feed is 50/50, and the permeate is vacuum. Adsorption is modeled by the Extended Langmuir model, and three different models for the loading dependence of Maxwell-Stefan diffusivities are compared: 53

Figure 2.14: Predictions of Cussler's analytical equation (Equation 2.49) [1] for the performance of a microporous silica/clinoptilolite mixed matrix membrane. 55

Figure 2.15: Predictions of Cussler's analytical equation (Equation 2.49) for the performance of a microporous silica [72] /silicalite [73] mixed matrix membrane for the separation of xylene isomers at 100°C..... 56

Figure 2.16: FEM and analytical predictions of the pressure profile across a one-dimensional clinoptilolite/microporous silica mixed matrix membrane..... 57

Figure 3.1: Comparison of finite element calculations (FEM) and analytical models for the performance of a mixed matrix membrane containing flakes with an aspect ratio of α = 50 and loading of ϕ = 30%..... 74

Figure 3.2: Comparison of finite element calculations (FEM) and analytical models for the performance of a mixed matrix membrane containing flakes with an aspect ratio of α = 1 and loading of ϕ = 30%..... 75

Figure 3.3: Diagram showing the applicability of various analytical models for the performance of mixed matrix membranes as a function of flake aspect ratio and loading. 76

Figure 3.4: Comparison of finite element calculations (FEM) and analytical models for the performance of a mixed matrix membrane containing flakes with an aspect ratio of α = 10 and loading of ϕ = 20%..... 78

Figure 3.5: Permeability of a silicalite-1 membrane to normal- and iso-butane as a function of feed pressure for a 50/50 feed mixture and a 50% pressure drop across the membrane according to the Maxwell-Stefan model. 80

Figure 3.6: Literature values for the diffusion coefficients of normal- and iso-butane in silicalite-1. 81

Figure 3.7: Predictions for the performance of a mixed matrix membrane containing flakes with an aspect ratio of α = 50 and loading of ϕ = 30%. The feed composition is 50/50 and the total feed and permeate pressures are p_t^{feed} = 100 kPa and $p_t^{permeate}$ = 0 kPa. 85

Figure 3.8: Predictions for the performance of a mixed matrix membrane containing flakes with an aspect ratio of α = 5 and loading of ϕ = 30%. The feed composition is 50/50 and the total feed and permeate pressures are p_t^{feed} = 100 kPa and $p_t^{permeate}$ = 0 kPa. 87

Figure 3.9: Predictions for the performance of a mixed matrix membrane containing flakes with an aspect ratio of α = 50 and loading of ϕ = 30%. The feed composition is 50/50 and the total feed and permeate pressures are p_t^{feed} = 1 kPa and $p_t^{permeate}$ = 0 kPa. 89

Figure 3.10: Predictions of the selectivity (P_2^C / P_1^C) of a mixed matrix membrane containing flakes with an aspect ratio of α = 50 and loading of ϕ = 30% as a function of matrix permeability (P_2^M) and selectivity (P_2^M / P_1^M). The feed composition is 50/50 and the total feed and permeate pressures are p_t^{feed} = 100 kPa and $p_t^{permeate}$ = 0 kPa. 92

Figure 3.11: Selectivity ridgelines for a mixed matrix membrane containing flakes with an aspect ratio of α = 50 and loading of ϕ = 30% at various feed pressures for 50/50 feed composition and $p_t^{permeate}$ = 0 kPa according to the Cussler model. 94

Figure 3.12 Predictions of the selectivity (P_2^C / P_1^C) of a mixed matrix membrane containing flakes with an aspect ratio of α = 5 and loading of ϕ = 30% as a function of matrix permeability (P_2^M) and selectivity (P_2^M / P_1^M). The feed composition is 50/50 and the total feed and permeate pressures are p_t^{feed} = 100 kPa and $p_t^{permeate}$ = 0 kPa. 96

Figure 3.13: Calculated permeability of a CHA membrane to carbon dioxide and methane as a function of feed pressure for a 50/50 feed mixture and a 50% pressure drop across the membrane according to the Maxwell-Stefan model. 99

Figure 3.14: Predictions of the CO_2/CH_4 selectivity (P_2^C / P_1^C) of a mixed matrix membrane containing dispersed CHA particles at a loading of ϕ = 15% as a function of matrix permeability (P_2^M) and selectivity (P_2^M / P_1^M). The feed composition is 50/50 CO_2/CH_4 and the total feed and permeate pressures are p_t^{feed} = 448 kPa and $p_t^{permeate}$ = 0 kPa. 101

Figure 3.15: Predictions of the CO_2/CH_4 selectivity (P_2^C / P_1^C) of a mixed matrix membrane containing dispersed CHA particles at a loading of ϕ = 30% and an aspect ratio of α = 30 as a function of matrix permeability (P_2^M) and selectivity (P_2^M / P_1^M). The feed composition is 50/50 CO_2/CH_4 and the total feed and permeate pressures are p_t^{feed} = 10^4 kPa and $p_t^{permeate}$ = 0 kPa. 103

Figure 4.1: Schematic representation of support functionalization with 3-chloropropyltrimethoxysilane. 112

Figure 4.2: Schematic representation of particle deposition by sonication-assisted covalent attachment. 113

Figure 4.3: dC5-silicalite-1 particle layers formed by sonication-assisted covalent attachment under various conditions. 115

Figure 4.4: X-ray diffraction of dC5-silicalite-1 powder and a dC5-silicalite-1-coated support. 116

Figure 4.5: SEM images of silica films deposited by slip coating on top of dC5-silicalite-1 particulate coatings. 118

Figure 4.6: Tilted-view SEM images of a calcined silica film deposited by slip coating on top of a dC5-silicalite-1 particulate coating. 119

Figure 4.7: Permeance (A, C) and selectivity (C, D) of five silica/dC5-silicalite-1 films formed by successive slip coating of silica on top of zeolite particulate films. Open symbols are for *ortho*-xylene and filled symbols are for *para*-xylene. 120

Figure 4.8: SEM images of silica coatings deposited by aerosol deposition on top of dC5-silicalite-1 particulate coatings. 123

Figure 4.9: SEM images of silica films deposited by spray coating on top of dC5-silicalite-1 particulate coatings. 125

Figure 5.1: Normalized powder x-ray diffraction patterns of the products of syntheses based on the recipe for LAlPO-1 and the simulated powder pattern based on the reported single-crystal structure solution for the expected product [143]. 132

Figure 5.2: SEM images of the products of syntheses based on the recipe for LAlPO-1 as a function of reaction time. 133

Figure 5.3: Molar composition (in terms of solvent, SDA, and Al) of synthesis mixtures explored, where the components are those used in the synthesis of LAlPO-2. 135

Figure 5.4: Powder x-ray diffraction patterns of the products of the synthesis mixtures shown in Figure 5.3. The synthesis time of each product at 180°C is given on the plot. The materials are classified as: a.) LAlPO-2, b.) unknown phase, and c.) dense phase. 136

Figure 5.5: Representative SEM images of the products of the syntheses shown in Figure 5.3. The images correspond to the XRD patterns labeled: (a., b.) A, 15 days; (c., d.) L, 2 days; (e.) O, 3 days; and (f.) S, 2 days. 138

Figure 5.6: Powder XRD for the products of syntheses carried out with the LAlPO-3 recipe given in Table 5.1 as a function of synthesis time. 140

Figure 5.7: SEM images of the products synthesized from a mixture corresponding to the LAlPO-3 recipe. Synthesis times are: (a.) 1 day and (b.) 4 days. 140

Figure 5.8: Powder XRD patterns for the products of syntheses based on the LAlPO-3 recipe, but with an isopropanolamine/Al ratio of 25 141

Figure 5.9: SEM images of the products of syntheses based on the LAlPO-3 recipe, but with an isopropanolamine/Al ratio of 25. 142

Figure 5.10: Powder XRD patterns of the products of syntheses based on the LAlPO-3 recipe, but with different isopropanolamine/Al ratios. 143

Figure 5.11: Small angle x-ray scattering from unknown LAlPO-3-related material swollen with CTAB surfactant. Peaks are labeled with their corresponding distances. The peaks are tentatively indexed according to a hexagonal arrangement of cylinders..... 144

Figure B.1: Flux through microporous silica membrane reported by Moon *et al.* [71]. The data of Moon *et al.* is shown by closed symbols, while the dashed lines show a fit to the data that contains flux due to three mechanisms: viscous flow, Knudsen diffusion, and surface diffusion. 155

Chapter 1. Introduction

1.1. Mixed Matrix Membranes

A mixed matrix membrane is a physical barrier that is meant to separate a chemical mixture – for example a mixture of gases, vapors, or liquids – by selective transport of one or more of the mixture components. A mixed matrix membrane differs from other types of separation membranes in its microstructure – a continuous phase in which a second phase has been dispersed. The continuous phase is referred to (somewhat confusingly) as the matrix and I will refer to the dispersed phase as the flake, because high aspect ratio is generally desirable, a fact which will become clear later. The flake should possess performance characteristics (such as selectivity for separating the mixture of interest) that are superior to those of the matrix, and it is dispersed in the matrix in the hope that the resulting mixed matrix membrane will posses some of these superior characteristics. If such a mixed matrix membrane is easier to form than a pure membrane made of the flake material alone, it is superior to both of its most obvious competitors: the matrix, on the basis of performance, and the flake, on the basis of ease of formation. A schematic of a mixed matrix membrane is given in Figure 1.1.

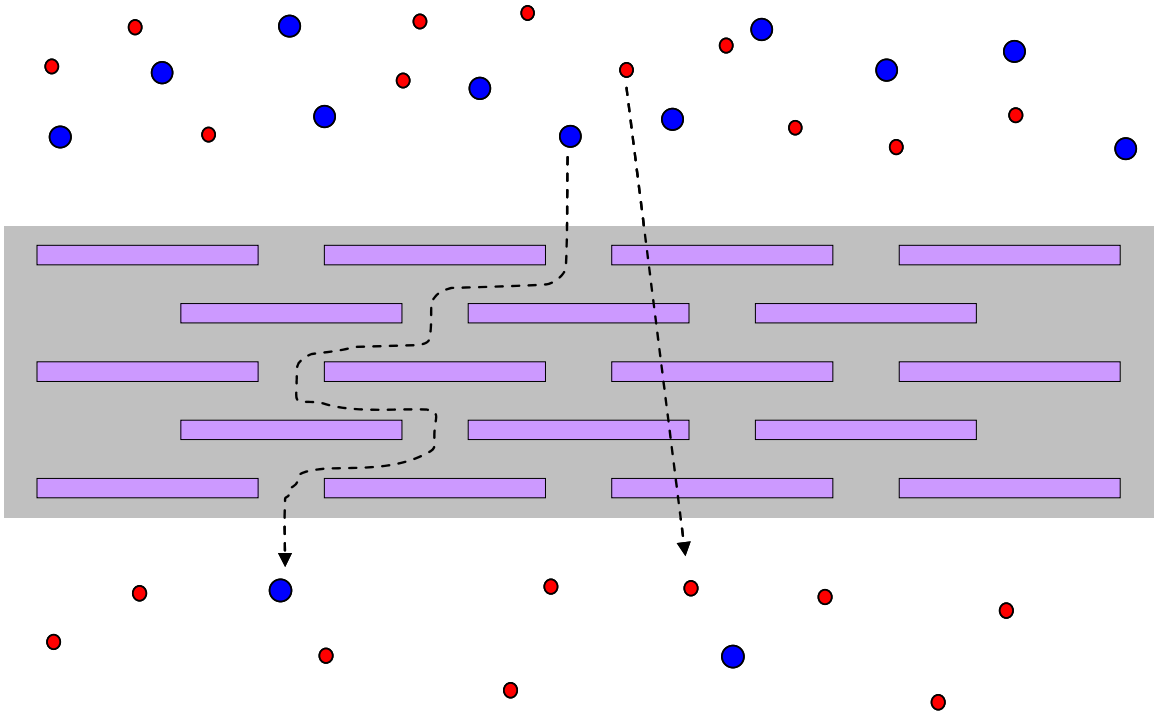

Figure 1.1: Schematic of a mixed matrix membrane.. The dispersed phase is portrayed as a staggered array of flakes which are selectively permeable to the smaller molecule.

The mixed matrix membrane concept has been discussed in the membrane literature for several years [1-4]. Polymer/zeolite composites are a very prominent example of mixed matrix membranes, with several reports available in the literature [5-32]. In this kind of membrane, a highly selective molecular sieve zeolite additive is meant to improve the separation performance of, for instance, a glassy polymer matrix. Other examples include porous inorganic/zeolite membranes where the zeolite again functions as the dispersed phase and an easily processed inorganic material such as amorphous silica or carbon molecular sieve serves as the matrix [33, 34].

Research into mixed matrix membranes has largely focused on polymer/zeolite composites because of the hope that these membranes will provide an in-kind replacement for polymeric gas separation membranes. Though they are the dominant membrane technology for gas separations [35], polymeric membranes suffer from performance limitations that have limited their opportunities for growth in this market.

Specifically, while incremental increases in membrane selectivity and permeability (which determine product gas purity and flow rate, respectively) have been realized through the testing and/or development of new polymeric materials, there appears to be an intrinsic trade-off between these two properties for polymers [36]. Addition of very selective zeolite particles to polymer membranes offers the hope of overcoming this trade-off and delivering the break-though necessary for expanding the market for gas separations by membranes. The incentive for such a break-through is significant, considering that the gas separation membrane market, which was born in 1980, had grown to a $150 million/year business by 2002 [37].

The significant attention drawn by mixed matrix membranes has yielded some progress in terms of selectivity and/or permeability improvements (see the review by Chung *et al.* [38]), but it has also uncovered many challenges. One of these challenges is that the polymer/zeolite mixed matrix membranes reported thus far are not easily formed in the geometries that are most relevant for industrial gas separation by polymer membranes. Asymmetric membranes with very thin selective skins are the most important kind of membrane for industrial gas separations, with hollow fiber membranes being dominant [37]. In these membranes, the selective skin is on the order of 100 nm thick. Most research into mixed matrix membranes for gas separations has focused on the addition of micron-sized zeolite crystals to polymer films, but the use of such large additives is not consistent with ultra-thin asymmetric membrane technology.

In this dissertation, I will present work on materials synthesis aimed at addressing this concern. Layered microporous materials that consist of nanometer-thick sheets containing apertures of several angstroms could provide ultra-thin selective flakes for use in mixed matrix membranes. Layered aluminophosphates are an example of this type of material, and a synthesis study on these materials will be presented, focused on crystal size and shape control.

1.2. Mixed Matrix Membrane Modeling

Besides the numerous experimental challenges to mixed matrix membrane formation – of which flake particle size is only one example – mixed matrix membrane research itself has been greatly hindered by a lack of relevant design heuristics to aid the selection of matrix and flake materials for a desired separation. The requirements mentioned above – that the flake have superior separation characteristics than the matrix and that the mixed matrix membrane be easier to form or apply for the desired separation than a pure membrane of the flake material alone – are necessary but not sufficient criteria for choosing the materials for a successful mixed matrix membrane. It is also necessary to balance the transport properties of the matrix and the flake. If either phase offers too little mass transfer resistance in comparison to the other, the separation performance of the mixed matrix membrane will show no improvement over that of the neat matrix. Though this has been understood for a long time, thanks to early models for diffusion in heterogeneous materials [1, 39-44], it has been largely ignored by experimentalists reporting efforts aimed at mixed matrix membrane fabrication. Moreover, as I will argue in this dissertation, the models that were available up to now for mixed matrix membrane performance prediction are too simplistic to be meaningfully applied to the case of mixed matrix membranes containing zeolite flakes under many circumstances.

These models offer predictions (in the form of an analytical equation) of mixed matrix membrane permeability and selectivity as a function of matrix and flake permeabilities and mixed matrix membrane geometry (flake volume fraction, loading, etc.). They utilize two distinct classes of assumptions. The first class pertains to geometrical approximations that are necessary to render a fundamentally three-dimensional diffusion problem amenable to an analytical solution. The models are generally distinguished from one another by the specific form that these arguments take. The second class of assumptions is related to how the matrix and flake permeabilities are treated as a function of concentration. The available analytical models assume that these permeabilities are constant. While mathematically useful for the formulation of

these expressions, the assumption of concentration-independent permeabilities is not valid in many important cases. Specifically in the case of zeolites, permeability is in general a function of concentration.

The assumption of constant permeabilities poses two problems for modeling mixed matrix membranes containing zeolite flakes. First, as membrane operating conditions (for instance, feed pressure) change, the penetrant concentration within a membrane will also change. Associated changes in flake permeabilities will not be captured by a model that assumes flake permeability is constant. Second, even at constant operating conditions, the concentration seen by any particular flake will be different from that seen by the other flakes in the membrane. Therefore, the flakes in a mixed matrix membrane will be characterized by a range of permeabilities, corresponding to their positions with in the membrane.

This situation calls for a new approach to mixed matrix membrane modeling that realistically treats diffusion in zeolites. The Maxwell-Stefan approach is an established method for zeolite diffusion modeling which is able to capture such effects as concentration-dependent diffusion coefficients and competitive mulitcomponent adsorption phenomena [45-48]. However, use of the Maxwell-Stefan treatment greatly complicates the mathematics of mixed matrix membrane modeling (in comparison to the constant-permeability case) and makes the derivation of analytical solutions tenuous at best and probably impossible. In the face of such obstacles, numerical solutions are useful in as much as they give insight into the effects that concentration-dependent zeolite transport properties can have in the context of mixed matrix membranes. On the other hand, complicated numerical approaches are probably not accessible to most experimentalists who need guidelines for material selection for mixed matrix membrane design.

In this dissertation I present attempts to address both of these concerns. In Chapter 2, a numerical modeling study is presented that, for the first time, applies Maxwell-Stefan diffusion to the modeling of a mixed matrix membrane. Chapter 3

describes a semi-empirical approach that attempts to treat zeolite diffusion in a reasonable way while at the same time avoiding costly numerical calculations.

1.3. Outline

The remainder of this dissertation is divided into four chapters dealing with research, followed by some brief conclusions and comments about future work. Chapters 2 and 3 present two different approaches to mixed matrix membrane modeling, and Chapters 4 and 5 describe experimental efforts related to mixed matrix membranes.

In Chapter 2 I present a fully numerical finite element approach to mixed matrix membrane modeling that utilizes the Maxwell-Stefan approach for diffusion. Competitive adsorption effects are treated by two different models. Likewise, two different functional forms for the dependence of the diffusion coefficients on concentration are explored. The results are compared to simpler models, and the differences, both quantitative and qualitative, are rationalized.

Having demonstrated the importance of realistic transport models to the prediction of mixed matrix membrane performance in Chapter 2, Chapter 3 presents an approach that attempts to make this more accessible to those not wishing to pursue full numerical solutions. This semi-empirical approach combines Maxwell-Stefan calculations of zeolite permeability with analytical approaches for dealing with the mixed matrix geometry. The key to this approach is the calculation of "effective" flake permeabilities that are a function of operating conditions.

In Chapter 4, attempts to fabricate a mesoporous silica/zeolite mixed matrix membrane are documented. These efforts, guided by some of the modeling results, were hampered chiefly by severe cracking of the silica component of the films. Attempts at addressing this are presented. As part of this effort, oriented particulate coatings of very high aspect ratio silicalite-1 zeolite were formed, and these are also described.

Chapter 5 describes experimental attempts to synthesize layered aluminophosphates suitable for use as the selective flakes in mixed matrix membranes. Control of crystal morphology is stressed, and three unknown materials with micron-sized plate-like morphology are reported. Of these, one appears in a mixture with another material and another is of limited crystallinity. The other has been isolated, and its characterization by powder x-ray diffraction, scanning electron microscopy, and elemental analysis is described. Also, swelling of this material with surfactant is described.

Chapter 2. A Numerical Model for Mixed Matrix Membrane Performance[†]

2.1. Abstract

A model for mixed matrix membrane performance is given which utilizes the Maxwell-Stefan formulation for diffusion in microporous materials. Finite element calculations are presented that apply the model to the case of a microporous silica/clinoptilolite zeolite membrane for the separation of nitrogen and methane. In this model, the multicomponent adsorption of nitrogen and methane is predicted by Henry's Law, the Extended Langmuir model, and Ideal Adsorbed Solution Theory. The concentration dependence of the Maxwell-Stefan diffusivities is predicted according to two different limiting cases – facile exchange/weak confinement and non-facile exchange/strong confinement. Also, a finite element calculation is done to predict the performance of a microporous silica/silicalite-1 mixed matrix membrane for the separation of *para*- and *ortho*- xylene in the region of Henry's Law adsorption. The results are compared with an existing analytical model for transport through such membranes. It is found that membrane permselectivity is a function of operating pressure for mixed matrix membranes when adsorption is described by either of the two multicomponent adsorption models, under any of the diffusivity scenarios. The causes of this pressure dependence are explored in terms of adsorption selectivity and the permeability balancing between matrix and flake which is important for mixed matrix membranes. It is shown that inclusion of the more realistic models for adsorption can result in predictions for mixed matrix membrane performance that vary considerably from those given by models that rely only on Henry's Law and constant diffusivity.

[†] Material presented in the chapter is published in:
J.A. Sheffel, M. Tsapatsis, *Journal of Membrane Science*, **295**, 50 (2007).

2.2. Introduction and Background

The concept of improving the performance of a gas separation membrane by dispersing a second phase within it has been discussed in the membrane literature for several years [1-4]. Beginning with a matrix material that is relatively easily processed into a continuous membrane and dispersing within it a small amount of a second material with superior separation characteristics, it is hoped that the resulting composite – a so-called mixed matrix membrane – will include both the processability of the matrix and some of the enhanced performance characteristics of the dispersant. Polymer/zeolite composites are an example of this kind of membrane, of which there are several reports in the literature [5-32] In these membranes, highly selective molecular sieve zeolites are added to polymer films in the hope of overcoming the well-known performance limitations [36] of, for instance, the glassy polymers. Other examples include inorganic/zeolite membranes where the zeolite again functions as the dispersed phase and an easily processed inorganic such as amorphous silica or carbon molecular sieve serves as the matrix [33, 34].

While the suggestion of this kind of membrane technology is by no means young, and even though there has been considerable experimental interest in the fabrication of these kinds of composites, models for predicting the performance of these membranes have scarcely matured past initial, often simplistic efforts. For example, Barrer and Petropoulos offered a model for the performance of mixed matrix membranes [49] that assumes concentration-independent diffusivities and Henry's Law adsorption, and it deals with the inherent two-dimensionality of the situation through the introduction several unknown correction factors. The reliance on such correction factors is one good reason to seek more satisfying treatments; the restrictive assumption of Henry's Law adsorption is another. Perhaps the most popular model for the performance of mixed matrix membranes is based on Maxwell's treatment of the conductivity of a dilute suspension of spheres [15, 39, 43, 50-52]. This model, besides being valid for a restricted geometry, assumes constant permeabilities of the

components in the matrix and flake. Cussler has proposed perhaps the most relevant model by considering a staggered array of high aspect ratio flakes. He reduces the three-dimensional diffusion problem to an essentially one-dimensional problem through a series of approximations [1] and assumes constant Fickian diffusivity. Here I will argue that the latter is a serious limitation, particularly when trying to describe the performance of a composite containing a zeolite phase.

The aspect of mixed matrix membrane modeling we are concerned with here consists of predicting the steady-state species fluxes across a composite membrane of some geometry when it is exposed to a certain set of feed and permeate conditions. The problem is shown schematically in Figure 2.1. Presumably, the feed conditions (total pressure and composition) are known. The permeate conditions could be governed by any physically reasonable situation. In the simplest case, the permeate side of the membrane is maintained at very low pressure or is very efficiently swept by a non-permeating gas, and the permeate partial pressures can be assumed to be zero. Other situations will be discussed later.

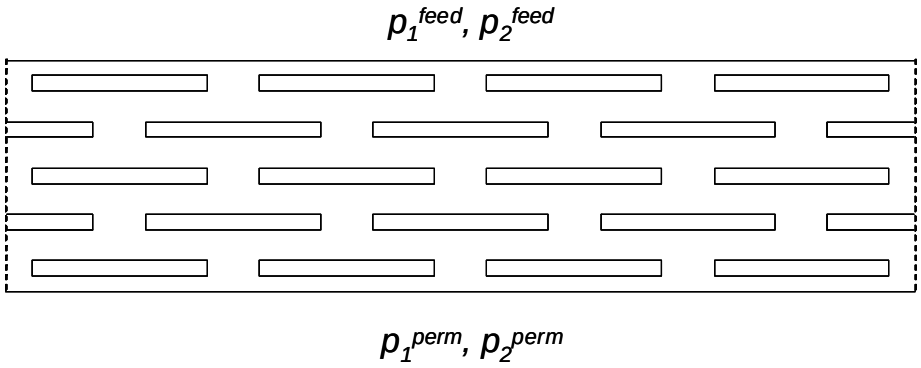

Figure 2.1: Schematic representation of a mixed matrix membrane.

A straightforward approach to solving for the relevant fluxes is to solve the diffusion problem on this domain, obtaining species concentration profiles which can then be integrated across the boundaries to obtain fluxes. Mathematically, this amounts to solving the conservation of mass equation for this non-reactive, steady state system:

$$\underline{\nabla} \bullet \underline{N}_i = 0 \qquad 2.1$$

Obviously, constitutive equations that relate the driving force for diffusion to the diffusive fluxes are needed, and some candidates will be discussed in the theory section. Though straightforward in theory, in practice such an approach is complicated by the two-dimensional, composite geometry of the problem. Even using the simplest constitutive equations, analytical solution of Equation 2.1 for this geometry has not been reported.

Another approach is to make simplifying assumptions about the mixed matrix geometry in order to reach a situation where an analytical solution is possible. This approach has been followed by a number of researchers [1, 40-44]. However, these analytical solutions are not independent of the diffusive constitutive equation assumed in their derivation. That is, a proper set of geometric assumptions *and* the assumption of a particular constitutive equation for diffusion are integral to the derivation of analytical solutions for mixed matrix membrane performance. Without the assumption of a sufficiently simple constitutive equation for diffusion, the geometric assumptions, though they simplify matters significantly in relation to a full two-dimensional approach, are not guaranteed to yield an analytical solution.

This situation poses a problem for the modeling of mixed matrix membranes containing zeolite flakes because for many systems of interest, the constitutive equation for diffusion is significantly more complex than the analytical equations assume. These analytical equations, as they are, are not applicable. A direct replacement of the constitutive equation by a more appropriate one complicates the mathematics so that the derivation of new analytical equations is not possible. This leaves the option of a numerical solution of Equation 2.1 on the mixed matrix membrane domain. Here we present such a treatment. In Chapter 3, a semi-empirical approach is developed, which aims to balance the accessibility and transparency of analytical expressions with the requirements of a reasonable constitutive equation for zeolite diffusion.

The approach presented here relies on the Maxwell-Stefan constitutive equation for diffusion. The Maxwell-Stefan model has been widely applied to the analysis and prediction of diffusive transport within zeolites and other microporous materials [45-48]. It uses chemical potential gradients as the driving force for diffusion, and it contains two different kinds of diffusivities which may have various concentration dependencies. The Maxwell-Stefan equations require a multicomponent adsorption model (or data) in order to express the chemical potential driving force in terms of more experimentally accessible quantities. In principle, any accurate model can be used. Two which are commonly used for zeolites – the Extended Langmuir model and the Ideal Adsorbed Solution Theory – are described in the Theory section and featured in the calculations which follow.

Here we present finite element calculations of mixed matrix membrane performance utilizing the Maxwell-Stefan equations for diffusion in zeolites and two different models for multicomponent adsorption. The values and functionalities of the Maxwell-Stefan diffusivities are predicted according to two different limits which have been relevant for microporous materials. The discussion is facilitated by two case studies of hypothetical mixed-matrix membranes. The results are compared with the predictions of an analytical model developed by Cussler.

2.3. Theory

Constitutive Equations for Diffusion

Diffusive constitutive equations relate diffusive flux to some driving force for diffusion. Fick's Law in its most general form gives diffusive flux of species i in an n-component mixture as the product of concentration-depended diffusion coefficients and the gradients in species concentrations [53]:

$$-\underline{N}_i = \sum_{k=1}^{n-1} D_{ik}^t \left(C_k\right) \underline{\nabla} C_k \tag{2.2}$$

where the D_{ik}^t are $(n-1)$ transport or Fickian diffusivities.

Other constitutive equations assert that chemical potential is a more appropriate driving force for diffusion. Among these are Maxwell-Stefan and Onsager constitutive equations. Because the Maxwell-Stefan approach is often used to describe transport in microporous materials, it will be used in this study.

The Maxwell-Stefan Equations

The Maxwell-Stefan equation for surface diffusion, which is widely used to describe transport in zeolite membranes, is:

$$-\rho \frac{\theta_i}{RT} \underline{\nabla} \mu_i = \sum_{\substack{j=1 \\ i \neq j}}^{n} \frac{q_j \underline{N}_i - q_i \underline{N}_j}{q_i^{sat} q_j^{sat} D_{ij}} + \frac{\underline{N}_i}{q_i^{sat} D_i} \tag{2.3}$$

[48], where q_i is the loading of component i in the zeolite, having units $\left(mol\ i \big/ kg \text{ adsorbent}\right)$, and θ_i is the fractional loading of component i in the zeolite, defined as q_i divided by the loading at saturation:

$$\theta_i \equiv \frac{q_i}{q_i^{sat}} \tag{2.4}$$

The Maxwell-Stefan formulation expresses the driving force for diffusion – a gradient in chemical potential – as a linear combination of the fluxes. In order to express the driving force for diffusion in terms of more accessible quantities, note that:

$$\underline{\nabla}\mu_i = \underline{\nabla}\left(\mu_i^0 + RT \ln f_i\right) \tag{2.5}$$

At moderate pressure:

$$\underline{\nabla}\mu_i \approx RT\underline{\nabla} \ln p_i \tag{2.6}$$

With this substitution, Equation 2.3 becomes:

$$-\rho\frac{\theta_i}{p_i}\underline{\nabla}p_i = \sum_{\substack{j=1 \\ i\neq j}}^{n}\frac{q_j\underline{N}_i - q_i\underline{N}_j}{q_i^{sat}q_j^{sat}D_{ij}} + \frac{\underline{N}_i}{q_i^{sat}D_i} \tag{2.7}$$

Equation 2.7 is conveniently written in matrix form [54], often with loading instead of pressure gradient chosen as the driving force for diffusion. In terms of pressure it is written (for two components):

$$-(N) = \rho\left[q^{sat}\right][B]^{-1}[\Omega](\nabla p) \tag{2.8}$$

Where:

$$\left[q^{sat}\right] = \begin{bmatrix} q_1^{sat} & 0 \\ 0 & q_2^{sat} \end{bmatrix} \tag{2.9}$$

$$[B]^{-1} = \begin{bmatrix} D_1 & 0 \\ 0 & D_2 \end{bmatrix}\begin{bmatrix} 1+\theta_1\frac{D_2}{D_{21}} & \theta_1\frac{D_2}{D_{12}} \\ \theta_2\frac{D_1}{D_{21}} & 1+\theta_2\frac{D_1}{D_{12}} \end{bmatrix}\left(\frac{1}{1+\theta_1\frac{D_2}{D_{21}}+\theta_2\frac{D_1}{D_{12}}}\right) \tag{2.10}$$

$$[\Omega] = \begin{bmatrix} \dfrac{\theta_1}{p_1} & 0 \\ 0 & \dfrac{\theta_2}{p_2} \end{bmatrix} \tag{2.11}$$

The diffusion coefficients contained in the matrix $\underline{\underline{B}}$ are of two kinds. The first, D_i, is associated with the interaction between the adsorbed species i and the zeolite. These diffusivities are known as the Maxwell-Stefan or "corrected" diffusivities. The second, D_{ij}, is associated with the adsorbate-adsorbate interactions in multicomponent diffusion. It embodies "correlation effects" that can arise from zeolite topology anisotropy, sorbate-to-sorbate momentum transfer, and concerted motion of sorbate clusters [55]. It is this diffusion coefficient that gives rise to the "dragging" force that faster-diffusing species can exert on slower-diffusing species and vice versa. In general, both kinds of diffusivities are a function of loading [48].

Extensive molecular dynamics simulations have been done in order to determine the exact dependence of each of these diffusivities on loading [55-61], and the behavior has been found to be highly dependent on the host-guest system. For the current purposes, two limiting cases for the loading dependence of D_i will be used. First, the so-called weak confinement scenario will be adopted. In this limit, the Maxwell-Stefan diffusivity is independent of loading:

$$D_i = D_i(0) \tag{2.12}$$

For cases of strong confinement of the diffusant in the zeolite host, the Maxwell-Stefan diffusivity is seen to decrease strongly with loading. The relation used in this limit is [62-64]:

$$D_i = D_i(0)(1-\theta_1-\theta_2) \tag{2.13}$$

Likewise for the exchange coefficient, two common relations for its dependence on loading will be used. First, the case in which the correlation effects represented by first term on the right of Equation 2.3 are unimportant is considered. In this limit, called facile exchange, D_{ij} is very large:

$$D_{ij} \to \infty \tag{2.14}$$

Second, when correlation effects are significant the following relation, originally suggested by Krishna and Wesselingh [48], will be used to estimate values for D_{ij}:

$$D_{ij} = D_i^{q_i/(q_i+q_j)} D_j^{q_j/(q_i+q_j)} \tag{2.15}$$

Recently, Skoulidas and coworkers have suggested an alternative to Equation 2.15 that provides more quantitative agreement with molecular dynamics simulations in many cases [55]. However, Equation 2.15 will serve our illustrative purposes here, since we are without any data upon which to base a preference for the more complex expression for our current system.

First, the limits represented by Equations 2.12 and 2.14 will be explored. In the limit of weak confinement and facile exchange, Equation 2.8 becomes:

$$-\underline{N}_i = \rho q_{isat} D_i(0) \frac{\theta_i}{p_i} \underline{\nabla} p_i \tag{2.16}$$

Note that in this limit, the diffusion of species i is coupled to that of the other species j through the term θ_i. The fractional loading of species i is a function of the chemical potential (or partial pressure) of all the other species j. The facile exchange limit with loading-independent Maxwell-Stefan diffusivities will serve to isolate the effect of the coupling of the transport through the adsorption isotherms. Later, Equations 2.13 and 2.15 will be employed to explore the effect of loading-dependent diffusivity and correlation effects on membrane performance.

The equation for conservation of all species i for a non-reactive system at steady state is:

$$\underline{\nabla} \bullet \underline{N}_i = 0 \qquad 2.17$$

Along with some relationship between θ_i and p_i, Equations 2.16 and 2.17 can be solved on any domain (with appropriate boundary conditions) to yield both loading profiles and total fluxes.

Models for Multicomponent Adsorption

Ideal Adsorbed Solution Theory

There are a number of models that could be used to obtain the relationship between θ_i and p_i that is necessary for the solution of Equations 2.8 and 2.17. Of these, the Ideal Adsorbed Solution Theory of Myers and Prausnitz [65] presents a thermodynamically consistent way to obtain such a multicomponent adsorption isotherm from single-component adsorption data. The criterion for equilibrium according to Ideal Adsorbed Solution Theory is:

$$\int_{t=0}^{t=p_t y_1 / x_1} q_1(t)\, d\ln t = \int_{t=0}^{t=p_t(1-y_1)/(1-x_1)} q_2(t)\, d\ln t \qquad 2.18$$

where p_t is the total gas phase pressure, y_i is the mole fraction of component i in the gas phase, x_i is the mole fraction of species i in the adsorbed phase $\left(\text{moles } i \text{ adsorbed} / \text{total moles adsorbed}\right)$, and q_i is the single-component adsorption isotherm of component i. Given a bulk gas pressure p_t and composition y_i, Equation 2.18 can be solved to find the adsorbed phase composition x_i. The fractional loadings are given by Equations 2.19a,b, from which it is clear that the total adsorbed amount, q_t, is needed.

$$\theta_1 = \frac{x_1 q_t}{q_1^{sat}} \tag{2.19a}$$

$$\theta_2 = \frac{(1-x_1) q_t}{q_2^{sat}} \tag{2.19b}$$

By assuming no area change upon mixing, it can be shown that [65]:

$$\frac{1}{q_t} = \frac{x_1}{q_1\left(p_t y_1 \big/ x_1\right)} + \frac{(1-x_1)}{q_2\left(p_t (1-y_1) \big/ (1-x_1)\right)} \tag{2.20}$$

where the single-component adsorption isotherms are evaluated at $p_t y_i \big/ x_i$ as indicated.

When the single-component adsorption isotherms can be satisfactorily represented by a Langmuir isotherm, Equations 2.18 - 2.20 become:

$$q_1^{sat} \ln\left(1 + b_1 p_t y_1 \big/ x_1\right) = q_2^{sat} \ln\left(1 + b_2 p_t (1-y_1) \big/ (1-x_1)\right) \tag{2.21a}$$

$$\frac{1}{q_t} = \frac{x_1^2 + b_1 p_t y_1 x_1}{q_1^{sat} b_1 y_1 p_t} + \frac{(1-x_1)^2 + b_2 p_t (1-y_1)(1-x_1)}{q_2^{sat} b_2 (1-y_1) p_t} \tag{2.21b}$$

$$\theta_1 = \frac{x_1 q_t}{q_1^{sat}} \tag{2.21c}$$

$$\theta_2 = \frac{(1-x_1) q_t}{q_2^{sat}} \tag{2.21d}$$

Equations 2.21a-d provide a relationship between the multicomponent fractional loadings, (θ_1, θ_2), and the gas phase partial pressures, (p_1, p_2); all that is required to find the loadings are the single component Langmuir adsorption isotherms, $\{q_i^{sat}, b_i\}$.

This method provides the missing piece necessary for solution of Equations 2.8 and 2.17.

Extended Langmuir Model

While Ideal Adsorbed Solution Theory provides a thermodynamically consistent means for predicting multicomponent adsorption from single component adsorption data, a less rigorous model based on a simple extension of the Langmuir adsorption isotherm has found much use in the literature. Though the Extended Langmuir model is not thermodynamically consistent [66], it does offer the advantage of a simple analytical expression. The Extended Langmuir model for binary adsorption is:

$$\theta_i = \frac{q_i}{q_i^{sat}} = \frac{b_i p_i}{1 + b_1 p_1 + b_2 p_2} \tag{2.22}$$

It can be shown that this model is the special case of the Ideal Adsorbed Solution Theory when $q_i^{sat} = q_j^{sat}$ for all i, j. Along with appropriate boundary conditions, it too can be used to solve Equations 2.16 and 2.17.

Henry's Law

Finally, a useful limit of both the Ideal Adsorbed Solution and Extended Langmuir models is Henry's Law. This is the familiar model that says that the amount of species i adsorbed is directly proportional to the partial pressure of i in the bulk gas.

$$\theta_i = b_i p_i \tag{2.23}$$

From Equation 2.22 it is obvious that this is the low-pressure limit of the Extended Langmuir model. It is the low pressure limit of Ideal Adsorbed Solution Theory as well. When substituted in to Equation 2.16, Henry's Law yields a very simple constitutive equation:

$$-\underline{N}_i = \rho q_i^{sat} D_i b_i \underline{\nabla} p_i \tag{2.24}$$

$$-\underline{N}_i = \rho q_i^{sat} D_i \underline{\nabla} \theta_i \qquad 2.25$$

$$-\underline{N}_i = D_i \underline{\nabla} C_i \qquad 2.26$$

This is Fick's Law with a constant diffusion coefficient.

Model Summary

All of the pieces necessary for the modeling of mixed matrix membranes are now in place. To summarize, Equation 2.8 is the constitutive equation that will be considered in the present work. Along with Equation 2.17, it can be solved to obtain the pressure (or loading) profiles on any geometry, provided appropriate boundary conditions are available. From these profiles, fluxes can be calculated in order to predict performance. However, a model for adsorption and a model for the loading dependence of the two types of Maxwell-Stefan diffusivities are required for complete specification of the problem. Presently, weak confinement and facile exchange expressions (Equations 2.12 and 2.14) will be used along with three different models for adsorption. The adsorption models are: (1) Ideal Adsorbed Solution Theory, (2) the Extended Langmuir model, and (3) Henry's Law. The performance of a mixed-matrix membrane is predicted by solution of Equations 2.16 and 2.17 along with each of these three adsorption models. Then, Equations 2.13 and 2.15 will be used to predict the loading dependence of the Maxwell-Stefan diffusivities, and the Extended Langmuir model will be used for the multicomponent adsorption isotherms. Equations 2.8 and 2.17 will solved to predict the performance of mixed-matrix membranes under these conditions. All of these predictions are compared and discussed in the Results section. First, a few limiting cases for which analytical solutions exist are considered for purposes of model validation.

Limiting Cases: Geometries offering Analytical Solutions

Equations 2.8 and 2.17 can be solved along with either IAST (Equations 2.21-d), Extended Langmuir (Equation 2.22), or Henry's Law (Equation 2.23) adsorption on any

geometry to give a complete description of diffusive transport. The case of a one-dimensional composite with Extended Langmuir adsorption offers the advantage of an analytical solution and will provide a useful check for later numerical solution methods applied to more complex geometries. The case of a homogeneous membrane is reviewed first and then this analysis is extended to a one-dimensional composite.

One-dimensional homogeneous membrane with Extended Langmuir adsorption, weak confinement, and facile exchange

The solution to Equations 2.16, 2.17, and 2.22 for a one-dimensional membrane (Figure 2.2) with Extended Langmuir Adsorption has been worked out by Krishna [64]. The original derivation uses loading as the dependent variable. An equivalent derivation emphasizing pressure begins by writing Equation 2.7 in one dimension and substituting the Extended Langmuir expression (Equation 2.22) for the fractional loading.

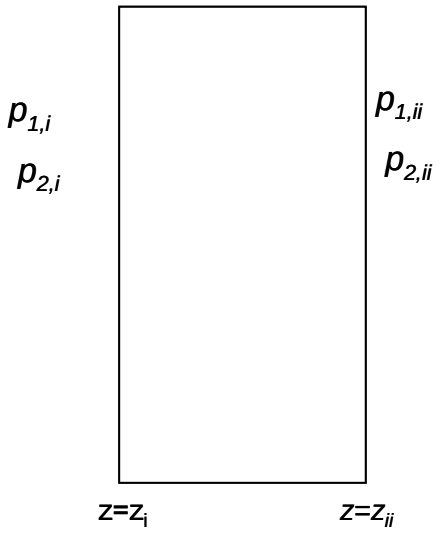

Figure 2.2: One-dimensional microporous membrane. Arabic subscripts denote species, while lowercase roman subscripts denote position. Krishna derived an analytical solution for the species distribution and flux across such a membrane [64] (Equations 2.28,b) using the Extended Langmuir model to describe the multicomponent adsorption.

$$-\rho\frac{b_1}{1+b_1p_1+b_2p_2}\frac{dp_1}{dz}=\frac{N_1}{q_{1sat}D_1} \qquad 2.27a$$

$$-\rho \frac{b_2}{1+b_1 p_1 + b_2 p_2} \frac{dp_2}{dz} = \frac{N_2}{q_{2sat} D_2} \qquad 2.27b$$

Solution of these equations yields the following expression for the flux through a one-dimensional membrane (see Figure 2.2 and Appendix A for details):

$$N_1 = \frac{\rho D_1 q_1^{sat}}{\left(z_{ii} - z_i\right)} \frac{b_1\left(p_{1,ii} - p_{1,i}\right)}{\left(b_1 p_{1,ii} + b_2 p_{2,ii}\right) - \left(b_1 p_{1,i} + b_2 p_{2,i}\right)} \ln\left(\frac{1 + b_1 p_{1,i} + b_2 p_{2,i}}{1 + b_1 p_{1,ii} + b_2 p_{2,ii}}\right) \qquad 2.28a$$

$$N_2 = \frac{\rho D_2 q_2^{sat}}{\left(z_{ii} - z_i\right)} \frac{b_2\left(p_{2,ii} - p_{2,i}\right)}{\left(b_1 p_{1,ii} + b_2 p_{2,ii}\right) - \left(b_1 p_{1,i} + b_2 p_{2,i}\right)} \ln\left(\frac{1 + b_1 p_{1,i} + b_2 p_{2,i}}{1 + b_1 p_{1,ii} + b_2 p_{2,ii}}\right) \qquad 2.28b$$

where Arabic subscripts denote diffusant species and lowercase roman subscripts denote position. The feed is signified by a subscript i, the permeate by ii. Equations 2.28a,b, can be readily applied to the case of a one-dimensional composite membrane (Figure 2.4), but first it will be instructive to examine Equations 2.28a,b more closely in order to obtain an expression for membrane selectivity.

Equations 2.28a,b give the flux in terms of the operating conditions $p_{1,i}, p_{2,i}, p_{1,ii}, p_{2,ii}$. In practice, it is common that, while the total feed pressure and composition are known, the composition of the permeate is determined by the performance of the membrane itself and therefore not known *a priori*. The total permeate pressure is set, but its composition is determined by a mass balance at $z = z_{ii}$. That is, assuming no resistances in the gas phase:

$$p_{1,ii} + p_{2,ii} = p_{t,ii} \qquad 2.29$$

$$\frac{N_1}{N_2} = \frac{p_{1,ii}}{p_{2,ii}} \qquad 2.30$$

Equations 2.28a,b, 2.29, and 2.30 are four equations in four unknowns, $\left(N_1, N_2, p_{1,ii}, p_{2,ii}\right)$. If membrane selectivity (here, flux ratio) is of interest, Equations 2.28a and b can be combined to yield a set of three equations in three unknowns:

$$fr = A\frac{p_{1,ii} - p_{1,i}}{p_{2,ii} - p_{2,i}} \qquad 2.31a$$

$$p_{1,ii} + p_{2,ii} = p_{t,ii} \qquad 2.31b$$

$$fr = \frac{p_{1,ii}}{p_{2,ii}} \qquad 2.31c$$

Where,

$$fr \equiv \frac{N_1}{N_2} \qquad 2.32$$

$$A \equiv \frac{D_1 q_1^{sat} b_1}{D_2 q_2^{sat} b_2} \qquad 2.33$$

For compactness, the feed can be described by:

$$p_{1,i} + p_{2,i} = p_{t,i} \qquad 2.34a$$

$$\beta \equiv \frac{p_{1,i}}{p_{2,i}} \qquad 2.34b$$

Equations 2.31a,b,c and 2.34a,b can be used to eliminate $p_{1,i}, p_{2,i}, p_{1,ii}, p_{2,ii}$ from Equation 2.31a, yielding:

$$fr = A\frac{\frac{fr}{1+fr}p_{t,ii} - \frac{\beta}{1+\beta}p_{t,i}}{\frac{1}{1+fr}p_{t,ii} - \frac{1}{1+\beta}p_{t,i}} \tag{2.35}$$

which is a quadratic equation in fr with one positive solution:

$$fr = \frac{-\left[\frac{1}{1+\beta}p_{t,i} + p_{t,ii}(A-1) - \frac{\beta}{1+\beta}p_{t,i}A\right] + \sqrt{\left[\frac{1}{1+\beta}p_{t,i} + p_{t,ii}(A-1) - \frac{\beta}{1+\beta}p_{t,i}A\right]^2 + 4\frac{\beta}{(1+\beta)^2}p_{t,i}p_{t,i}A}}{\frac{2}{1+\beta}p_{t,i}} \tag{2.36}$$

The quantity fr is the ratio of component fluxes through the membrane (or the ratio of the permeate partial pressures.) Of more interest is the separation factor of the membrane, defined generally as:

$$\alpha \equiv \frac{p_{1,ii}/p_{2,ii}}{p_{1,i}/p_{2,i}} = \frac{fr}{\beta} \tag{2.37}$$

So that, with Equation 2.36, we can write:

$$\alpha = \frac{-\left[\frac{1}{1+\beta} + \gamma(A-1) - \frac{\beta}{1+\beta}A\right] + \sqrt{\left[\frac{1}{1+\beta} + \gamma(A-1) - \frac{\beta}{1+\beta}A\right]^2 + 4\frac{\beta}{(1+\beta)^2}A}}{2\frac{\beta}{1+\beta}} \tag{2.38}$$

where

$$\gamma \equiv \frac{p_{t,ii}}{p_{t,i}} \tag{2.39}$$

In Equation 2.38 we have an analytical expression for the separation factor of a one-dimensional membrane in terms of two operating conditions, (γ, β) and one

material parameter, (A). At constant feed composition (β) and pressure drop ratio (γ), Equation 2.38 shows that separation factor is not a function of operating pressure for a one-dimensional membrane governed by Extended Langmuir adsorption. When a two-dimensional mixed matrix membrane is considered later, it will become clear that, while these three parameters remain important to membrane performance, other variables are needed to completely specify the problem. Specifically, the selectivity of a two-dimensional mixed matrix membrane governed by Extended Langmuir adsorption (as well as Ideal Adsorbed Solution Theory) will be shown to be a function of operating pressure, even under the assumptions of constant β and γ.

Before moving on, it is interesting to note some of the behavior predicted by Equation 2.38 for membrane performance. Figure 2.3 shows how separation factor (α) improves as the material property (A) is improved for various operating conditions (γ) at a given feed composition ($\beta = 1$). As Figure 2.3 shows, for some operating conditions the performance is unbounded as $A \to \infty$, while for others the separation factor approaches some asymptotic value. It can be shown that:

$$\lim_{A\to\infty} \alpha = \begin{cases} \dfrac{1}{\gamma(1+\beta)-\beta} & \text{if} \quad \gamma > \dfrac{\beta}{1+\beta} \\ \infty & \text{if} \quad \gamma \le \dfrac{\beta}{1+\beta} \end{cases} \qquad 2.40$$

Equation 2.40 predicts a limit on membrane performance which is determined by the operating conditions, no matter how good the material properties of the membrane. In cases where operating conditions dictate that separation factor is limited, improvements on the material properties of the membrane will yield vanishing dividends in membrane performance.

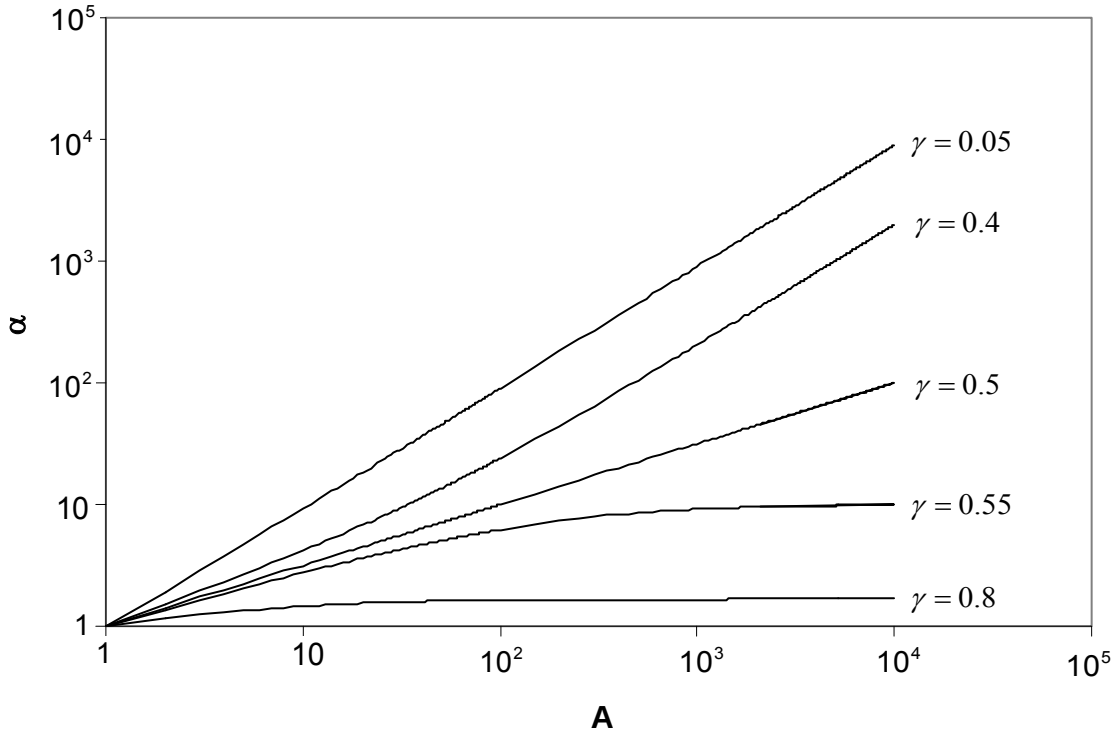

Figure 2.3: Separation factor of a homogeneous membrane obeying Extended Langmuir adsorption as a function of material property, A, for various pressure drop ratios, γ. The feed is a 50/50 mixture ($\beta = 1$). For γ above a certain threshold, the separation factor is limited as $A \to \infty$, while for values of γ below that threshold, the separation factor is unbounded.

Finally, it should be noted that Equations 2.31-c are identical to those that result from a consideration of transport across a membrane governed by Henry's Law adsorption [67] (i.e. from a constant-diffusivity form of Fick's Law). Therefore, the analysis that follows from these equations is equally applicable to both the case of Henry's Law and Extended Langmuir adsorption.

One-dimensional composite membrane with Extended Langmuir adsorption

Figure 2.4 shows a composite membrane consisting of two different materials arranged in series with respect to the direction of transport. The feed side of the membrane ($\text{at } z = z_i$) is in equilibrium with a mixture of gases 1 and 2 at partial

pressures $p_{1,i}$ and $p_{2,i}$, and the permeate side (at $z = z_{iii}$) is in equilibrium with a mixture of the same gases at partial pressures $p_{1,iii}$ and $p_{2,iii}$. The two materials, A and B, are in intimate contact at their interface at $z = z_{ii}$. The criteria for equilibrium at this interface are formulated by requiring that the partial pressure of each component in each phase be equal at this interface. (Partial pressure takes the place of fugacity as the relevant variable here because of the approximation made in Equation 2.6.) Another way of stating this is to say that there is a fictitious gas with composition $p_{1,ii}, p_{2,ii}$ with which both phase A and phase B are in equilibrium at $z = z_i$.

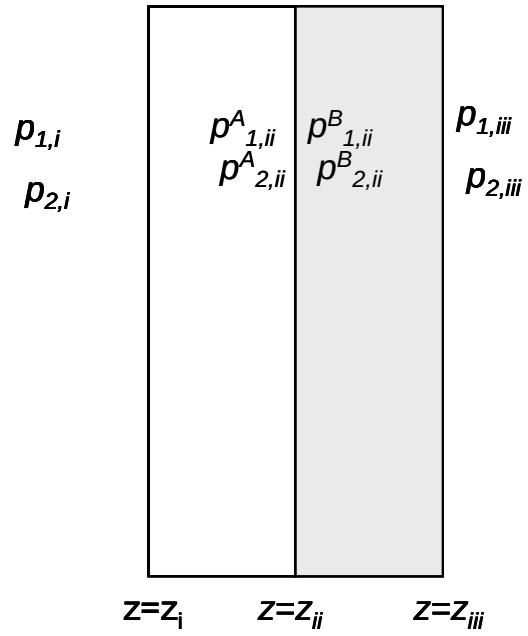

Figure 2.4: One-dimensional composite microporous membrane. An analytical solution for the species distribution and flux across this membrane is given by Equations 2.41 - 2.44 for the case of Extended Langmuir adsorption.

In order to assess the performance of the membrane shown in Figure 2.4, the steady-state flux of each component will be of interest for a given set of feed and permeate conditions. To this end, equations 2.28a,b can be written for each component in each phase of the composite membrane, A and B. That is, we can write for phase A:

$$N_1 = \frac{\rho^A D_1^A q_1^{sat,A}}{\left(z_{ii} - z_i\right)} \frac{b_1^A \left(p_{1,ii} - p_{1,i}\right)}{\left(b_1^A p_{1,ii} + b_2^A p_{2,ii}\right) - \left(b_1^A p_{1,i} + b_2^A p_{2,i}\right)} \ln\left(\frac{1 + b_1^A p_{1,i} + b_2^A p_{2,i}}{1 + b_1^A p_{1,ii} + b_2^A p_{2,ii}}\right) \quad 2.41a$$

$$N_2 = \frac{\rho^A D_2^A q_2^{sat,A}}{\left(z_{ii} - z_i\right)} \frac{b_2^A \left(p_{2,ii} - p_{2,i}\right)}{\left(b_1^A p_{1,ii} + b_2^A p_{2,ii}\right) - \left(b_1^A p_{1,i} + b_2^A p_{2,i}\right)} \ln\left(\frac{1 + b_1^A p_{1,i} + b_2^A p_{2,i}}{1 + b_1^A p_{1,ii} + b_2^A p_{2,ii}}\right) \quad 2.41b$$

and for phase B:

$$N_1 = \frac{\rho^B D_1^B q_1^{sat,B}}{\left(z_{iii} - z_{ii}\right)} \frac{b_1^B \left(p_{1,iii} - p_{1,ii}\right)}{\left(b_1^B p_{1,iii} + b_2^B p_{2,iii}\right) - \left(b_1^B p_{1,ii} + b_2^B p_{2,ii}\right)} \ln\left(\frac{1 + b_1^B p_{1,ii} + b_2^B p_{2,ii}}{1 + b_1^B p_{1,iii} + b_2^B p_{2,iii}}\right) \quad 2.42a$$

$$N_2 = \frac{\rho^B D_2^B q_2^{sat,B}}{\left(z_{iii} - z_{ii}\right)} \frac{b_2^B \left(p_{2,iii} - p_{2,ii}\right)}{\left(b_1^B p_{1,iii} + b_2^B p_{2,iii}\right) - \left(b_1^B p_{1,ii} + b_2^B p_{2,ii}\right)} \ln\left(\frac{1 + b_1^B p_{1,ii} + b_2^B p_{2,ii}}{1 + b_1^B p_{1,iii} + b_2^B p_{2,iii}}\right) \quad 2.42b$$

Assuming that the pressure and composition of the gas on the permeate face of the membrane are known, equations 2.41 and 2.42 are four equations in six unknowns, $\left(N_1, N_2, p_{1,ii}, p_{2,ii}, p_{1,iii}, p_{2,iii}\right)$. Again, it is likely that the total permeate pressure would be known, though its composition would not. That is,

$$p_{1,iii} + p_{2,iii} = p_{t,iii} \quad 2.43$$

A mass balance at $z = z_{ii}$ (assuming no resistances in the gas phase) provides the final relationship necessary for solution of this problem:

$$\frac{N_1}{N_2} = \frac{p_{1,iii}}{p_{2,iii}} \quad 2.44$$

Equation 2.44 states that the composition of the permeate gas is determined by the flux ratio through the composite membrane. Equations 2.41 - 2.44 are six equations in six

unknowns which can be readily solved by an appropriate numerical technique once $\left(p_{1,i}, p_{2,i}, p_{t,iii}\right)$ are specified.

Fick's Law diffusion in a zeolite mixed matrix membrane

A final useful limit of Equation 2.16 is that of Henry's Law adsorption. As has already been mentioned, Henry's Law (Equation 2.23) is the low pressure limit of both the Ideal Adsorbed Solution Theory and the Extended Langmuir model. Also, recall that the use of Henry's Law in Equation 2.16 results in a constitutive equation which is equivalent to the well-known form of Fick's Law with a constant diffusivity (Equations 2.24 - 2.26). That is, in the limit of Henry's Law, Equation 2.16 becomes:

$$-\underline{N}_i = D_i \underline{\nabla} C_i = \rho q_i^{sat} b_i D_i \underline{\nabla} p_i = P_i \underline{\nabla} p_i \qquad 2.45$$

Where the permeability of species i is defined:

$$P_i = \rho q_i^{sat} b_i D_i \qquad 2.46$$

As mentioned in the Introduction, several models for the performance of mixed matrix membranes already exist which are based on Equation 2.45. Of these, one due to Cussler is of particular interest here. Cussler considered diffusion through a staggered array of flakes embedded in a continuous matrix, as shown in Figure 2.1.

Cussler essentially reduced this two-dimensional diffusion problem to a one-dimensional model through a series of approximations. He considered the two-dimensional diffusion in the vicinity of a flake as consisting of three one-dimensional diffusional fluxes: flux through the matrix, through the flake, and around the flake. This is illustrated in Figure 2.5, where these fluxes are denoted N^M, N^W, and N^F, respectively.

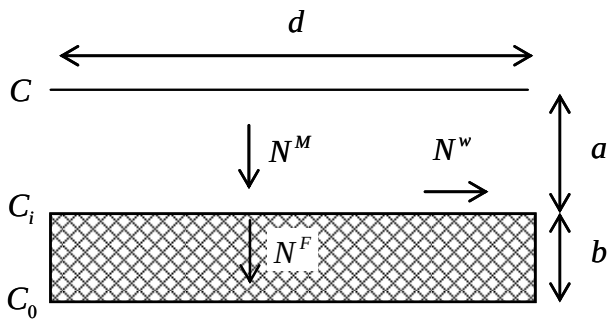

Figure 2.5: Cussler's Model for diffusion around a flake imbedded in a composite membrane. Assumptions are made in order to reduce an inherently two-dimensional problem to a set of three one-dimensional fluxes.

Cussler formulated the problem in terms of a concentration driving force and assumed equal species concentrations at the matrix/flake interface. That is, at the matrix/flake interface it was assumed that:

$$C_i^M = C_i^F \tag{2.47}$$

This is amounts to assuming that the Henry's Law constants in each phase are equal. By considering such a model Cussler arrived at an analytical expression for the selectivity of a mixed matrix membrane as a function of the diffusional and geometrical properties of the matrix and flake. If the less restrictive boundary condition:

$$p_i^M = p_i^F \tag{2.48}$$

is applied at the matrix/flake interface, Cussler's model can be used for materials with different Henry's Law constants. The only change necessary is to replace the diffusion coefficients in Cussler's analytical expression with permeabilities.

$$\frac{N_1}{N_2} = \frac{P_1^M}{P_2^M} \frac{1 + \left(\dfrac{\lambda^2 \phi^2 \Big/ (1-\phi)^2}{1 + \dfrac{\lambda^2 \phi}{P_2^M / P_2^F (1-\phi)}} \right)}{1 + \left(\dfrac{\lambda^2 \phi^2 \Big/ (1-\phi)^2}{1 + \dfrac{\lambda^2 \phi}{P_1^M / P_1^F (1-\phi)}} \right)}$$

where ϕ: volume fraction of flakes in the membrane,

λ: aspect ratio of the flakes, 2.49

P_i^M: permeability of species i in the matrix,

P_i^F: permeability of species i in the flake.

Analysis of this result lead Cussler to conclude that there exists an optimal relationship between the permeabilities of the matrix and flake that would maximize selectivity for a particular membrane geometry. If both permeabilities in the matrix are too high in comparison to the flake, both species are essentially rejected by the flakes. Both species diffuse around the flakes, and membrane performance is dominated by the selectivity of the matrix. On the other hand, if both permeabilities in the flake are too high in comparison to the matrix, neither species is rejected by the flake. No species diffuse around the flake, and membrane performance is again dominated by the selectivity of the matrix.

Because Henry's Law is the low-pressure limit of the more complex adsorption models described above, Cussler's analysis provides a starting point for predicting the low-pressure behavior of membranes obeying these more complex models. In addition, Cussler's analysis provides an encouraging example of the kind of insight that can be gained by carefully considering this kind of composite. Though use of a transport equation that includes a more complete treatment of adsorption greatly complicates the analysis, it is hoped that similarly satisfying insight may be gained from such an endeavor.

2.4. Results

Model Geometry

2-Dimensional mixed matrix membrane

In order to explore the effect of feed pressure on the performance of a mixed matrix membrane, the geometry shown in Figure 2.6 was considered. For this geometry the volume fraction loading of flakes is 0.3 and the flake aspect ratio is 30. The total pressure and composition of the feed and permeate gases were the independent variables in this study. Periodic boundary conditions were applied at the edges of the membrane. That is, the species loadings along the top boundary in Figure 2.6 were made to be equal to those along the bottom boundary at every point, and likewise for the fluxes. These periodic boundary conditions simulate the performance of a membrane that is infinitely wide (in the dimension normal to transport). A careful consideration of the geometry in Figure 2.6 reveals that, by symmetry, no flux is expected through the top and bottom boundaries. Indeed, this a characteristic of all solutions found for this geometry. In this specific case, because of symmetry, periodic and no-flux boundary conditions are both valid.

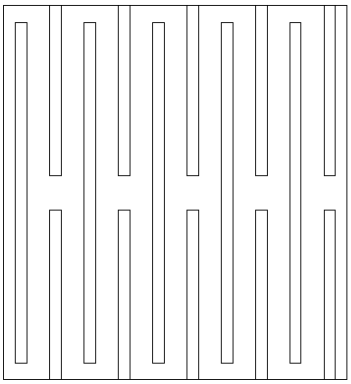

Figure 2.6: Geometry of a mixed-matrix membrane. The membrane is 1μm thick. Each flake is 990 x 33 nm, and the volume fraction of flakes is 0.3.

1-Dimensional composite

In order to confirm the accuracy of the numerical approach, it was compared to the analytical solution for a 1-dimensional composite. This 1-dimensional composite was a 30/70 volume fraction series arrangement of the materials used to construct the 2-dimensional mixed matrix membrane. This geometry is shown is Figure 2.7.

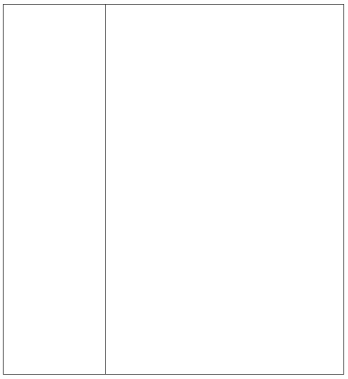

Figure 2.7: 1-dimensional composite membrane. An analytical solution for the species distribution and flux for such a membrane has been derived, and this provides a method for verifying the numerical approach.

Again, the total pressure and composition of the feed gas and the total pressure of the permeate were taken as the independent variables and, for consistency, periodic boundary conditions were applied to boundaries parallel to the direction of diffusion.

Parameter Selection

For the purposes of a case study, adsorption and diffusion data from the literature was sought for two appropriate materials to serve as the matrix and flake in a mixed matrix membrane for a relevant separation. The N_2/CH_4 gas separation was chosen. The zeolite clinoptilolite was chosen as the flake, and relevant parameters for Ce-exchanged clinoptilolite were obtained from the work of Yang and co-workers [68]. The framework of clinoptilolite (a heulandite-type zeolite) consists of parallel 8- and 10- member rings running along the c-direction intersecting with 8-member rings along the a-direction [69]. There are no micropores along the b-direction. Though clinoptilolite exhibits plate-like crystals which would make it well-suited for use in

flake-filled membranes, the b-axis of the crystals is along the thin dimension of the flakes [70]. Therefore, diffusivity selectivity should not be expected for transport normal to the flake faces because there are no micropores in this direction. This is unfortunate, since this is precisely the kind of selectivity desired in a flake-filled composite. Nevertheless, the diffusivity obtained from the literature was applied to the model in an isotropic fashion. Clearly, this is a hypothetical construction that could approximate the behavior of a clinoptilolite plate thin along the a-axis, which has not been reported.

For the matrix, data from Moon and co-workers [71] for TPABr-templated microporous silica was used (for details on how this data was extracted see Appendix B). Organic-templated microporous silicas are amorphous materials prepared by sol-gel methods. The precursor sols contain a silica source and some large organic molecules (such as teterpropylammoniumbromide). After polymerization of the silica network by traditional methods, the organics are calcined out, leaving microvoids in their place. Films of these microporous materials have been explored as an alternative to crystalline zeolite membranes owing to their ease of processability, ability to be easily formed with 20-100 nm thickness, and the tunability of their pore size [72]. In addition to thin films for gas separations, these materials could also be used for "caulking" cracks in polycrystalline zeolite membranes. For the present purposes, microporous amorphous silicas are a class of materials demonstrating Langmuir-type pure component adsorption isotherms for gases of interest and zeolite-like transport that could realistically be envisioned as a matrix material for a composite membrane containing zeolite selective flakes.

Adsorption parameters and diffusivities for the matrix and flake are given in Table 2.1.

Table 2.1: Material properties for microporous silica [71] and clinoptilolite [68].

	N_2				CH_4				
	q_i^{sat}	b_i	D_i	$\rho q_i^{sat} b_i D_i$	q_i^{sat}	b_i	D_i	$\rho q_i^{sat} b_i D_i$	ρ
	(mmol/g)	(1/kPa)	(m^2/s)	(mol/m s kPa)	(mmol/g)	(1/kPa)	(m^2/s)	(mol/m s kPa)	kg/m^3
TPABr Silica (matrix)	0.6631	1.88×10^{-2}	5.37×10^{-14}	1.34×10^{-12}	1.6046	9.66×10^{-3}	1.82×10^{-13}	5.65×10^{-12}	2000
Ce-Clinoptilolite (flake)	0.85	3.48×10^{-2}	8.00×10^{-15}	4.74×10^{-13}	0.93	1.11×10^{-2}	9.80×10^{-17}	2.01×10^{-15}	2000

In addition to the hypothetical microporous silica/clinoptilolite mixed matrix membrane, a mixed matrix membrane containing silicalite-1 flakes dispersed in microporous silica was also considered. Lai and coworkers reported the synthesis of plate-like silicalite-1 with the *b*-channels running along the thin dimension of the crystals as well as xylene permeation data for a defect-free membrane fabricated from such crystals [73]. Xomeritakis and coworkers reported xylene permeation data for a microporous silica membrane capable of separating *para*- and *ortho*-xylene with a selectivity of 18 [72]. From these data, permeabilities were calculated (see Table 2.2) in order to perform a numerical calculation of the performance of a mixed matrix membrane made up of these materials. The results of these calculations were compared to the predictions of Cussler's analytical model.

Table 2.2: Permeabilities of microporous silica and silicalite-1 obtained from Xomeritakis *et al.* [72] and Lai *et al.* [73].

	p-Xylene	o-Xylene
	P_i (mol/m s kPa)	P_i (mol/m s kPa)
TPABr Silica (matrix)	1.5×10^{-11}	8.1×10^{-13}
Silicalite (flake)	2.5×10^{-10}	5.4×10^{-14}

Inherent separation performance of the matrix and flake materials

In order to examine the limits on the performance of a mixed matrix membrane composed of the materials given in Table 2.1, the performance of homogeneous membranes of each material was evaluated for the case of a 50/50 nitrogen/methane feed ($\beta = 1$) and permeate vacuum ($\gamma = 0$). As explained above, two different models for multicomponent adsorption and two scenarios for the concentration-dependence of the Maxwell-Stefan diffusivities will be of interest. The relevant combinations of adsorption and diffusion models are summarized in Table 2.3.

Table 2.3: Summary of the combinations of multicomponent adsorption and diffusion models used in this study.

	Extended Langmuir	Ideal Adsorbed Solution Theory
Weak Confinement $D_i = D_i(0)$ Facile Exchange $D_{ij} \to \infty$	Scenario I	Scenario II
Weak Confinement $D_i = D_i(0)$ Non-facile Exchange $D_{ij} = D_i^{q_i/(q_i+q_j)} D_j^{q_j/(q_i+q_j)}$	Scenario III	
Strong Confinement $D_i = D_i(0)(1-\theta_1-\theta_2)$ Non-facile Exchange $D_{ij} = D_i^{q_i/(q_i+q_j)} D_j^{q_j/(q_i+q_j)}$	Scenario IV	

Membrane Performance for Scenarios I and II

Predictions for the performance of homogeneous microporous silica and clinoptilolite membranes under Scenarios I and II are shown in Figure 2.8. Here, the performance was predicted by solving Equations 2.16 and 2.17 along with both Extended Langmuir and Ideal Adsorbed Solution Theory models for adsorption and weak confinement and facile exchange (Equations 2.12 and 2.14) for the Maxwell-Stefan diffusivities.

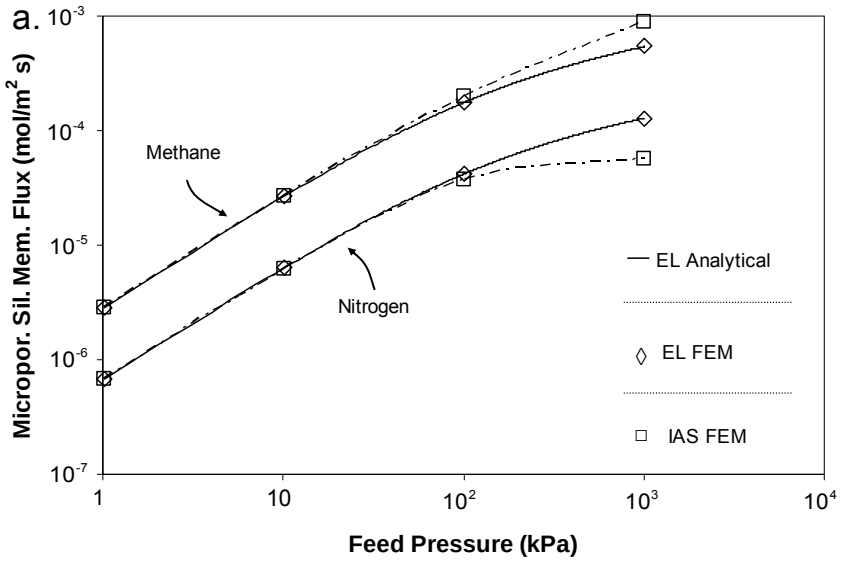
a.
Micropor. Sil. Mem. Flux (mol/m2 s)
10-3
10-4
10-5
10-6
10-7
Methane
Nitrogen
EL Analytical
EL FEM
IAS FEM
1
10
102
103
104
Feed Pressure (kPa)

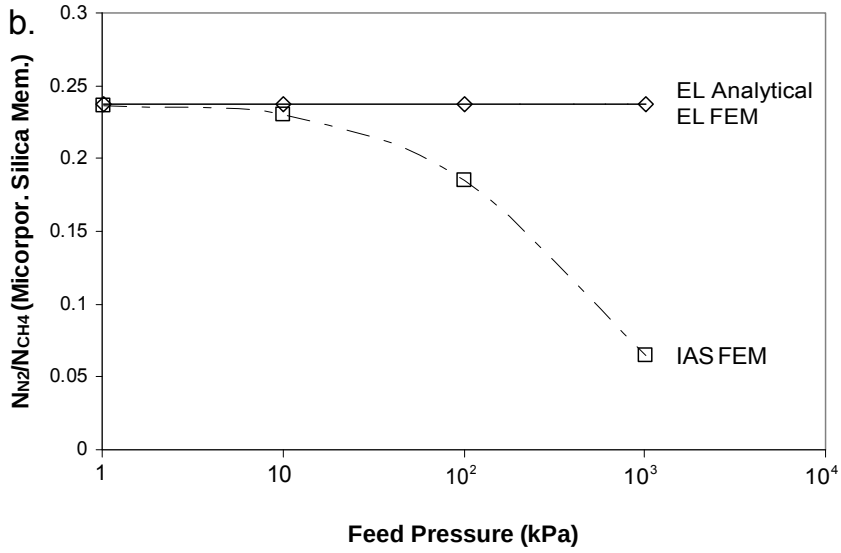
b.
NN2/NCH4 (Micorpor. Silica Mem.)
0.3
0.25
0.2
0.15
0.1
0.05
0
EL Analytical
EL FEM
IAS FEM
1
10
102
103
104
Feed Pressure (kPa)

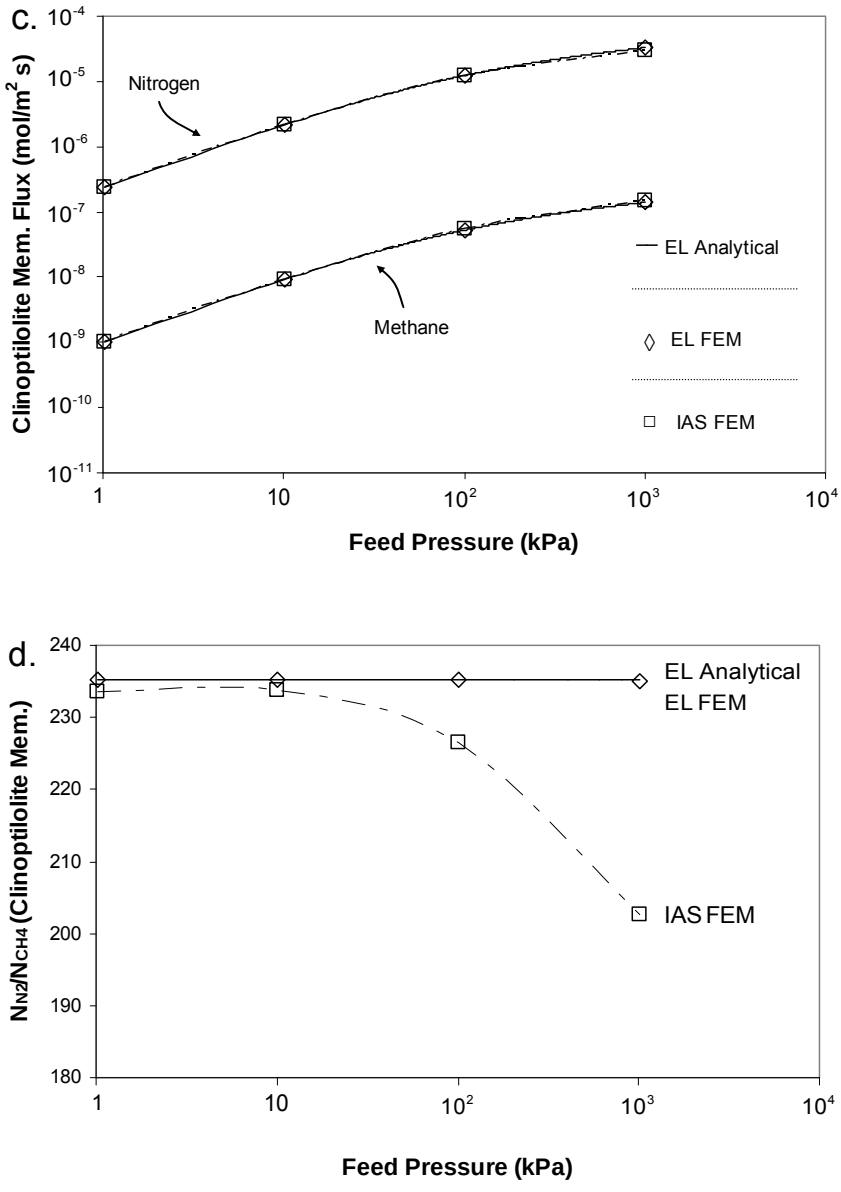

Figure 2.8: Flux and selectivity predictions for homogeneous, one-dimensional microporous membranes as a function of feed pressure. Feed composition is 50/50 nitrogen/methane, and permeate pressure is zero. (—) Analytical solution for a one-dimensional membrane using Extended Langmuir adsorption (Equations 2.28a,b and 2.38), (◊) Finite element solution for a one-dimensional membrane using Extended Langmuir adsorption (Scenario I), (□) Finite element solution for a one-dimensional membrane using Ideal Adsorbed Solution Theory (Scenario II). (a,b.) Predictions for a homogeneous microporous (TPABr-templated) silica membrane. Material properties taken from ref. [71]. (c,d.) Predictions for a homogeneous clinoptilolite membrane. Material properties taken from ref. [68]. (– - –) to guide the eye.

Note that the Extended Langmuir model (Scenario I) does not predict any dependence of selectivity on feed pressure. This is in agreement with Equation 2.38. On the other hand, the Ideal Adsorbed Solution Theory (Scenario II) predicts that the selectivity falls as feed pressure increases for each of these materials. To understand this conflict, it will be instructive to consider the adsorption selectivity predicted by these two adsorption models.

Adsorption selectivity

For the case of two-component adsorption, the adsorption isotherm is represented by a surface – $\theta_i = f\left(p_1, p_2\right)$. The amount adsorbed of each component (here nitrogen and methane) can be represented by such a surface. Depending on the location on the $\left(p_1, p_2\right)$ plane, one gas or the other will be favored by adsorption. This fact – that the adsorption selectivity is a function of bulk phase pressure and composition – is illustrated in Figure 2.9.

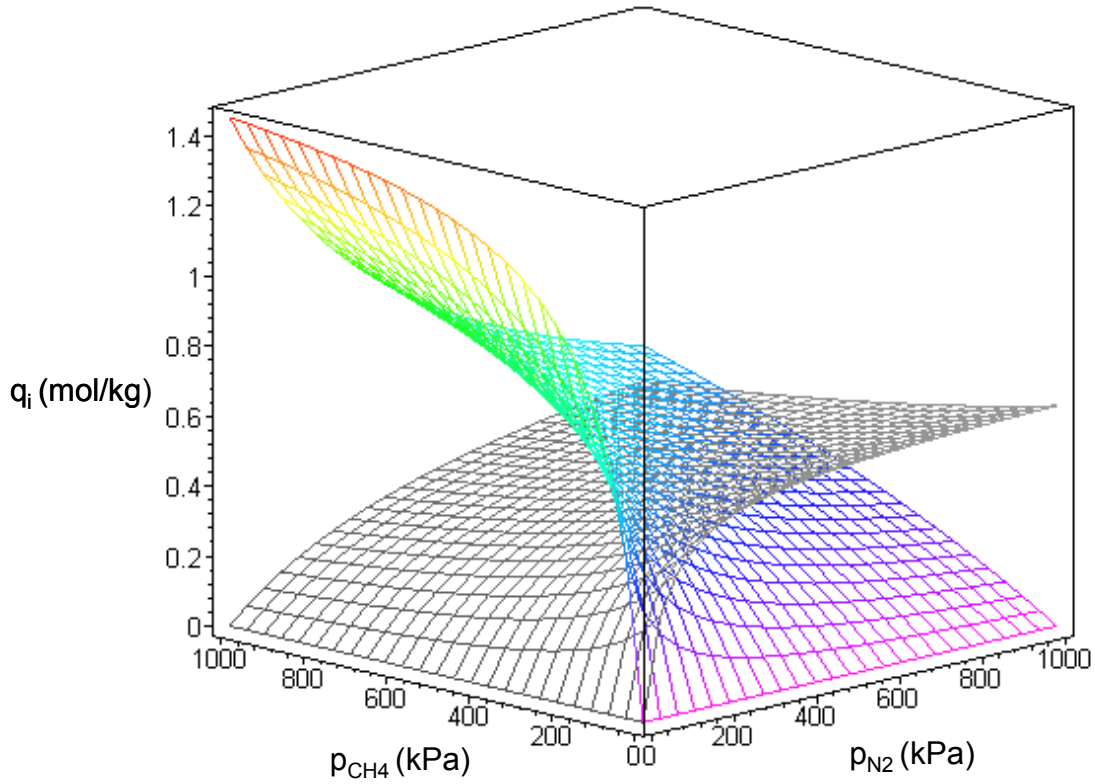

Figure 2.9: Adsorption of nitrogen and methane on microporous silica according to the Extended Langmuir model, illustrating that adsorption selectivity is a function of gas phase composition. The colored surface shows the adsorption of methane and the gray surface that of nitrogen. Material properties for the microporous silica taken from ref. [71]. Because the pressure and composition of the adsorbed phase is a function of location within the membrane, the membrane does not operate at any one specific point on Figure 2.9. Nevertheless, the feed conditions can be considered representative for the purposes of examining trends. That is, we can explore how the adsorption selectivity of the material depends on (feed) pressure.

In order to address this question, we consider the condition at which the amount of N_2 adsorbed is equal to the amount of CH_4 is adsorbed. That is, we seek the composition (at some pressure) for which there is no adsorption selectivity. (Here "selectivity" is used in the most simplistic way – q_1/q_2.) For every value of total pressure ($p_1 + p_2$) there will be one composition for which this is true. According to the Extended Langmuir model for multicomponent adsorption, this is expressed mathematically as:

$$\zeta \equiv \frac{q_1}{q_2} = 1 \tag{2.50}$$

$$\frac{q_1^{sat} b_1 p_1}{1 + b_1 p_1 + b_2 p_2} = \frac{q_2^{sat} b_2 p_2}{1 + b_1 p_1 + b_2 p_2} \tag{2.51}$$

This condition, which corresponds to no adsorption selectivity, is given by Equation 2.52 according to the Extended Langmuir model.

$$p_2 = \frac{q_1^{sat} b_1}{q_2^{sat} b_2} p_1 \tag{2.52}$$

Equation 2.52 is the equation of a line in the (p_1, p_2) plane corresponding to an adsorption selectivity of one. For any value of ζ there exists such a contour line, and some of these are shown in Figure 2.10a for TPABr-templated microporous silica.

$$p_2 = \frac{1}{\zeta} \frac{q_1^{sat} b_1}{q_2^{sat} b_2} p_1 \tag{2.53}$$

From this figure it is clear why the performance of a homogeneous membrane is not a function of pressure according to the Extended Langmuir model when the total feed to total permeate pressure ratio is held constant. As pressure is increased at a given composition, the adsorption selectivity remains constant, a fact that has been observed by Sircar [74]. This is illustrated by the fact that the contours in Figure 2.10a are straight lines.

a.

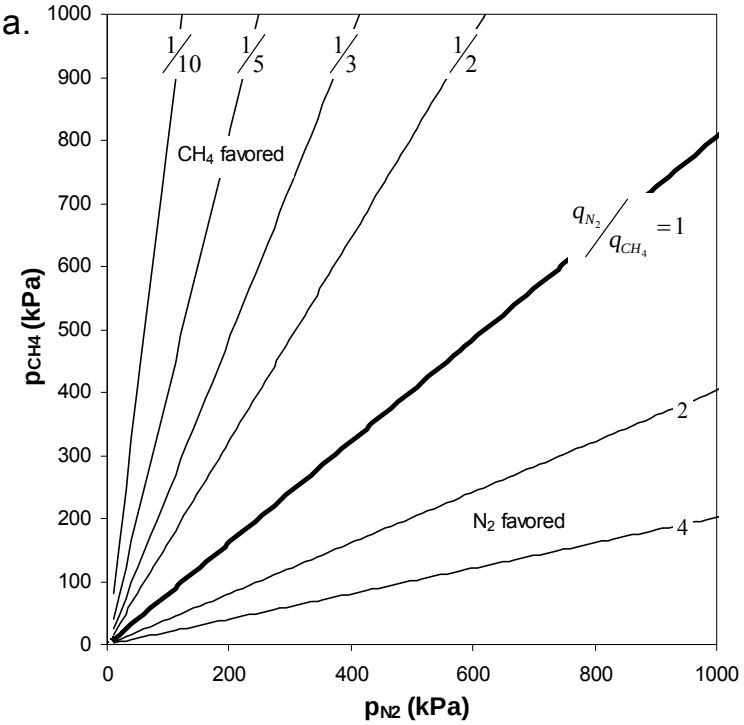
1/10
1/5
1/3
1/2
CH4 favored
$q_{N_2}/q_{CH_4}=1$
2
N2 favored
4
pCH4 (kPa)
pN2 (kPa)
0
100
200
300
400
500
600
700
800
900
1000

b.

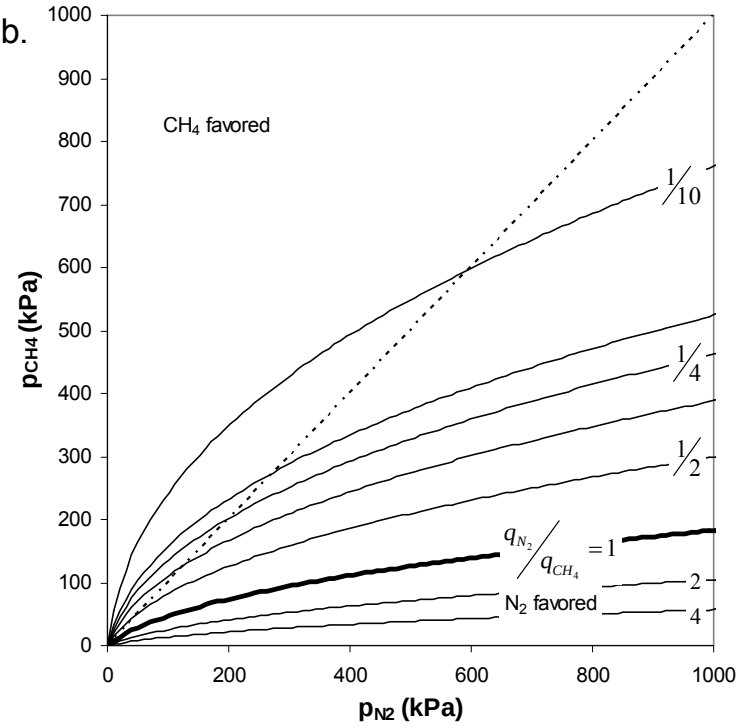
CH4 favored
1/10
1/4
1/2
$q_{N_2}/q_{CH_4}=1$
2
N2 favored
4
pCH4 (kPa)
pN2 (kPa)
0
100
200
300
400
500
600
700
800
900
1000

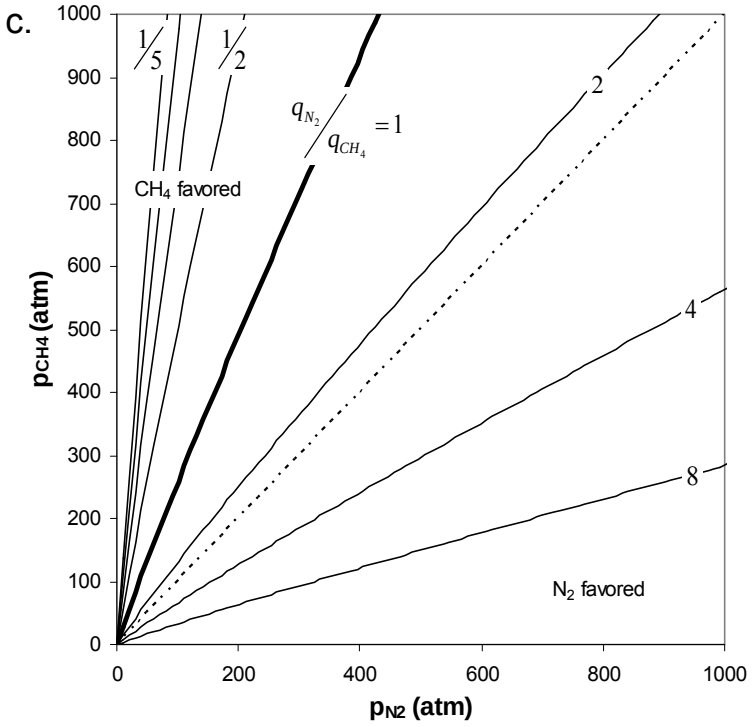

Figure 2.10: Adsorption selectivity contours for: (a.) microporous silica according to the Extended Langmuir model, (b.) microporous silica according to the Ideal Adsorbed Solution Theory, and (c.) clinoptilite according to Ideal Adsorbed Solution Theory. The bold line separates areas in composition space where nitrogen is favored from areas where methane is favored. The dotted line marks the composition of the feed gas considered here (50/50) for reference. The EL model predicts that for a given gas phase composition, adsorption selectivity is independent of total pressure (straight contours), while the IAST predicts a dependence on total pressure (curved contours). Because the saturation loading of nitrogen and methane on clinoptilolite are nearly equal, the adsorption contours in (c.) are nearly straight.

On the other hand, Figure 2.10b illustrates why the Ideal Adsorbed Solution theory predicts falling selectivity as a function of feed pressure. Again, this figure shows contours of constant adsorption selectivity on the $\left(p_1, p_2\right)$ plane. The calculation of these contours is mathematically more complex according to the Ideal Adsorbed Solution theory than for the Extended Langmuir case. It involves solving Equation 2.50 along with Equations 2.21a-d.

From this figure it is clear that adsorption selectivity is a function of total pressure, even as composition is held constant. For instance, as the composition is held constant at 50/50 along the dotted line in Figure 2.10b, the adsorption selectivity changes as contour lines are traversed. For this material, as pressure increases, adsorption selectivity for nitrogen falls. This provides a rationale for understanding why the Ideal Adsorbed Solution model predicts falling membrane selectivity with operating pressure while the Extended Langmuir model predicts pressure-invariant selectivity for constant γ.

Finally, the adsorption selectivity graph for clinoptilolite according to the Ideal Adsorbed Solution Theory is shown in Figure 2.10c. This figure is a good illustration of the agreement between Ideal Adsorbed Solution Theory and the Extended Langmuir model when the saturation loadings of the adsorbents are similar. In the case of clinoptilolite, the saturation loadings are similar ($q_{N_2}^{sat} = 0.85,\ q_{CH_4}^{sat} = 0.93$), and the two models make similar predictions in terms of multicomponent adsorption (note the nearly-straight contours in Figure 2.10c), whereas for the microporous silica considered here, the saturation loadings differ considerably ($q_{N_2}^{sat} = 0.6631,\ q_{CH_4}^{sat} = 1.6046$), and the predictions of IAST and the Extended Langmuir model differ as well. The slight concavity of the adsorption contours explains why the performance of the clinoptilolite membrane in Figure 2.8d falls slightly with increasing pressure.

Membrane performance for Scenarios III and IV

Allowing the Maxwell-Stefan diffusivities to vary with loading and assuming Extended Langmuir adsorption behavior, in accordance with scenarios III and IV, the performance of homogeneous microporous silica and clinoptilolite membranes was predicted. The results of these calculations are shown in Figure 2.11. From these results it is clear that the inclusion of a finite D_{ij} in Scenario III has the effect of slowing down the diffusion of the more mobile species and accelerating the diffusion of the slower species. For instance, in Figure 2.11a it is shown that the flux of methane

decreases and the flux of nitrogen increases for a microporous silica membrane when non-facile exchange (Equation 2.15) is used. Consequently, the microporous silica membrane becomes less selective for methane as pressure increases under Scenario III (Figure 2.11b). The trend for clinoptilolite is similar; the flux of the faster-diffusing nitrogen falls, while the more sluggish methane demonstrates an increase in flux (Figure 2.11c). The net result is that the selectivity of a clinoptilolite membrane for nitrogen falls with increasing pressure when the assumption of facile exchange is replaced by Equation 2.15 (Figure 2.11d).

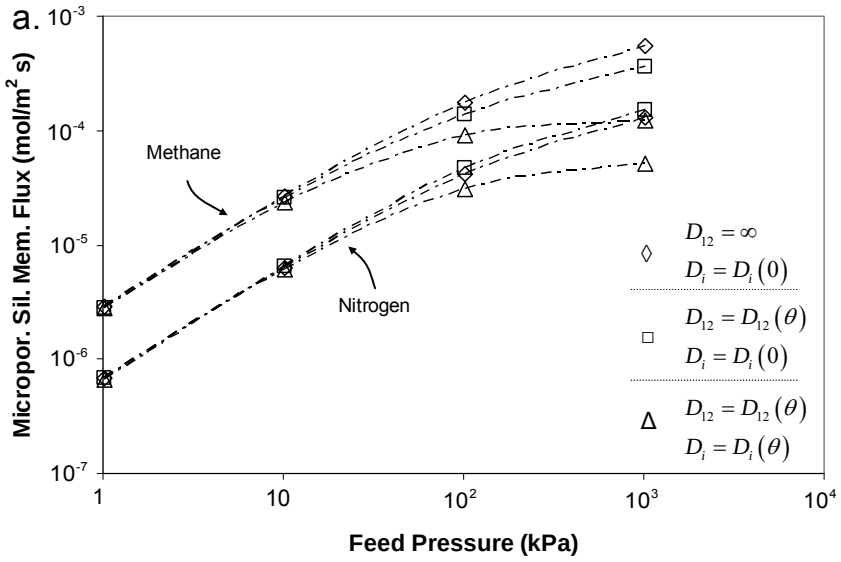
a.
Micropor. Sil. Mem. Flux (mol/m2 s)
10-3
10-4
10-5
10-6
10-7
Methane
Nitrogen
D12 = ∞
Di = Di (0)
D12 = D12 (θ)
Di = Di (0)
D12 = D12 (θ)
Di = Di (θ)
1
10
10²
10³
10⁴
Feed Pressure (kPa)

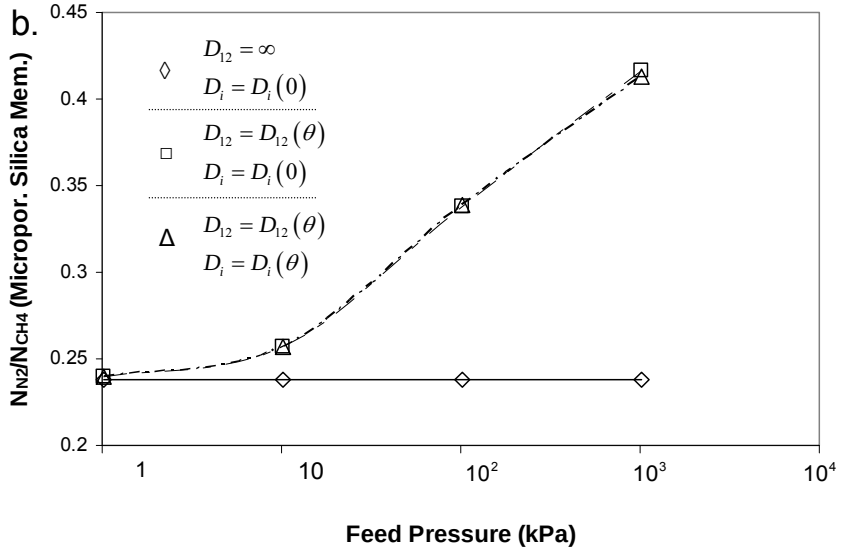
b.
N2/NCH4 (Micropor. Silica Mem.)
0.45
0.4
0.35
0.3
0.25
0.2
D12 = ∞
Di = Di (0)
D12 = D12 (θ)
Di = Di (0)
D12 = D12 (θ)
Di = Di (θ)
1
10
10²
10³
10⁴
Feed Pressure (kPa)

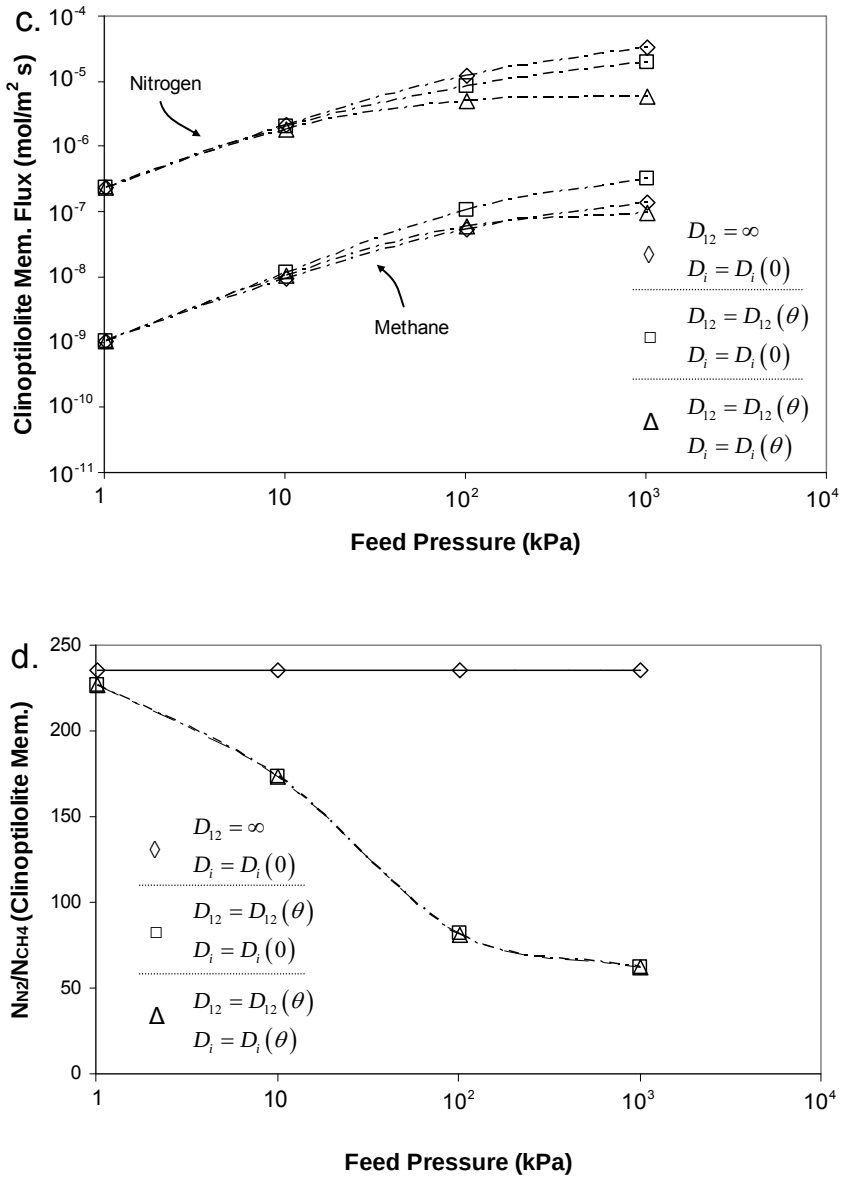

Figure 2.11: Flux and selectivity predictions for homogeneous, one-dimensional microporous membranes as a function of feed pressure. Feed composition is 50/50 nitrogen/methane, and permeate pressure is zero. Finite element solutions for a one-dimensional membrane using Extended Langmuir adsorption assuming: (◊) Weak confinement and facile exchange (Equations 2.12 and 2.14, Scenario I), (□) Weak confinement and Equation 2.15 for D_{ij} (Scenario III), and (Δ) Equation 2.13 for D_i and Equation 2.15 for D_{ij} (Scenario IV). (a,b.) Predictions for a homogeneous microporous (TPABr-templated) silica membrane. Material properties taken from ref. [71]. (c.d.) Predictions for a homogeneous clinoptilolite membrane. Material properties taken from ref. [68]. (– - –) to guide the eye.

The additional inclusion of a D_i that falls strongly with increased loading (Scenario IV) suppresses the flux of both components equally. Figures 2.11a,c show that the flux of each component falls when Equation 2.13 is added to the model. Figures 2.11b,d show that this decrease in flux is not accompanied by a change in selectivity (relative to Scenario III – non-facile exchange and weak confinement) for either homogeneous membrane.

2-Dimensional Membrane

Membrane performance for Scenarios I and II

To explore the effect of operating pressure on the performance of a mixed matrix membrane under Scenarios I and II (weak confinement and facile exchange – Equations 2.12 and 2.14) with the geometry shown in Figure 2.6 and the material properties given in Table 2.1, Equations 2.16 and 2.17 were solved by the method of finite elements using IAST, EL, and Henry's Law models for adsorption. The total pressure of a 50/50 binary mixture of nitrogen and methane was varied between 1.01325 and 1.01325 x 10^4 kPa for the feed. The model was solved for total permeate side pressures of 0, 1% and 10% of the total feed pressure. When a non-zero permeate pressure was applied, a consistent solution was sought in terms of species flux and permeate composition. That is, Equations 2.54 and 2.55 were enforced.

$$\frac{N_1}{N_2} = \frac{p_1^{permeate}}{p_2^{permeate}} \tag{2.54}$$

$$p_1^{permeate} + p_2^{permeate} = p_t^{permeate} \tag{2.55}$$

Once the pressure distribution was determined on the domain of the membrane, Equation 2.7 was integrated across either the feed or permeate boundary in order to obtain the species fluxes. The integration should, and did, yield the same result no matter which boundary was integrated. The results of these calculations are shown in Figure 2.12a. At low feed pressure, the flux increases linearly with pressure, but at

higher pressures this dependence falls off for both the IAST and EL models. The selectivity of the mixed matrix membrane is a function of pressure for the more complex adsorption models, as shown in Figure 2.12b. Three trends are obvious from these results: (1) The selectivity of this particular membrane falls as feed pressure is increased. This is true not only according to the Ideal Adsorbed Solution theory, which predicts a severe deterioration in the selectivity of the matrix as pressure is increased (cf. Figure 2.8), but also for the Extended Langmuir model, which predicts no change in the inherent selectivity of either phase as a function of pressure (cf. Equation 2.38 and Figure 2.8); (2) This effect is more severe according to the predictions of the Ideal Adsorbed Solution Theory model than according Extended Langmuir model; (3) An elevated permeate pressure has the effect of suppressing overall membrane selectivity. The Henry's Law model, which predicts no change in either the adsorption isotherm or the diffusion coefficient with pressure, predicts no dependence of selectivity on pressure.

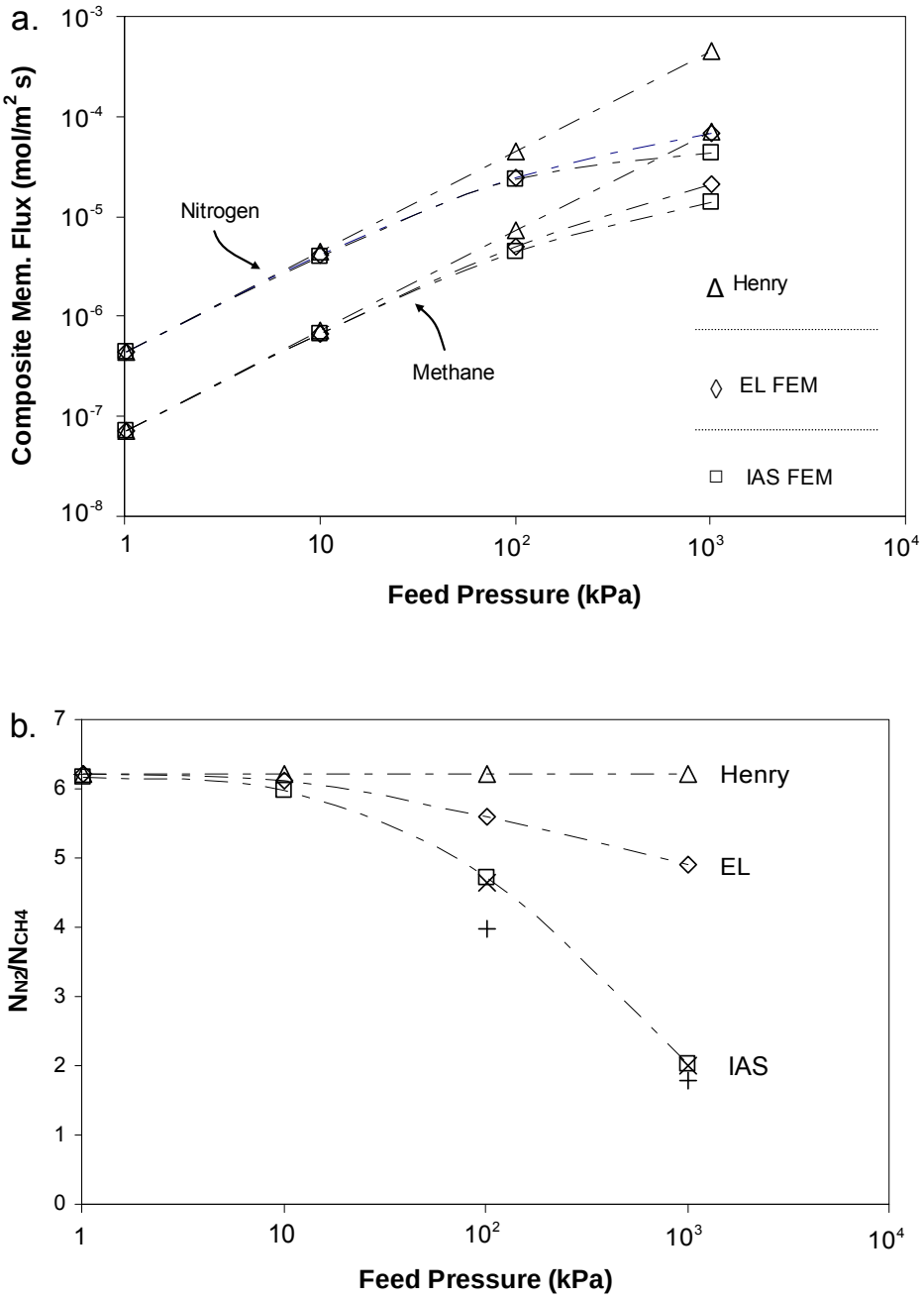

Figure 2.12: (a.) Flux and (b.) selectivity of a mixed matrix membrane composed of a microporous silica matrix [71] and clinoptilolite flakes [68] as a function of feed pressure according to three different models for multicomponent adsorption: (□) Henry's Law, (◊) Extended Langmuir (Scenario I), and (□) Ideal Adsorbed Solution Theory (Scenario II). The feed is 50/50 nitrogen/methane. (x) corresponds to $p_{permeate} = 0.01p_{feed}$, and (+) corresponds to to $p_{permeate} = 0.1p_{feed}$. All other points are for permeate vacuum.

Membrane performance for Scenarios III and IV

The effect of loading-dependent diffusivities on the performance of a microporous silica/clinoptilolite mixed matrix membrane was explored by solving Equations 2.8 and 2.17 along with the Extended Langmuir model for adsorption (Equation 2.22) and Equations 2.13 and 2.15 for the Maxwell-Stefan diffusivities (i.e., Scenarios III and IV). Again, the feed pressure of a 50/50 nitrogen/methane mixture was varied between 1.01325 and 1.01325 x 10^4 kPa. The permeate pressure was zero. The results of these calculations are given in Figure 2.13. The effect of loading-dependent diffusivities is to lower the selectivity of the mixed-matrix membrane considered here. Note that the selectivity of the mixed matrix membrane under Scenario IV is less than the selectivity under Scenario III. This is true even though there is no difference between the inherent selectivies predicted by Scenarios III and IV for the matrix or the flake (cf. Figure 2.11).

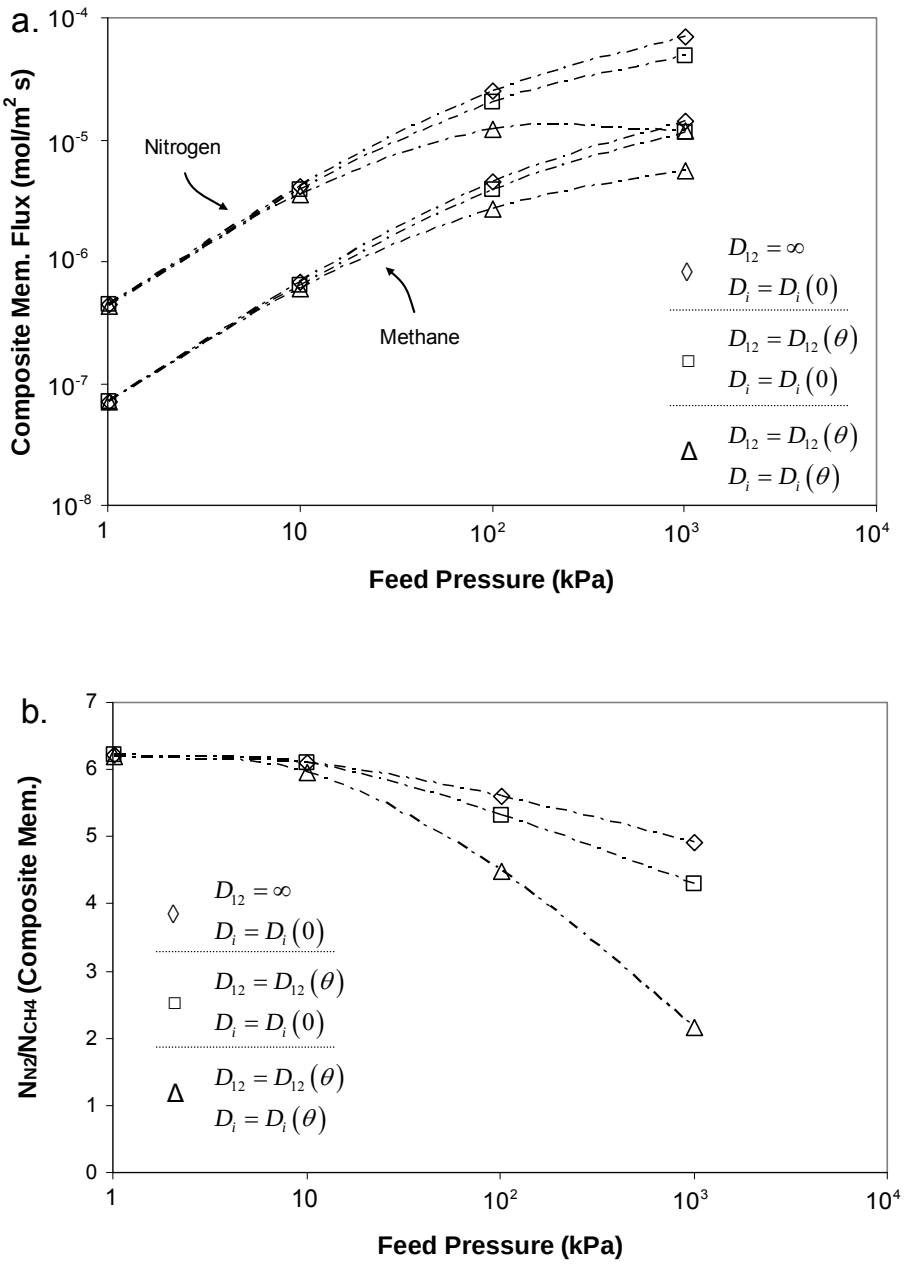

Figure 2.13: (a.) Flux and (b.) selectivity of nitrogen and methane as a function of feed pressure for a mixed matrix membrane composed of a microporous silica matrix [71] and clinoptilolite flakes [68]. The feed is 50/50, and the permeate is vacuum. Adsorption is modeled by the Extended Langmuir model, and three different models for the loading dependence of Maxwell-Stefan diffusivities are compared: (◊) Weak confinement and fascile exchange (Equations 2.12 and 2.14, Scenario I), (□) Weak confinement and Equation 2.15 for D_{ij} (Scenario III), and (Δ) Equation 2.13 for D_i and Equation 2.15 for D_{ij} (Scenario IV).

Membrane performance according to a constant-permeability analytical equation

The performance of the microporous silica/clinoptilolite mixed matrix membrane was also predicted by Cussler's analytical equation (Equation 2.49). Recall that analytical equations like this one use constant permeabilities. Here, we will use the low pressure (Henry's Law) values. That is, we will use those suggested by Equation 2.45:

$$P_i = \rho q_i^{sat} b_i D_i \qquad 2.56$$

When flake permeabilities and membrane geometry are set, Equation 2.49 can be conveniently plotted to show how mixed matrix selectivity depends on the matrix permeability. This is done in Figure 2.14, where mixed matrix selectivity is plotted as a function of P_1^M / P_1^F, as P_2^M / P_1^M and P_2^F / P_1^F are held constant. The arrow in Figure 2.14 corresponds to the permeability of the microporous silica matrix, and so indicates the predictions of Cussler's analytical equation for the mixed matrix membrane studied here.

Also shown in this figure are the results of finite element calculations for the performance of the mixed matrix membrane assuming constant matrix and flake permeabilities (Henry's Law values). This provides a comparison between a fully numeric, two-dimensional solution and the predictions of the analytical equation. As can be seen, the overall trend of the behavior of the membrane is given well by Cussler's equation, though the exact values are overestimated in comparison to finite element calculations.

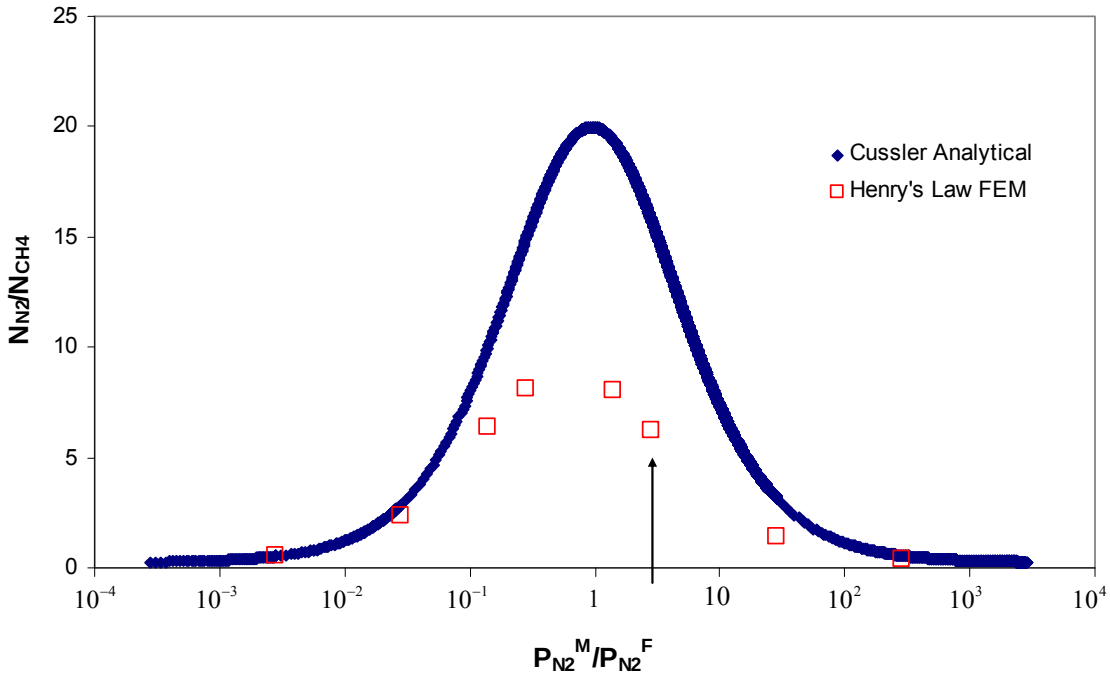

Figure 2.14: Predictions of Cussler's analytical equation (Equation 2.49) [1] for the performance of a microporous silica/clinoptilolite mixed matrix membrane. The arrow indicates the properties of the membrane considered here. The analytical expression predicts a selectivity of 15.8, while finite element calculations predict 6.2.

Figure 2.15 shows a curve similar to that shown in Figure 2.14, but for a mixed matrix membrane composed of a microporous silica matrix and silicalite-1 flakes for the separation of *para*- and *ortho*- xylene at 100°C. The adsorption isotherms of xylene isomers on silicalite-1 at 100°C are such that the assumption of Henry's Law is valid for pressures up to approximately 101.325 kPa [75]. For the present purposes, it is probably safe to assume that the assumption of Henry's law for the microporous silica is acceptable as well.

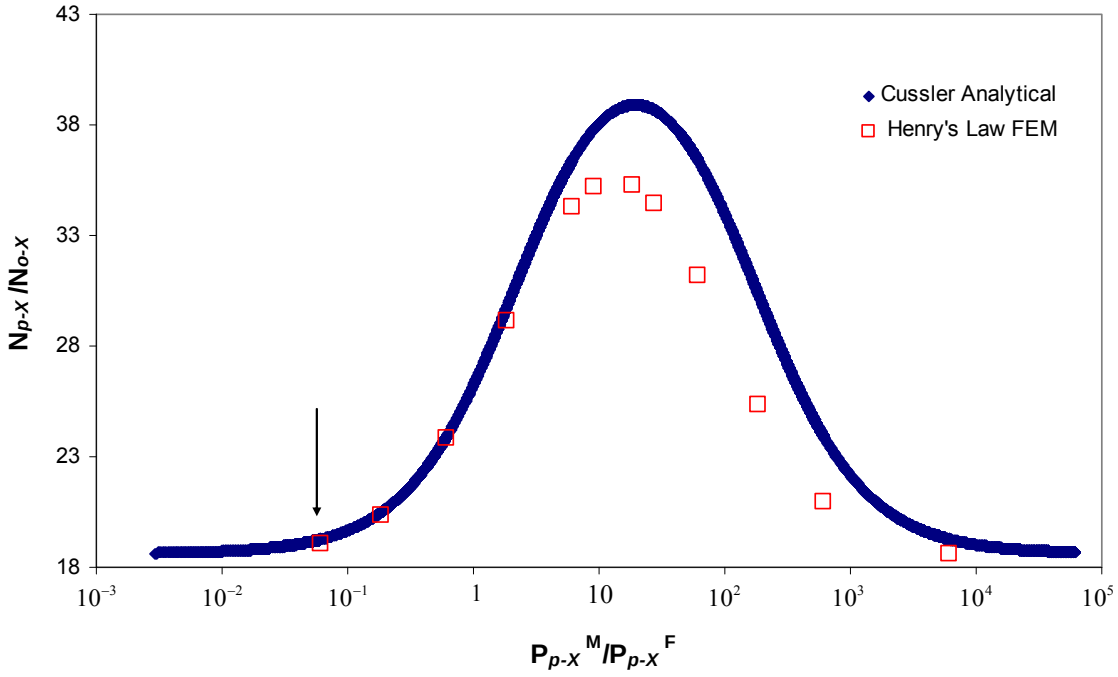

Figure 2.15: Predictions of Cussler's analytical equation (Equation 2.49) for the performance of a microporous silica [72] /silicalite [73] mixed matrix membrane for the separation of xylene isomers at 100°C. At this temperature, Henry's Law adsorption is a valid assumption. The arrow indicates the properties of the membrane considered here. This model predicts that an increase in the matrix permeability of one or two orders of magnitude is necessary for realization of significant performance enhancements due to the presence of flakes.

Test Case: Performance of a 1-dimensional composite membrane according to Scenario I

As a test of the numerical method, the finite element model was used to solve Equations 2.16, 2.17, and 2.22 on the one-dimensional domain shown in Figure 2.7. Of course, an analytical solution for this one-dimensional case exists, in the form of Equations 2.42 - 2.44. The results of the finite element calculation and the analytical solution are shown in Figure 2.16. As this figure shows, the finite element and analytical solutions are in agreement.

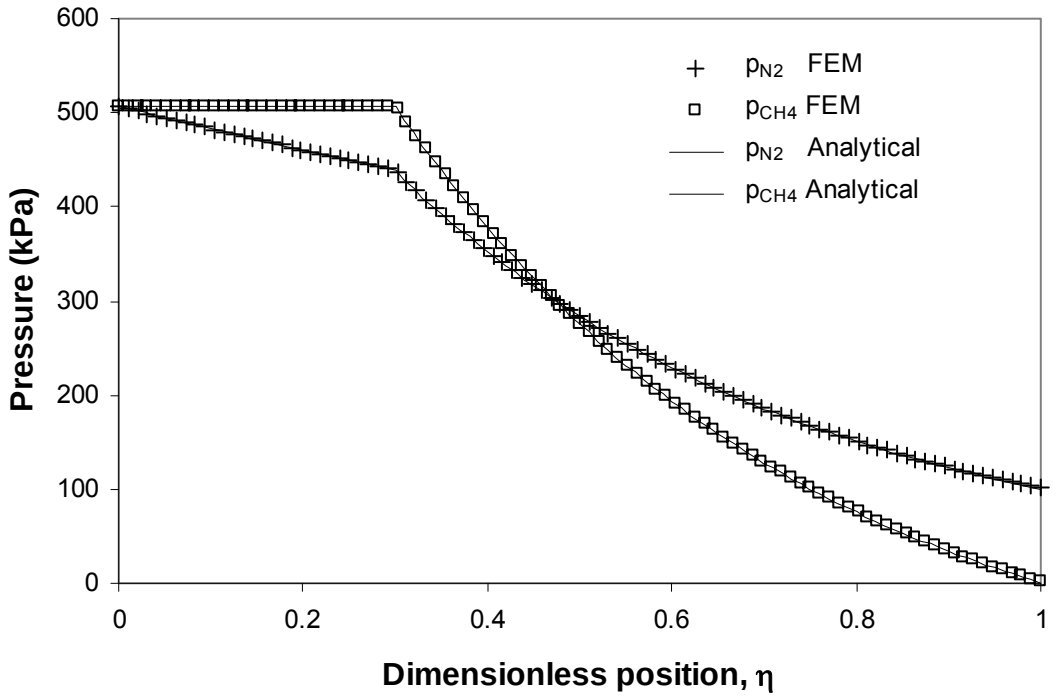

Figure 2.16: FEM and analytical predictions of the pressure profile across a one-dimensional clinoptilolite/microporous silica mixed matrix membrane.

2.5. Discussion

Constant permeability models: Cussler's analytical and Henry's Law FEM

The mixed matrix membrane performance predictions of two different models that assume constant matrix and flake permeabilities were presented above. Cussler's analytical model was used to predict the performance of both a microporous silica/clinoptilolite membrane and a microporous silica/silicalite-1 membrane. The constant permeabilities used in these calculations were obtained by calculating the low pressure, Henry's Law permeabilities for these materials. Also, two-dimensional finite element calculations assuming constant permeabilities were performed. Again, the constant permeabilities used were those from Henry's Law. By comparing the predictions of these two models to each other, the effect of the geometric assumptions inherent in the analytical model can be seen. By comparing the results of both of these models to numerical calculations that use more realistic constitutive equations (which encompass multicomponent adsorption isotherms and concentration-dependent diffusivities), the effect of the constant-permeability assumption is elucidated.

Figures 2.14 and 2.15 show that Cussler's analytical equation is quite successful at predicting the trends in mixed matrix selectivity as a function of the balance between matrix and flake permeability. The location of the selectivity maximum between the analytical and FEM calculations is very close. As a tool for guiding material selection in cases where permeability can be considered constant, the results presented here attest to the trustworthiness of this model. Despite significant assumptions employed in order to reduce the two-dimensional diffusion problem to a simple analytical express, the important behavior is captured well by this model for the cases considered here.

Of course, though the location of the selectivity maximum is predicted well by Cussler's equation for both mixed matrix membranes considered, it is clear that the predicted values for membrane selectivity are much better in one case (Figure 2.15) than the other (Figure 2.14). For the microporous silica-clinoptilolite membrane considered here, Cussler's equation would predict a selectivity of 15.8, while FEM

calculations predict 6.2. The discrepancy between the ability of Cussler's equation to accurately predict the selectivity values in the two cases considered here suggests that there is something about the permeabilities themselves that dictates when Cussler's equation will be more or less accurate. This is in addition to geometrical factors such as loading and flake aspect ratio, which have been shown to be important for determining the validity of such expressions for the case of barrier flakes [76].

Models that include multicomponent adsorption isotherms and constant diffusivities (Scenarios I and II)

In Figure 2.12 the results of two finite element calculations that do not assume Henry's Law are compared with one that does. Clearly, use of the more sophisticated adsorption isotherms results in predictions that are both quantitatively and qualitatively different from those given by Henry's Law. While all three models agree at low pressure, the drop in selectivity as feed pressure increases cannot be predicted by the Henry's Law model. This pressure dependence is a significant effect, which cannot be captured by a constant-permeability (Henry's Law or otherwise) model. For example, at 101.325 x 10^3 kPa, the Heny's Law model predicts a selectivity of 6, the Extended Langmuir model (Scenario I) predicts a selectivity of 5, and the Ideal Adsorbed Solution Theory (Scenario II) predicts a selectivity of 2.

The physical basis for the trends predicted by the models in Figure 2.12 that use the Extended Langmuir model and Ideal Adsorbed Solution Theory can be understood by revisiting the topic of adsorption selectivity. The diffusion coefficients remain constant in these calculations, so we do not have to consider their effect presently.

First, consider the adsorption selectivity of the matrix as a function of pressure according to the Ideal Adsorbed Solution Theory. This is shown in Figure 2.10b, from which it is clear that, as pressure increases, adsorption selectivity in the matrix increasingly favors methane. The same is true for the flake, as can be seen in Figure 2.10c, though the effect is much less. This is unfortunate, since the overall membrane is permselective for nitrogen at most of the feed pressures under consideration.

Adsorption selectivity in the matrix (and to a lesser extent, in the flake) is working against the overall performance of the membrane. Taking feed pressure as a characteristic operating pressure for the purposes of this discussion, the phenomenon of falling adsorption selectivity in the matrix and flake helps to explain why mixed matrix membrane selectivity would fall as operating pressure increases according to the calculations that use Ideal Adsorbed Solution Theory. Increasing permeate pressure also has the effect of raising the average operating pressure within the membrane, and this too causes a loss in nitrogen selectivity for the mixed matrix membrane, as seen in Figure 2.12.

This rationale is useful for understanding the predictions of the model that uses Ideal Adsorbed Solution Theory, but it does not explain the predictions of the model that uses the Extended Langmuir model. As Equation 2.53 and Figure 2.10a show, adsorption selectivity is not a function of total pressure according to the Extended Langmuir model. Nevertheless, selectivity of the mixed matrix membrane considered in Figure 2.12 falls as feed pressure increases, even according to the Extended Langmuir model. To understand this, it is important to recall that matrix and flake *selectivities* are not the only parameters that affect mixed matrix membrane selectivity. The balance of matrix and flake *permeabilities* also plays a strong role. When adsorption isotherms more complex than Henry's Law are used in the Maxwell-Stefan formulation, the effective permeability changes with pressure. This is obvious from Figure 2.8, where the flux though homogenous membranes is plotted as a function of pressure. At low pressure (Henry's Law regime) this is a straight line. At higher pressures, this curve begins to deviate from linearity. Permeability is flux divided by pressure gradient (c.f. Equation 2.45), and this curvature illustrates how permeability falls as a function pressure for these materials. The falling *permeabilities* of the matrix and flake materials have an effect on the permeability balancing of the mixed matrix membrane, even though the matrix and flake *selectivities* remain constant. In this case, the overall effect is to degrade mixed matrix membrane selectivity. In general, the

effect will depend on the way the permeabilities change in relation to one another, and instances of improved selectivity with pressure cannot be ruled out.

Models that contain concentration dependent diffusivities (Scenarios III and IV)

Restricting the above discussion to the limiting case of infinite exchange coefficients ($D_{ij} \to \infty$) and concentration-independent Maxwell-Stefan diffusivities ($D_i = D_i(0)$) allowed us to isolate the effect of the adsorption isotherms on the performance of a mixed-matrix membrane through the loading term, θ_i. Though very useful for our present purposes, these are not, in general, good assumptions. For example, several molecular dynamics studies predict that D_{ij} has a finite value small enough to have a significant effect on the diffusive fluxes of several species in a host of zeolites [57-59, 77]. Though specific predictions for the values D_{ij} and the concentration dependence of D_{ij} and D_i are not available for the system under consideration here, it would be at least reasonable to suspect that the assumption of $D_{ij} \to \infty$ and $D_i = D_i(0)$ may not be valid. Furthermore, the consideration of concentration-dependent diffusivities will allow us to explore one more way in which the performance of real mixed-matrix membranes might differ from that predicted by the models currently available.

To this end, Equations 2.8 and 2.17 were solved for a microporous silica/clinoptilolite mixed-matrix membrane using the Extended Langmuir adsorption model and Equations 2.13 and 2.15 for the loading-dependence of the diffusivities in both phases (Scenarios III and IV). As can be seen from Figure 2.13, the inclusion of loading-dependent diffusivities results in lower predictions for the membrane performance at high pressure and little change in performance at low pressure. In order to rationalize these predictions, it will be illuminating to consider the effect of Equations 2.13 and 2.15 on the performance of each individual phase. From Figure 2.11, it can be seen that the effect of Equations 2.13 and 2.15 is to degrade the inherent

selectivity of both the matrix and the flake. In the case of the matrix, this means that as pressure increases, the microporous silica becomes less selective for methane. In the case of the flake, this means that as pressure increases, the clinoptilolite becomes less selective for nitrogen. With respect to the performance of the composite (which is selective for nitrogen), this represents an enhancement for the matrix and a degradation for the flake. Of course, the matrix is still selective for methane, even at high pressures. In terms of the combined effect on the composite, it appears that the significant degradation of the flake selectivity is more important than the slight improvement of the matrix.

Though the degradation of the inherent selectivity of the individual phases as pressure increases is certainly one factor affecting the mixed matrix membrane's performance, it cannot explain all of the behavior shown in Figure 2.13. Compare the performance of a mixed matrix membrane that operates with a strongly loading-dependent D_i (according to Equation 2.13, Scenario IV) to the performance of a membrane with a constant D_i (Scenario III): the inclusion of a loading-dependent D_i (Scenario IV) results in predictions of lower selectivity. However, the inclusion of a loading-dependent D_i does not appreciably degrade the inherent selectivity of either of the membrane materials, as shown in Figure 2.11. That is, though there is no difference in the matrix or flake selectivities between Scenarios III and IV, there *is* a difference in the mixed matrix membrane selectivity between these two scenarios.

The reason for this is that the permeabilities of the matrix and flake are different in Scenarios III and IV. Inclusion of Equation 2.13 (in Scenario IV) lowers the permeability relative to Scenario III, as seen in Figure 2.13. This, once again, illustrates that changes in each phase's *permeability* as well as *selectivity* must be taken into account in order to completely understand the effect of pressure on the performance of a mixed-matrix membrane. Here, inclusion of Equations 2.13 and 2.15 has apparently shifted the permeability balance on the performance of the composite, just as was the case when considering the effect of the adsorption isotherms. All four parameters

important to composite performance ($P_1^M, P_2^M, P_1^F, P_2^F$) are complex functions of pressure.

A mixed matrix membrane for xylene isomer separations

The preceding discussion has dealt with the applicability of various models for mixed matrix membrane performance, concentrating on cases where constant permeabilities corresponding to Henry's Law adsorption behavior are not valid. The microporous silica/silicalite-1 composite for the separation of xylene isomers is a much simpler case. Because the adsorption isotherms are linear in the pressure range of interest, the Henry's Law result can be trusted. The predictions of the Henry's Law model, however are not encouraging. From Figure 2.14 it is clear that the addition of silicalite-1 flakes with a selectivity of approximately 45 is not effective in increasing the selectivity of the composite appreciably above the matrix selectivity of 18. This can be explained by an imbalance of the permeabilities of the two materials. The microporous silica matrix possesses a permeability that is too low, and the overall composite selectivity is dominated by the properties of the matrix. If it was possible to increase the permeability of the matrix by two to three orders of magnitude, perhaps by adding more organic template, a significant performance enhancement could be realized. For instance, if the permeability of the microporous silica to *p*-xylene could be increased by a factor of 100, Cussler's analytical equation predicts that the selectivity of the overall composite would be 33, even if the increase in permeability of the microporous silica was accompanied by a 50% decrease in *p*-/*o*- xylene selectivity. Alternatively, it has been shown that control of silicalite crystal morphology using oligomeric structure directing agents can result in high aspect-ratio, plate-like crystals with the thin dimension along several different crystallographic directions [78]. This too is a strategy that could be used to improve membrane performance for this system.

2.6. Conclusions

The case study presented here illustrates the importance of reasonably sophisticated models for the performance of composite membranes containing selective flakes. Using Cussler's analytical expression to predict the performance of our model membrane operating with a 50/50 feed at 1.01325 x 10^3 kPa and a permeate pressure of 1.01325 x 10^{-2} kPa would result in a predicted selectivity of 15.8. If finite element calculations utilizing Henry's Law adsorption were performed, the prediction would be 6.2. Use of an Extended Langmuir model for adsorption with weak confinement and facile exchange would lead to a prediction of 4.9, while the Ideal Adsorbed Solution Theory would yield 1.8. Similarly low selectivities are predicted by the Extended Langmuir model with loading-dependent diffusivities. Clearly there is a great difference between a membrane that offers a permselectivity of 15.8 and one that only offers 1.8. For the experimentalist wishing to design a mixed matrix membrane, the best available analytical equation is not sufficient for rationalizing material selection for a target separation or evaluating membrane performance.

It should be noted that, though the effect of various adsorption isotherms and models for Maxwell-Stefan diffusivities studied here has been to monotonically degrade the performance of the mixed-matrix membrane in comparison to Cussler's predictions as pressure increases, this may not always be the case. This is a complex system with many parameters, and only a simple case study has been presented here. A parametric study or a more rigorous mathematical exploration of this problem may reveal cases where increasing operating pressure can improve the selectivity of a mixed matrix membrane.

From the preceding discussion it should be clear that the level of understanding represented by Cussler's model and the associated intuitive explanation has not yet been attained for the current, more complex situation. Here, we do not have a system whose performance is governed by four constant parameters (P_1^M, P_2^M, P_1^F, P_2^F). Instead we

have at least 12 parameters (D_1^M , D_2^M , b_1^M , D_1^M , D_2^M , b_1^M , b_2^M , $q_1^{sat,M}$, $q_2^{sat,M}$, D_1^F , D_2^F , b_1^F , b_2^F , $q_1^{sat,F}$, $q_2^{sat,F}$), and it is not, at this juncture, clear how these should be balanced in order to obtain the optimum performance from a composite membrane.

Because fabrication of composite membranes with the structure idealized here is still a work in progress, the predictive power of the models presented cannot be readily verified. Nevertheless, attempts to formulate more complete models for the performance of these kinds of composites is important in as much as these predictions are used to guide membrane design and evaluate membrane performance. The model presented here provides what we hope is a more complete and useful description of the situation, upon which more work can be done to illuminate and optimize this interesting problem in material design.

Chapter 3. A Semi-empirical Model for Mixed Matrix Membrane Performance[‡]

3.1. Abstract

A successful model for mixed matrix membrane performance must address the complex geometry of the problem and accurately treat the diffusion behavior of the host-guest systems being considered. Detailed calculations based on the Maxwell-Stefan equations provide a widely accepted means of treating the diffusion of gases within zeolites. However, a full numerical solution of these equations for a complex mixed matrix membrane geometry does not offer the convenience and transparency that comes with an analytical treatment. At the same time, existing analytical equations which were formulated specifically to address mixed matrix geometry do so under the assumption of very simplistic models for diffusion. Here, an approach is presented for predicting the permeability and selectivity of mixed matrix membranes containing zeolite flakes that combines well-known analytical expressions for mixed matrix membrane performance with Maxwell-Stefan modeling for zeolite diffusion. The constant permeabilities required by the analytical models are calculated by the Maxwell-Stefan equations as a function of operating conditions, and these calculated effective permeabilities are used to predict mixed matrix membrane performance at corresponding operating conditions. The method is illustrated through two case studies: *n*-/*iso*-butane separation by a membrane containing silicalite-1 flakes and carbon dioxide/methane separation by membranes containing CHA-type zeolites. Predictions are compared to experimental results found in the literature for both cases. Also, the applicability of the Maxwell and Cussler analytical models for mixed matrix membrane performance is explored as a function of flake loading and aspect ratio.

[‡] Material presented in this chapter will be published in: J.A. Sheffel, M. *Tsapatsis, Journal of Membrane Science*, accepted.

3.2. Introduction

Mixed matrix membranes offer the hope of improving the performance of a separating membrane by dispersing a second phase within it. By combining the processability of a continuous phase (the matrix) with the separation characteristics of a dispersed phase (hereafter referred to as the flake, since high aspect ratio is generally desirable), mixed matrix membranes aim to provide a step-change improvement in membrane performance without dramatically increasing the cost of membrane technology [39].

One of the most important factors in the design of mixed matrix membranes is the proper matching of matrix and flake permeabilities. If the matrix permeability is either too high or too low in comparison to that of the flake, the selectivity of the mixed matrix membrane will show little improvement over that of the neat matrix. This has been understood for a long time, thanks to early models for diffusion in heterogeneous materials [1, 39-44].

These models yield analytical expressions for mixed matrix membrane permeability and selectivity. They utilize two distinct classes of assumptions. The first class pertains to geometrical approximations that are necessary to render a fundamentally three-dimensional diffusion problem amenable to an analytical solution. The models are generally distinguished from one another by the specific form that these arguments take. The second class of assumptions is related to how the matrix and flake permeabilities are treated as a function of concentration. The classic analytical models assume that these permeabilities are constant. While mathematically useful for the formulation of these expressions, the assumption of concentration-independent permeabilities is not valid in many important cases. Specifically in the case of zeolites, permeability is in general a function of concentration.

On the other hand, we recently presented a numerical study of mixed matrix membrane performance which both allowed for concentration-dependent permeabilities and dispensed with many of the geometric arguments characteristic of the analytical models [79]. However, this two-dimensional approach requires numerical solution, and thus the effect of the design parameters (such as flake loading and aspect ratio and matrix and flake diffusion coefficients) is not as transparent as in an analytical expression.

Here we propose a hybrid approach for predicting the performance of mixed matrix membranes containing zeolite flakes. First, the validity of the geometric assumptions contained in the analytical models is explored in a short study where constant matrix and flake permeabilities are assumed. Second, the permeability of zeolite flakes is calculated as a function of concentration, drawing on existing models for diffusion in zeolites. Finally, these concentration-dependent permeabilities are used in conjunction with the proper analytical models to predict mixed matrix membrane performance.

We aim to demonstrate this hybrid approach through two case studies. In the first, we address the design of a mixed matrix membrane containing silicalite-1 flakes for the separation of butane isomers. The effective permeabilities of silicalite-1 to butanes are calculated as a function of operating pressure by the Maxwell-Stefan model for zeolite diffusion. These effective permeabilities are then used in an analytical model for mixed matrix membrane performance in order to gain insight into the effect of operating conditions on the proper choice of matrix material. These predictions are compared to experimental results. Finally, the separation of carbon dioxide and methane by mixed matrix membranes containing CHA-type zeolites is considered. The predictions of this approach are explored as they relate to Robeson's upper bound for experimentally available polymers, and they are compared to a recently reported experimental membrane.

3.3. Theory

Of the several analytical models for mixed matrix membrane performance, one adapted from Maxwell's treatment of the conductivity of a dilute suspension of spheres enjoys wide popularity [15, 39, 43, 51, 52]. It predicts that the permeability of component i in a mixed matrix membrane will be given by:

$$P_i^C = P_i^M \frac{P_i^F + 2P_i^M - 2\phi\left(P_i^M - P_i^F\right)}{P_i^F + 2P_i^M + \phi\left(P_i^M - P_i^F\right)} \qquad 3.1$$

where ϕ is the volume fraction of flakes in the composite, and P_i^M and P_i^F are the respective permeabilities of the matrix and flake. A model developed by Cussler is similar in form, but considers a staggered array of high aspect ratio particles [1]. It predicts:

$$P_i^C = P_i^M \frac{1}{1-\phi+\dfrac{1}{\dfrac{1}{\phi}\dfrac{P_i^F}{P_i^M}+4\dfrac{1-\phi}{\alpha^2\phi^2}}} \qquad 3.2$$

where α is the flake aspect ratio, defined as the ratio of the longest to the shortest dimension of the flake (note that Cussler defines α as half this ratio, and his equation differs accordingly). The selectivity of a mixed matrix membrane according to this model is:

$$\frac{P_2^C}{P_1^C} = \frac{P_2^M}{P_1^M} \frac{1 + \left(\frac{\alpha^2 \phi^2 \Big/ (1-\phi)^2}{4 + \frac{\alpha^2 \phi}{P_1^M \Big/ P_1^F (1-\phi)}} \right)}{1 + \left(\frac{\alpha^2 \phi^2 \Big/ (1-\phi)^2}{4 + \frac{\alpha^2 \phi}{P_2^M \Big/ P_2^F (1-\phi)}} \right)} \tag{3.3}$$

In general, permeability is concentration dependent, though these analytical equations were formulated as if the matrix and flake permeabilities are constant. Only when the corrected diffusivity is constant and the equilibrium relationship between bulk species partial pressure and adsorbed amount is linear (Henry's law adsorption regime) is the permeability concentration-independent. This limit is often not realized for zeolites under practical conditions for membrane operation. In order to address this shortcoming, we propose that these permeabilities be considered, not as constant material properties, but instead in the context of a specific flux calculation (or measurement). That is:

$$P_i \equiv \frac{N_i}{\Delta p_i \Big/ l} \tag{3.4}$$

where N_i is the flux of species i across a pure (not mixed matrix) membrane of thickness l when exposed to a species partial pressure difference of Δp_i. In this way, the permeabilities that appear in, for example, Equation 3.3 can be calculated for pure polymer and zeolite membranes at specific experimental conditions, and these calculated permeabilities (which are functions of operating conditions) can be used to predict the performance of mixed matrix membranes at corresponding operating

conditions. The proper choice of "corresponding operating conditions" is, of course, not obvious, and a rational approach for making this choice will be discussed below.

The Maxwell-Stefan formulation is generally accepted as the best-suited continuum method for the treatment of diffusion within zeolites [48]. The Maxwell-Stefan equation is:

$$-\rho \frac{q_i}{q_i^{sat} RT} \nabla \mu_i = \sum_{\substack{j=1 \\ i \neq j}}^{n} \frac{q_j \underline{N}_i - q_i \underline{N}_j}{q_i^{sat} q_j^{sat} D_{ij}} + \frac{\underline{N}_i}{q_i^{sat} D_i} \tag{3.5}$$

where q_i is the loading of component i ($mol\ i/kg$ adsorbent), ρ is the density of the zeolite (kg/m^3), and μ_i is the chemical potential. The two types of diffusivities (D_i and D_{ij}) that appear in the Maxwell-Stefan equation are in general both dependent on concentration [48]. The exact form of these concentration dependencies has been the focus of numerous molecular dynamics studies [55-61], and the behavior has been found to be very host-guest specific. Here, the so-called strong confinement limit for the behavior of D_i will be used for butanes in silicalite-1:

$$D_i = D_i(0)\left(1 - \sum_i \theta_i\right) \tag{3.6}$$

This relation asserts that molecular jumps from one site to another occur only when the destination site is vacant. Thus, the Maxwell-Stefan diffusivity is proportional to the void fraction ($\theta_V = 1 - \sum_i \theta_i$) [63]. The strong confinement scenario does not allow for sorbate-sorbate interactions which might alter the jump frequency by decreasing the energy barrier for diffusion [59]. The Reed-Ehrlich model, which is more sophisticated, allows for these effects [80, 81]. Though several recent MD studies have found that this model is able to accurately predict the more complex loading dependencies which are

observed for some systems [59, 77, 81, 82], the strong confinement relation will be sufficient for our purposes with butanes in silicalite-1. For carbon dioxide and methane in CHA-type zeolites, there is sufficient data to both recommend the use Reed-Ehrlich and to allow its implementation.

The Maxwell-Stefan exchange coefficients, D_{ij}, are in general related to the Maxwell-Stefan diffusivities, D_i, and the species loadings. Krishna and Wesselingh suggested the following logarithmic interpolation formula [48]:

$$D_{ij} = D_i^{q_i/(q_i+q_j)} D_j^{q_j/(q_i+q_j)} \qquad 3.7$$

Skoulidas *et al.* have suggested an alternative to Equation 3.7 that provides more quantitative agreement with molecular dynamics simulations in many cases [55, 59, 77], but its application requires detailed knowledge of self diffusivities, such knowledge usually being gained from molecular dynamics simulations themselves. For our purposes with butanes in silicalite-1, Equation 3.7 will suffice to provide the qualitative consequence of the correlation effects embodied by D_{ij}. For carbon dioxide and methane in CHA, the exchange coefficients are assumed infinite, as suggested by recent experimental and MD studies [83, 84].

The Ideal Adsorbed Solution Theory of Myers and Prausnitz [85] will be used to make the multicomponent adsorption predictions necessary for the solution of Equation 3.5.

3.4. Results and Discussion

Evaluation of analytical models for mixed matrix membrane performance

To evaluate the effectiveness of the Maxwell (Equation 3.1) and Cussler (Equation 3.2) models for mixed matrix membrane performance, the predictions of each were compared to two-dimensional finite element calculations for membranes of

various geometries. In both the analytical models and the finite element calculations, the flake and matrix permeabilities were assumed to be constant (concentration independent). The comparison was made by constructing curves of predicted mixed matrix membrane permeability and selectivity as a function of matrix permeability, holding matrix selectivity and flake permeability constant. That is, P_2^F, P_1^F, and P_2^M / P_1^M were fixed, and P_2^M was varied. Several geometries of uniformly distributed flakes were constructed, varying the flake aspect ratio (α) and volume fraction (ϕ). For each of these geometries, the results of finite element calculations were compared to the predictions of the analytical models.

Figures 3.1 and 3.2 show examples of these comparisons. Figure 3.1 shows the results for a mixed matrix membrane with 30 volume percent flakes with an aspect ratio of 50. For this example, the Cussler model shows much better agreement with the finite element calculations than the Maxwell model. On the other hand, the calculations presented in Figure 3.2 are for a geometry (α = 1, ϕ = 0.3) for which the Maxwell model shows better agreement. For several geometries, calculations like those illustrated in Figures 3.1 and 3.2 were performed, and for each geometry a judgment was made about which analytical model (Cussler or Maxwell) provided the closest agreement with the numerical results. The results of these calculations are summarized in Figure 3.3.

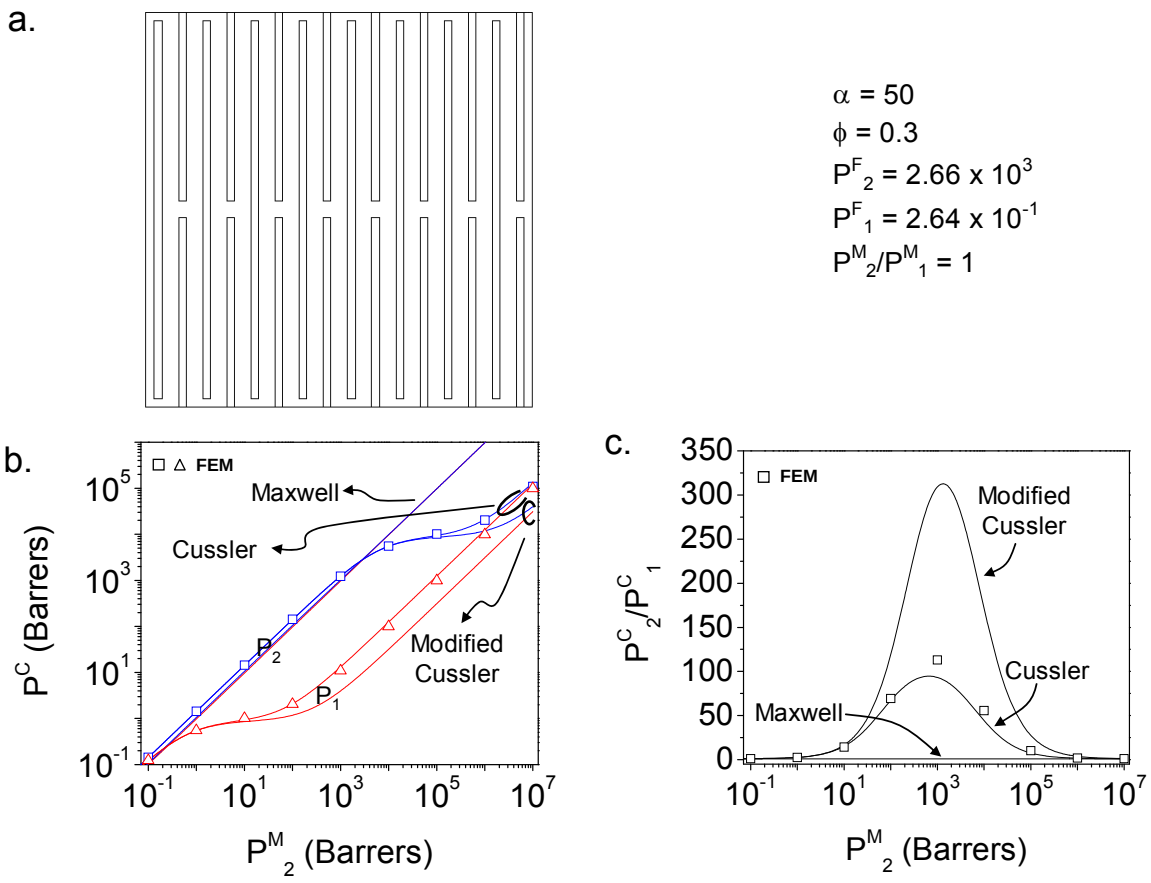

Figure 3.1: Comparison of finite element calculations (FEM) and analytical models for the performance of a mixed matrix membrane containing flakes with an aspect ratio of α = 50 and loading of ϕ = 30%. Flake permeabilities are P_2^F = 2.66 x 10^3, P_1^F = 2.64 x 10^{-1} Barrers. The matrix selectivity is P_2^M / P_1^M = 1. (a.) Geometry and parameters. (b.) Mixed matrix membrane permeability as a function of matrix permeability. (c.) Mixed matrix membrane selectivity as a function of matrix permeability.

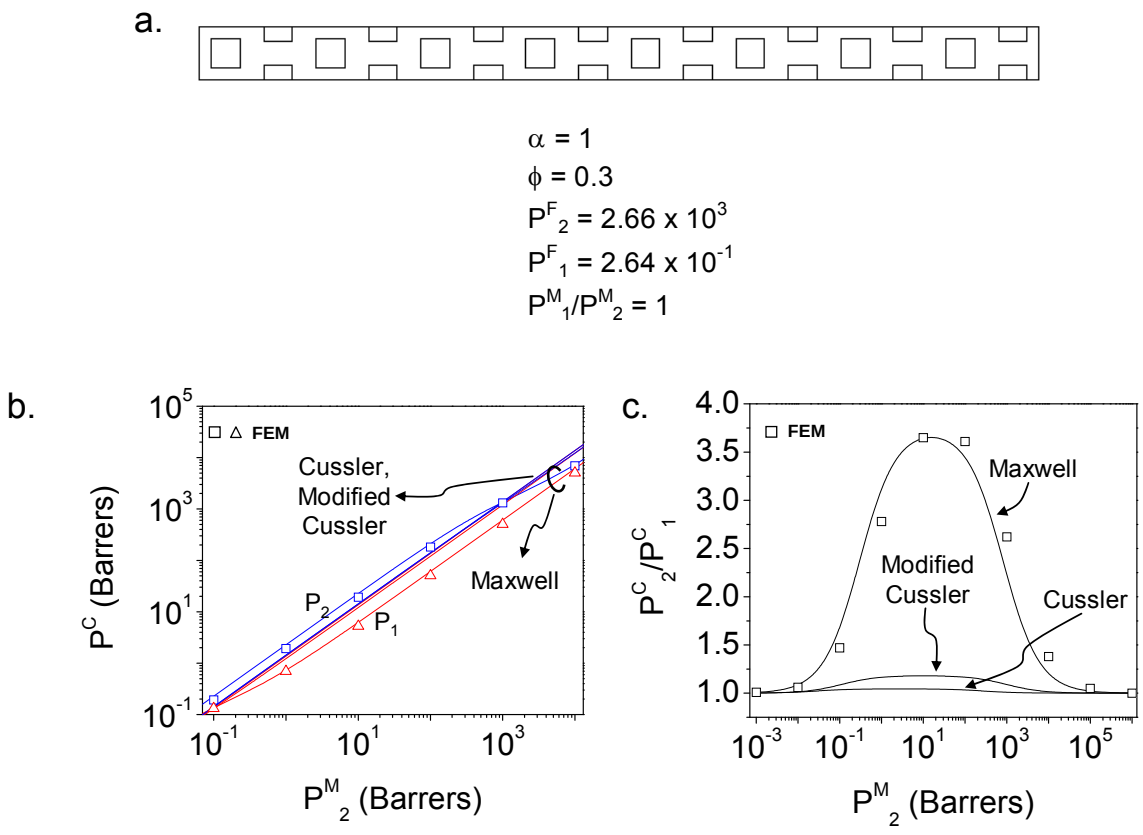

Figure 3.2: Comparison of finite element calculations (FEM) and analytical models for the performance of a mixed matrix membrane containing flakes with an aspect ratio of α = 1 and loading of ϕ = 30%. Flake permeabilities are P_2^F = 2.66 x 10^3, P_1^F = 2.64 x 10^{-1} Barrers. The matrix selectivity is P_2^M / P_1^M = 1. (a.) Geometry and parameters. (b.) Mixed matrix membrane permeability as a function of matrix permeability. (c.) Mixed matrix membrane selectivity as a function of matrix permeability.

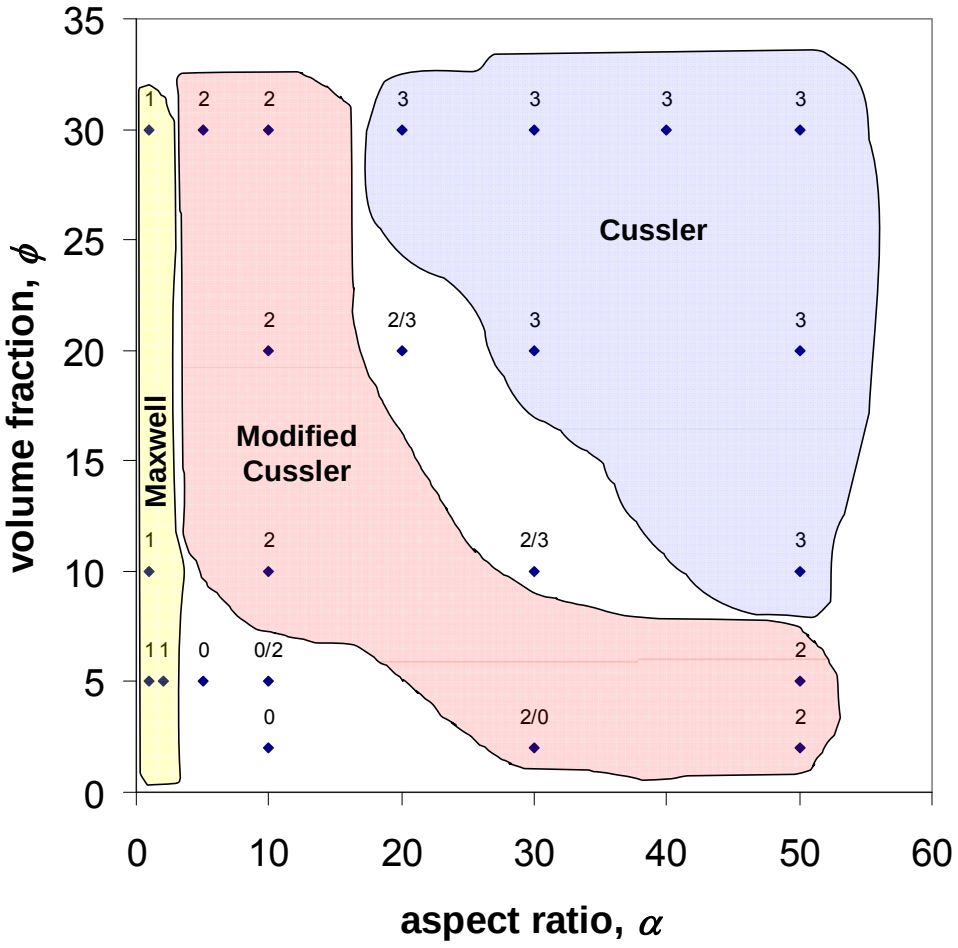

Figure 3.3: Diagram showing the applicability of various analytical models for the performance of mixed matrix membranes as a function of flake aspect ratio and loading. 1: Maxwell Model (Equation 3.1), 2: Modified Cussler Model (Equation 3.8), 3: Cussler Model (Equation 3.2), 0: no acceptable model was found.

This figure shows that the Cussler model is reasonably successful for predicting mixed matrix membrane performance when the aspect ratio is large and the volume fraction is moderate to large. That the Cussler model should fail for low aspect ratio flakes is unsurprising because the assumption of high aspect ratio is central to its derivation. On the other hand, the Maxwell model assumes low loading and spherical "flakes." This is born out in Figure 3.3, where the area at low volume fraction and low loading is best matched by the Maxwell model. However, the region of applicability of

the Maxwell model extends up to at least 30 volume percent, a result which is somewhat unexpected since this can hardly be considered dilute.

Figure 3.3 reveals that there are many combinations of volume fraction and aspect ratio for which neither the Maxwell nor Cussler models are successful for predicting mixed matrix membrane performance. A slight modification of the Cussler model, which results in Equation 3.8, provides an equation which is able to fill much of this gap.

$$P_i^C = P_i^M \frac{1}{1-\phi+\frac{1}{\frac{1}{\phi}\frac{P_i^F}{P_i^M}+\frac{1-\phi}{\alpha^2\phi^2}}} \qquad 3.8$$

Figure 3.4 provides one example of how this modified Cussler model shows better agreement with the numerical results than either of the previous models. The success of this modification is presented here as an empirical observation since no satisfactory rationale for its success is obvious to us.

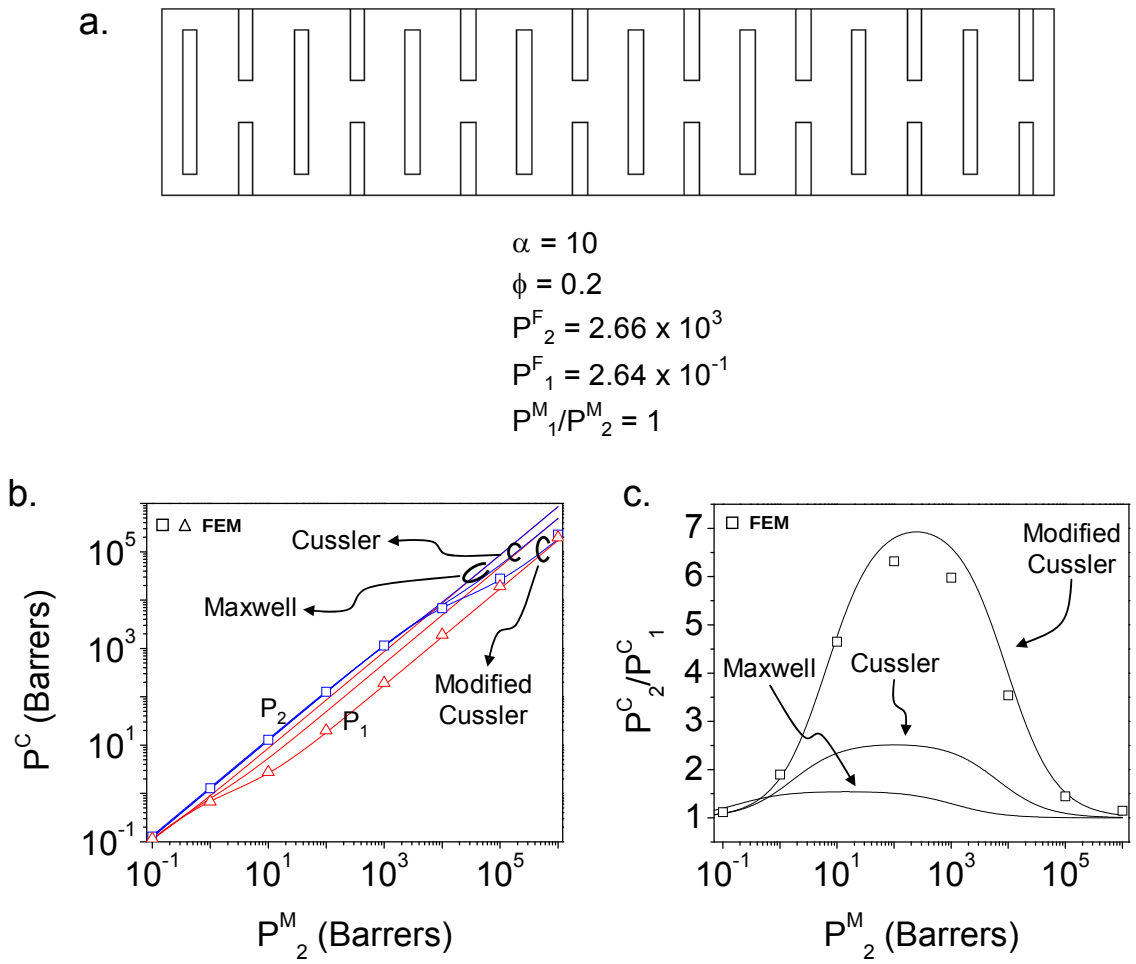

Figure 3.4: Comparison of finite element calculations (FEM) and analytical models for the performance of a mixed matrix membrane containing flakes with an aspect ratio of α = 10 and loading of ϕ = 20%. Flake permeabilities are P_2^F = 2.66 x 10^3, P_1^F = 2.64 x 10^{-1} Barrers. The matrix selectivity is P_2^M / P_1^M = 1. (a.) Geometry and parameters. (b.) Mixed matrix membrane permeability as a function of matrix permeability. (c.) Mixed matrix membrane selectivity as a function of matrix permeability.

Calculation of concentration-dependent zeolite permeabilities

Having established that analytical models exist which are accurate for a large range of flake loading and aspect ratio, the issue of concentration-dependent permeabilities can be addressed. As explained above, it is desirable to formulate an approach which takes into account the concentration-dependent nature of zeolite permeability while preserving some of the ease and transparency of the analytical

models. To accomplish this, we propose a hybrid approach. Instead of addressing the fact that each flake has a different permeability in a real mixed matrix membrane, we attempt to find a single flake permeability which represents a kind of average and can be used in the analytical models to accurately predict the performance of the composite at a certain set of operating conditions. Though this average permeability is essentially a fitting parameter, we are not without rational guidelines to aid in its estimation. For instance, we can evaluate the permeability of the flake at conditions which represent a rough average of the conditions that flakes would encounter across the mixed matrix membrane thickness. The highest pressure a flake could be expected to see in a mixed matrix membrane is the feed pressure, and the lowest is the permeate pressure. The appropriate average permeability should be found by evaluating the properties of the flake at some feed pressure between these two. The pressure drop across any individual flake in a mixed matrix membrane will be much less than the pressure drop across the entire mixed matrix membrane, so when searching for the appropriate average permeability, the flake should be evaluated with some pressure drop less than that across the mixed matrix membrane.

Figure 3.5 shows the calculated normal- and iso-butane permeability of a silicalite-1 membrane as a function of operating pressure. The feed composition is 50/50 *n*-/*i*-butane and the total permeate pressure is equal to one-half the total feed pressure. The permeate composition was found by adjusting the ratio of permeate partial pressures until they equaled the ratio of species fluxes, i.e., until a mass balance on the permeate side was consistent. The Maxwell-Stefan equation with the strong confinement scenario and the logarithmic interpolation formula (Equations 3.5 - 3.7) was used to calculate these permeabilities.

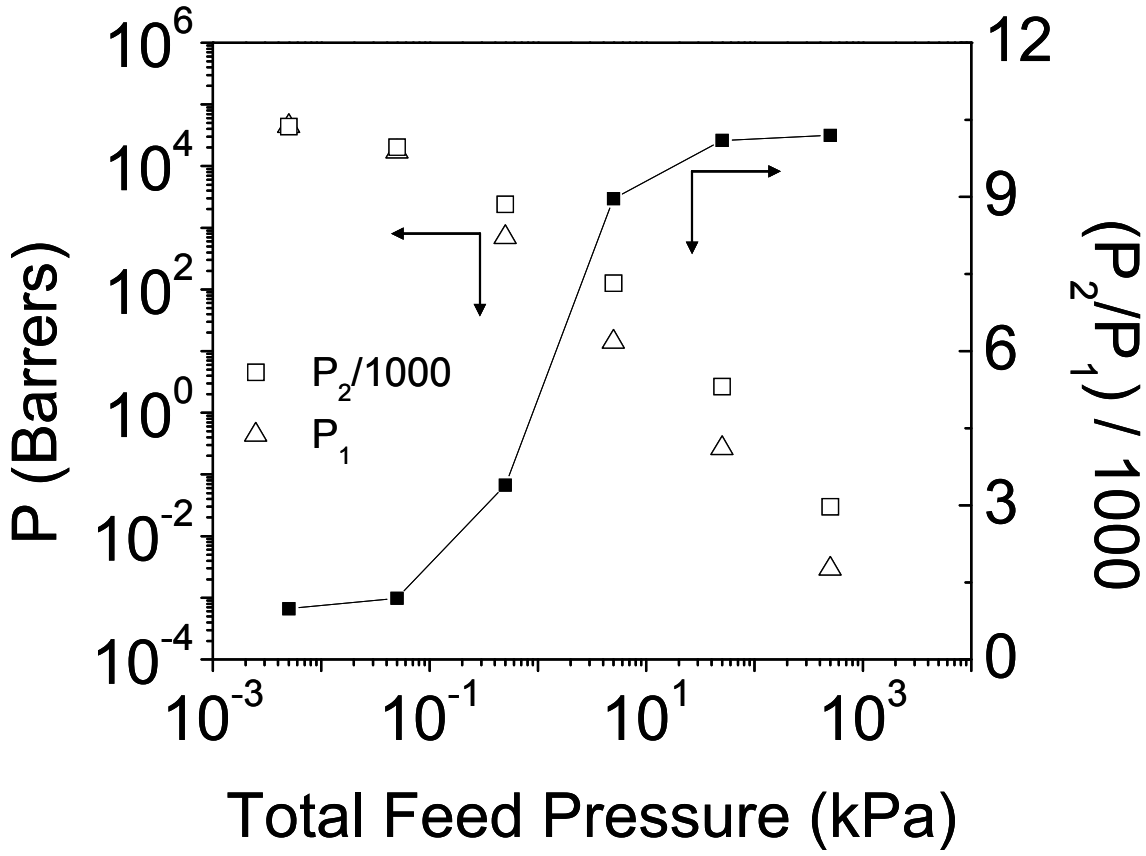

Figure 3.5: Permeability of a silicalite-1 membrane to normal- and iso-butane as a function of feed pressure for a 50/50 feed mixture and a 50% pressure drop across the membrane according to the Maxwell-Stefan model.

The single-component adsorption isotherms and diffusion coefficients used to calculate these concentration-dependent permeabilities were taken from the literature and are given in Tables 3.1 and 3.2 (shaded values). The dual-site Langmuir adsorption parameters were taken from an experimental study and show reasonable agreement with other experimental and computationally derived isotherms [86]. The iso-butane diffusivity was taken from an interference microscopy study [87], and the normal-butane value comes from a MAS PFG NMR measurement [88]. While it is the zero-loading Maxwell-Stefan diffusivities that are needed presently, both values listed in Table 2 were measured at finite loadings and neither is a proper Maxwell-Stefan diffusivity. Figure 3.6 places these diffusivities within the context of other values

reported in the literature, from which it can be seen that the differences between various reported values are immense. Given these well-known discrepancies, the effect of finite loading on the value of the diffusivities used here is likely smaller than the uncertainty introduced by choosing a particular value from the many available in Figure 3.6.

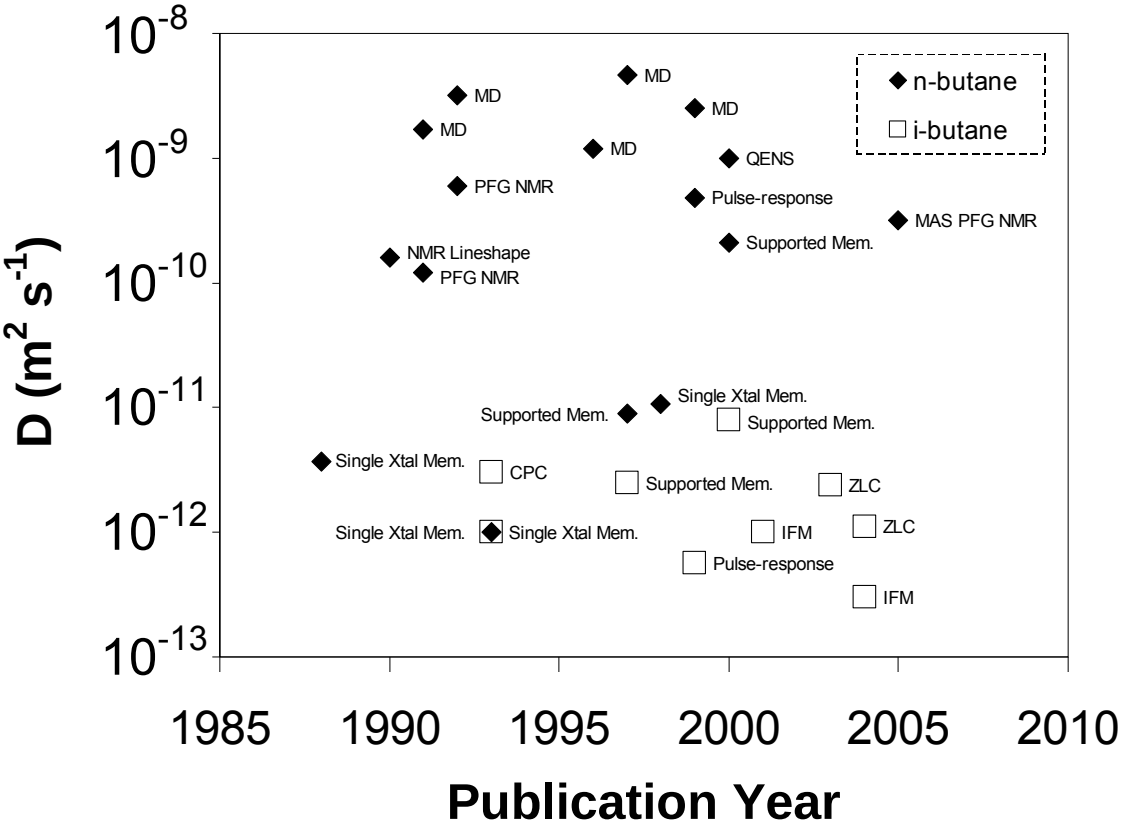

Figure 3.6: Literature values for the diffusion coefficients of normal- and iso-butane in silicalite-1.

Table 3.1: Dual-site Langmuir adsorption isotherm parameters for normal and isobutane in silicalite-1 [86].

	q_c (molecules / unit cell)	K_c (kPa^{-1})	q_I (molecules / unit cell)	K_I (kPa^{-1})
n-butane	8	21.4	2	0.315
i-butane	6	0.0212	4	13.9

Table 3.2: Normal and iso-butane diffusivity values from the literature. This data was used to construct Figure 3.6. The shaded values were used to model the diffusion of butanes in silicalite-1.

	D (m^2 s^{-1})			
Year	*i*-butane	*n*-butane	Reference	Method
2004	3×10^{-13}	---	[89]	IFM
2001	1×10^{-12}	---	[87]	IFM
2004	1×10^{-12}	---	[90]	ZLC
2003	2.4×10^{-12}	---	[91]	ZLC
1993	3×10^{-12}	---	[92]	CPC
1993	1×10^{-12}	1×10^{-12}	[93]	Single crystal membrane
1997	2.5×10^{-12}	9×10^{-12}	[94]	Supported membrane
2000	8×10^{-12}	2.1×10^{-10}	[95]	Supported membrane
1999	5.7×10^{-13}	4.8×10^{-12}	[96]	Pulse-Response
2005	---	3.17×10^{-10}	[88]	MAS PFG NMR
1997	---	4.61×10^{-9}	[97]	MD
1991	---	1.7×10^{-9}	[98]	MD
1992	---	3.2×10^{-9}	[99]	MD
1996	---	1.2×10^{-9}	[100]	MD
1990	---	1.6×10^{-10}	[101]	NMR line shape
1988	---	3.7×10^{-12}	[102]	Single crystal membrane
1992	---	6.0×10^{-10}	[103]	PFG NMR
2000	---	1.0×10^{-9}	[104]	QENS
1999	---	2.5×10^{-9}	[105]	MD
1998	---	1.07×10^{-11}	[106]	Single crystal membrane
1991	---	1.2×10^{-10}	[107]	PFG NMR

Hybrid approach to mixed matrix membrane performance prediction and comparison to finite element calculations

Figure 3.7 shows an example of how the calculated permeabilities from Figure 3.5 can be used to predict the performance of a mixed matrix membrane operating with a 50/50 *n*-/*i*-butane feed at a pressure of 100 kPa and a permeate pressure of 0 kPa. The membrane contains silicalite-1 flakes with an aspect ratio of 50 and a loading of 30%. Per Figure 3.3, this geometry falls within the Cussler model regime. The open symbols on Figure 3.7 are the result of finite element calculations which allow the silicalite-1 flakes to behave as they would in a real membrane. That is, they follow Maxwell-Stefan diffusion, and the properties depend on concentration. The curves are the predictions according to the Cussler model using a constant flake permeability that was obtained by evaluating the properties of silicalite-1 at some "average" conditions. These conditions were: 50/50 feed composition, 50 kPa total feed pressure, and 25 kPa total permeate pressure. These "average" conditions were chosen according to the following guidelines: the feed composition was equal to that of the mixed matrix membrane, the total feed pressure was equal to one-half the feed pressure of the mixed matrix membrane, and the fractional pressure drop ($\Delta p / p_t^{feed}$) was equal to one-half that of the mixed matrix membrane. As this figure shows, the predictions of the Cussler model using this permeability are not far off from the finite element calculations. Note especially that the same flake permeabilities were used for each plot in Figure 3.7. That is, the same value of the flake permeability (the fitting parameter) is able to successfully predict the performance of membranes with different matrices (P_2^M / P_1^M = 1, 2, and 5 for the membranes in Figure 3.7 a., b., and c., respectively).

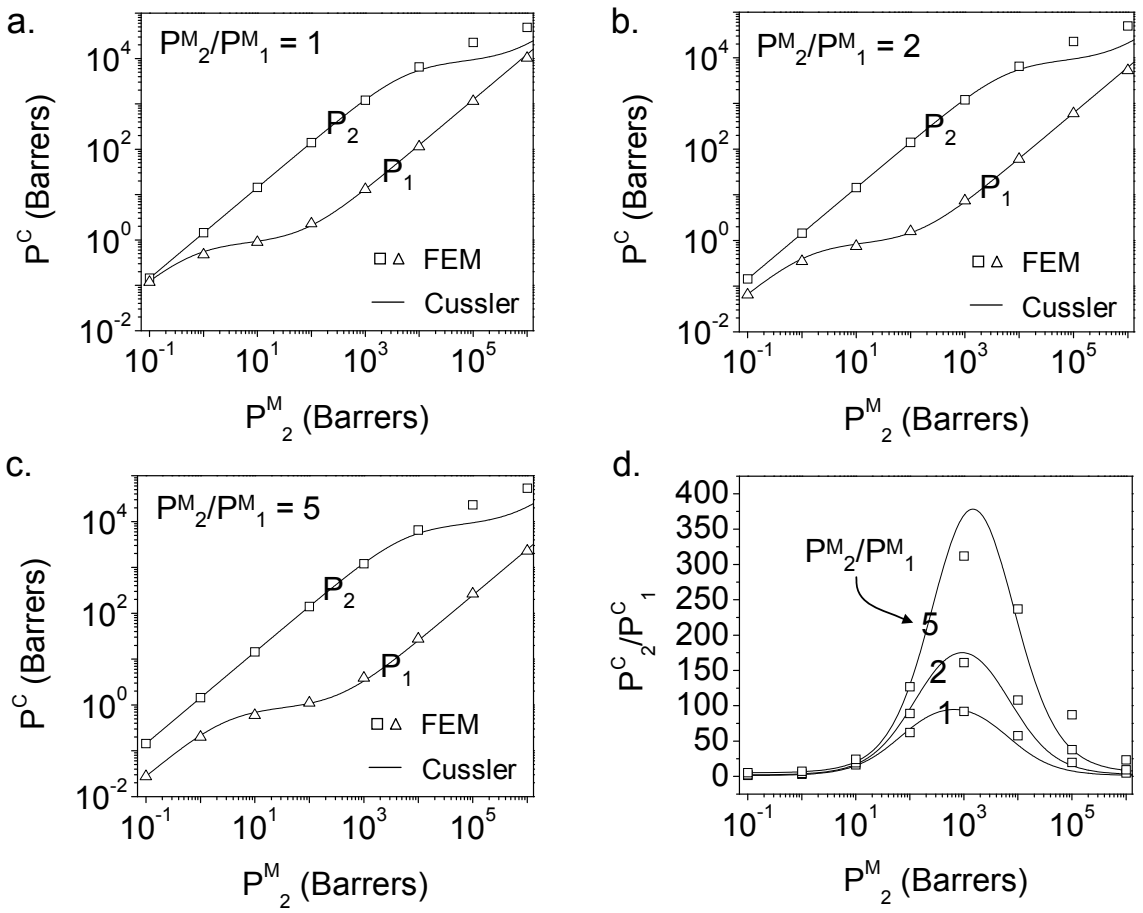

Figure 3.7: Predictions for the performance of a mixed matrix membrane containing flakes with an aspect ratio of α = 50 and loading of ϕ = 30%. The feed composition is 50/50 and the total feed and permeate pressures are p_t^{feed} = 100 kPa and $p_t^{permeate}$ = 0 kPa. Open symbols are the result of finite element calculations (FEM) for a membrane with a constant-permeability matrix and flakes which are governed by the Maxwell-Stefan equation. The curves are the predictions of the Cussler model, where both matrix and flake have constant permeabilities. The flake permeabilities used in the Cussler model were those of a silicalite-1 membrane with a 50/50 feed and p_t^{feed} = 50 kPa and $p_t^{permeate}$ = 25 kPa.

In Figure 3.8 another example of this approach is given, but for a membrane with a different geometry. Here, predictions are shown for a membrane containing flakes with an aspect ratio of 5 at a loading of 30%. Again, the flake permeability used to predict the performance of this mixed matrix membrane is that obtained from calculations for silicalite-1 at 50 kPa feed, 50/50 feed composition, and 25 kPa total

permeate pressure. The map provided by Figure 3.3 indicates that the modified Cussler model should be used for this geometry, and as Figure 3.8 illustrates, this model works well for this membrane. Figure 3.7 and Figure 3.8 begin to illustrate the robust nature of this approach. Even though the flake permeabilities are essentially fitting parameters, these figures show that, once determined, they can be applied for different values of matrix selectivity and different geometries.

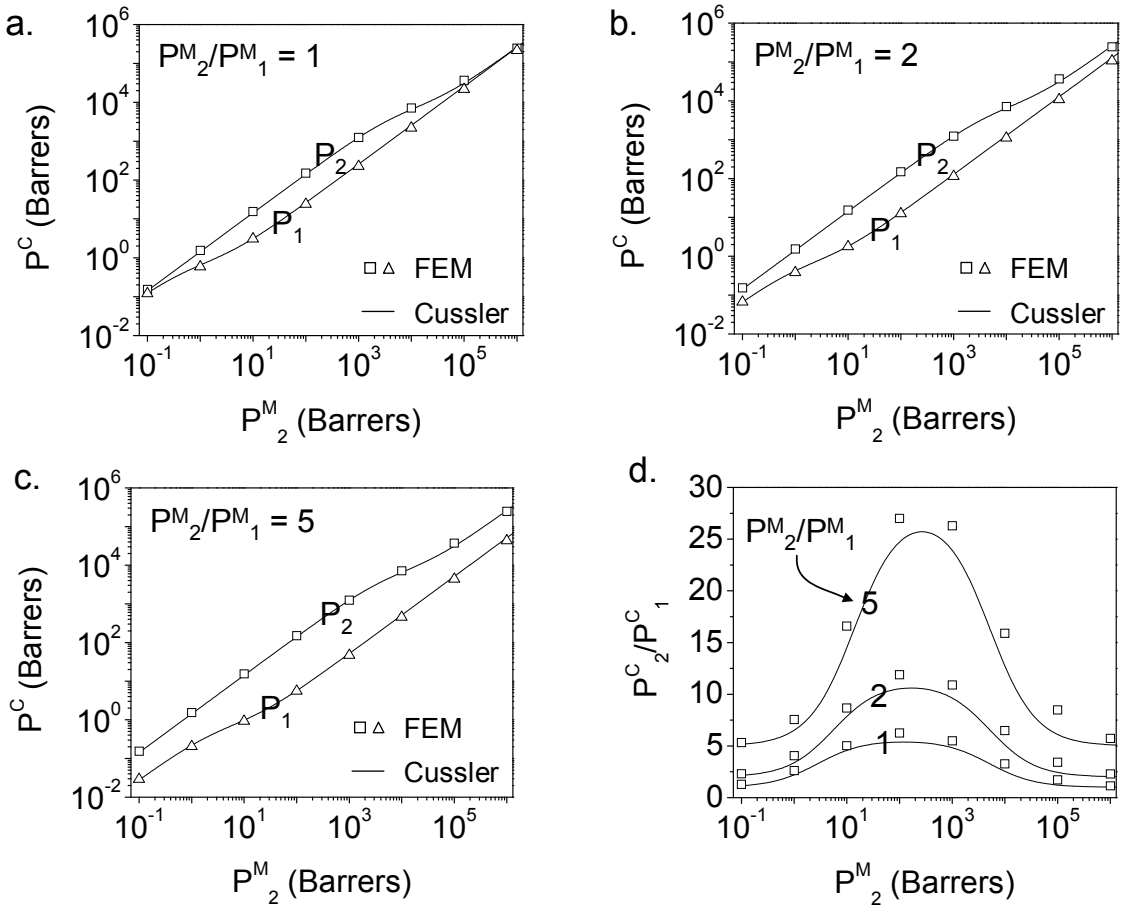

Figure 3.8: Predictions for the performance of a mixed matrix membrane containing flakes with an aspect ratio of α = 5 and loading of ϕ = 30%. The feed composition is 50/50 and the total feed and permeate pressures are p_t^{feed} = 100 kPa and $p_t^{permeate}$ = 0 kPa. Open symbols are the result of finite element calculations (FEM) for a membrane with a constant-permeability matrix and flakes which are governed by the Maxwell-Stefan equation. The curves are the predictions of the modified Cussler model, where both matrix and flake have constant permeabilities. The flake permeabilities used in the Cussler model were those of a silicalite-1 membrane with a 50/50 feed and p_t^{feed} = 50 kPa and $p_t^{permeate}$ = 25 kPa.

Figure 3.9 illustrates that the method applied above for finding the appropriate average permeabilities is valid not only at different matrix selectivities and geometries, but also at a different feed pressures. In this figure the performance of a mixed matrix membrane with a 50/50 feed composition, 1 kPa feed pressure, and a permeate pressure of 0 kPa is predicted. Since the feed pressure for this mixed matrix membrane is one

hundred times lower than in the previous example, a different flake permeability must be used. As before, the appropriate permeability is calculated by evaluating the properties of a silicalite-1 membrane at half the mixed matrix membrane's feed pressure and with a pressure drop of 50%. That is, the permeability of a silicalite-1 membrane is calculated for a 50/50 feed at 0.5 kPa and a total permeate pressure of 0.25 kPa. Per Figure 3.3, the Cussler model is used to predict the performance of the mixed matrix membrane. As Figure 3.9 shows, there is good agreement between the predicted and numerical results, demonstrating that the outlined approach for determining acceptable values of the flake permeability "fitting parameters" is useful at more than just one pressure.

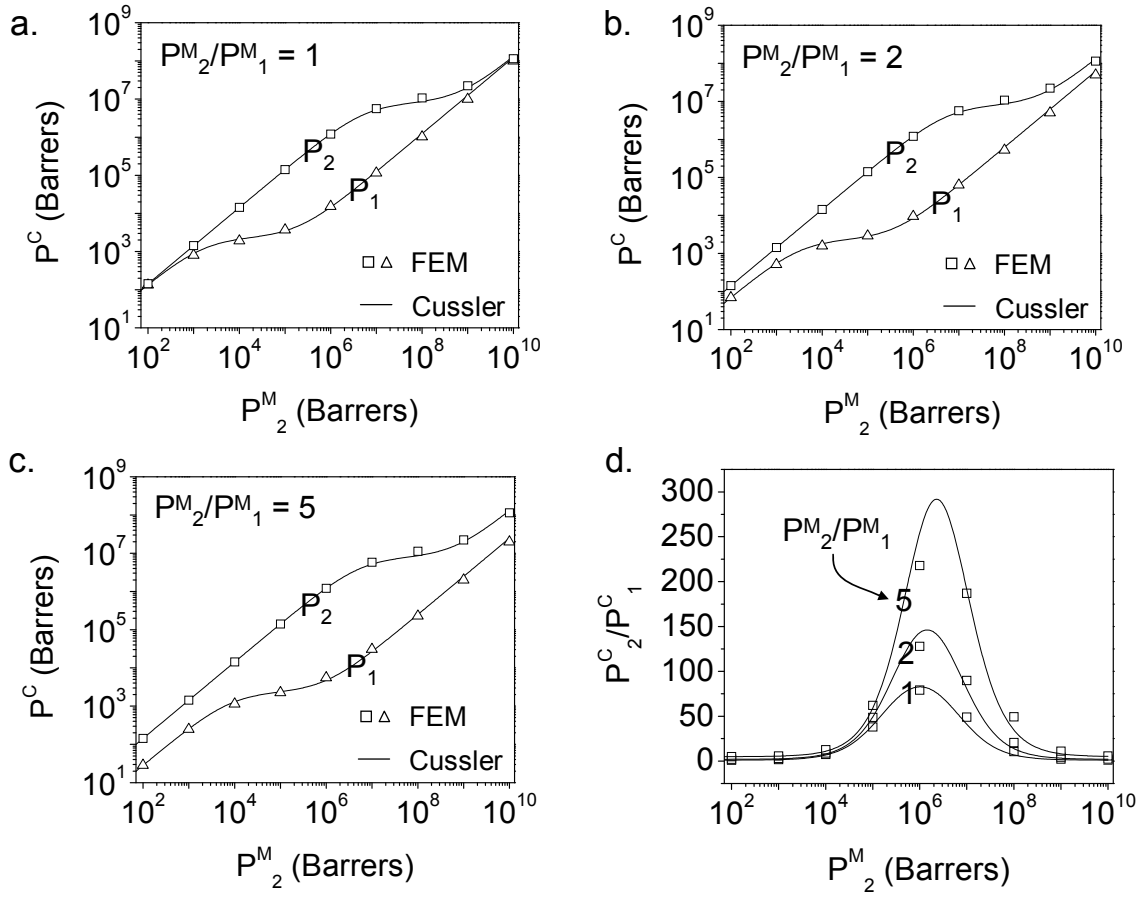

Figure 3.9: Predictions for the performance of a mixed matrix membrane containing flakes with an aspect ratio of α = 50 and loading of ϕ = 30%. The feed composition is 50/50 and the total feed and permeate pressures are p_t^{feed} = 1 kPa and $p_t^{permeate}$ = 0 kPa. Open symbols are the result of finite element calculations (FEM) for a membrane with a constant-permeability matrix and flakes which are governed by the Maxwell-Stefan equation. The curves are the predictions of the Cussler model, where both matrix and flake have constant permeabilities. The flake permeabilities used in the Cussler model were those of a silicalite-1 membrane with a 50/50 feed and p_t^{feed} = 0.5 kPa and $p_t^{permeate}$ = 0.25 kPa.

Utility of hybrid approach for membrane and process design

Separation of butanes by membranes containing silicalite-1

The usefulness of an accurate and quick method for predicting the performance of a mixed matrix membrane can be illustrated through a simple case study. Consider

the design of a mixed matrix membrane for the separation of normal and iso-butane using silicalite-1 flakes. With the flake material already in mind, the remaining important design parameters include membrane geometry, matrix material, and operating conditions. The hybrid method outlined above provides guidance for choosing each of these parameters.

The effect of mixed matrix membrane geometry is straightforward and is easily seen from the analytical expressions reviewed earlier. Selectivity is an increasing function of flake loading according to all three models. The Cussler and modified Cussler models both predict that increasing aspect ratio has a positive effect on mixed matrix membrane selectivity.

To gain insight into the proper choice of matrix material, imagine that silicalite-1 flakes with an aspect ratio of 50 are available and that a target operating pressure of 100 kPa feed with a 50/50 composition is set. Because we have already found average permeabilities for silicalite-1 that can be used to predict the performance of a mixed matrix membrane under these conditions, we can be confident in using these values with the Cussler model for design purposes. Figure 3.10 shows a plot of mixed matrix membrane selectivity as a function of matrix permeability and selectivity according to the Cussler model for a membrane with 30 volume percent flakes with an aspect ratio of 50. The flake permeability is calculated at 50 kPa feed and 25 kPa permeate pressure. Any point on this surface represents a specific membrane with a certain matrix permeability and selectivity (given by the x and y coordinates, respectively), and the corresponding color gives the selectivity of such a membrane. This figure provides guidance about how to choose from among a library of matrix materials in order to obtain a mixed matrix membrane with good selectivity. Of course, a more selective matrix will result in a more selective mixed matrix membrane, and this can be seen in the figure by noting that selectivity increases from bottom to top for any matrix permeability. The dependence of mixed matrix selectivity on matrix permeability is somewhat more complex, being characterized by an optimum matching, as already

mentioned above and widely recognized in the literature. At any given matrix selectivity there is a single value of matrix permeability that maximizes mixed matrix membrane selectivity. For every matrix selectivity in Figure 3.10, this optimum matrix permeability is marked by a blue point. The locus of all such points appears as a blue line in Figure 3.10. This line runs down the ridge of the mixed matrix membrane selectivity surface and provides a guide to where the best mixed matrix membrane selectivities can be found, with the most selective membranes found on the upper right end of the line. For a given set of flake properties, this "ridgeline" provides a shorthand way of conveying much of the important information from Figure 3.10 – the location of optimum matrix permeability for any matrix selectivity. From the point of view of mixed matrix membrane design, Figure 3.10 indicates that if silicalite-1 flakes with an aspect ratio of 50 are available, it is advisable to choose a matrix material with a permeability somewhere around 1000 Barrers in order to maximize selectivity at 100 kPa feed pressure. Use of a modestly selective matrix (less than 10) should offer the hope of realizing a mixed matrix selectivity in the hundreds under these conditions.

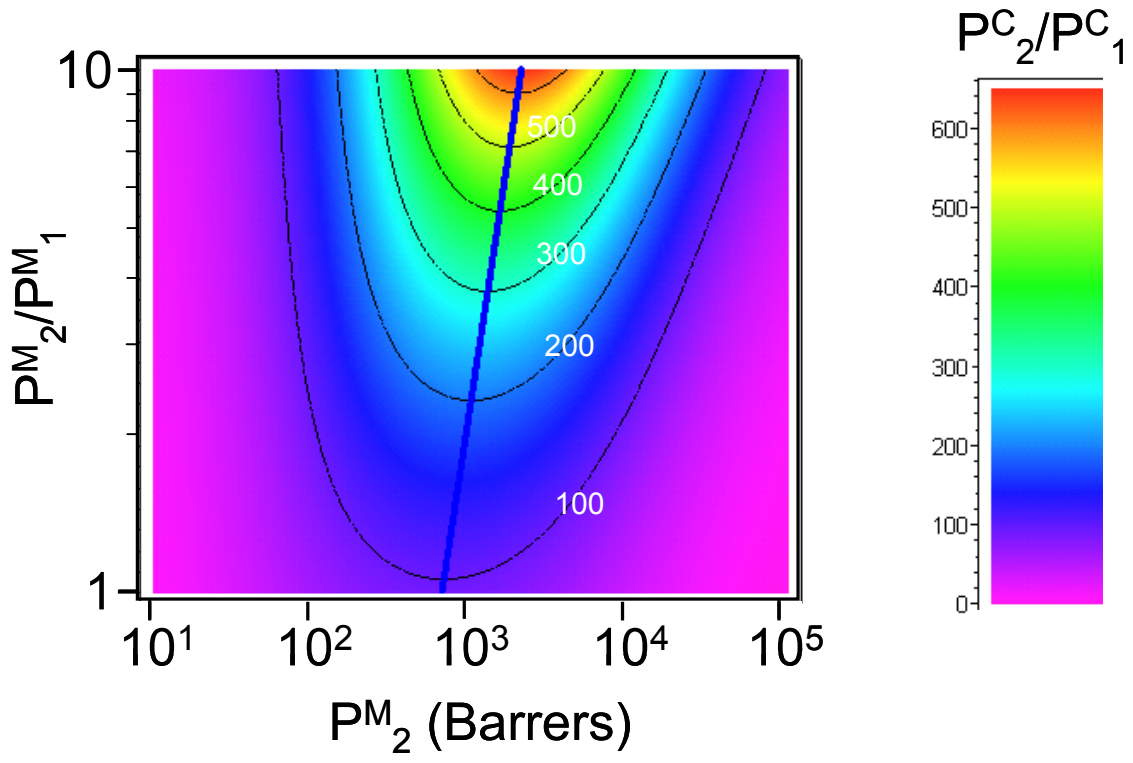

Figure 3.10: Predictions of the selectivity (P_2^C/P_1^C) of a mixed matrix membrane containing flakes with an aspect ratio of α = 50 and loading of ϕ = 30% as a function of matrix permeability (P_2^M) and selectivity (P_2^M/P_1^M). The feed composition is 50/50 and the total feed and permeate pressures are p_t^{feed} = 100 kPa and $p_t^{permeate}$ = 0 kPa. The flake permeabilities used in the Cussler model were those of a silicalite-1 membrane with a 50/50 feed and p_t^{feed} = 50 kPa and $p_t^{permeate}$ = 25 kPa. The colors represent the selectivity of the mixed matrix membrane that would result from forming a membrane using a matrix with a given permeability (*x*-axis) and selectivity (*y*-axis). A color key is provided at right. The black lines are contours of constant mixed matrix membrane selectivity.

Figure 3.10 and others like it give guidance about how to best choose a matrix material in order to optimize mixed matrix membrane selectivity. However, they do not offer any information about which matrix materials are actually experimentally available. For polymeric materials, the Robeson upper bound curve is a convenient way of presenting this information [36]. This upper bound is a straight line on a log-log plot of polymer selectivity versus permeability for a given gas pair, above and to the right of which no polymeric materials with the given selectivity and permeability are

experimentally known. The relationship between the Robeson line and the mixed matrix selectivity ridgeline provides insight into the practicality of using a given flake for a specific separation. For instance, if the Robeson line and the selectivity ridgeline do not intersect at a point where the Robeson line is populated with polymeric materials, the advisability of using the particular flake and/or operating conditions under consideration is questionable. On the other hand, if the Robeson line and the selectivity ridgeline do intersect at a point where polymeric materials are available, this point will provide guidance about which polymer to choose.

Figure 3.10 is useful for determining the optimum matrix material for a given set of flake permeabilities, but it does not provide insight into the effect that a change in these permeabilities might have on mixed matrix membrane performance. We have pointed out above that such a change is accomplished any time the average pressure within the mixed matrix membrane is changed – for instance, when the feed pressure is adjusted. Figure 3.9 demonstrated the ability of our method to accurately predict the performance of a mixed matrix membrane at various feed pressures, so we can confidently construct surfaces analogous to Figure 3.10 at any pressure. Because such an exercise would require as many figures as feed pressures, a more streamlined approach is taken in Figure 3.11, where only the ridgelines are presented for mixed matrix membranes operating at various feed pressures. This figure provides a quick illustration of how the optimum matrix properties change when the feed pressure is adjusted. At lower feed pressure, the effective permeability of the flakes increases. This can clearly be seen from Figure 3.5, where the average permeabilities that were used to construct the ridgeline plot can be found. The implication of this for mixed matrix membrane design is that a set of materials that are optimized for one set of operating conditions may not be optimized for a different set. Conversely, for a given set of materials (matrix and flake), the operating conditions may be used as a dial to achieve better performance.

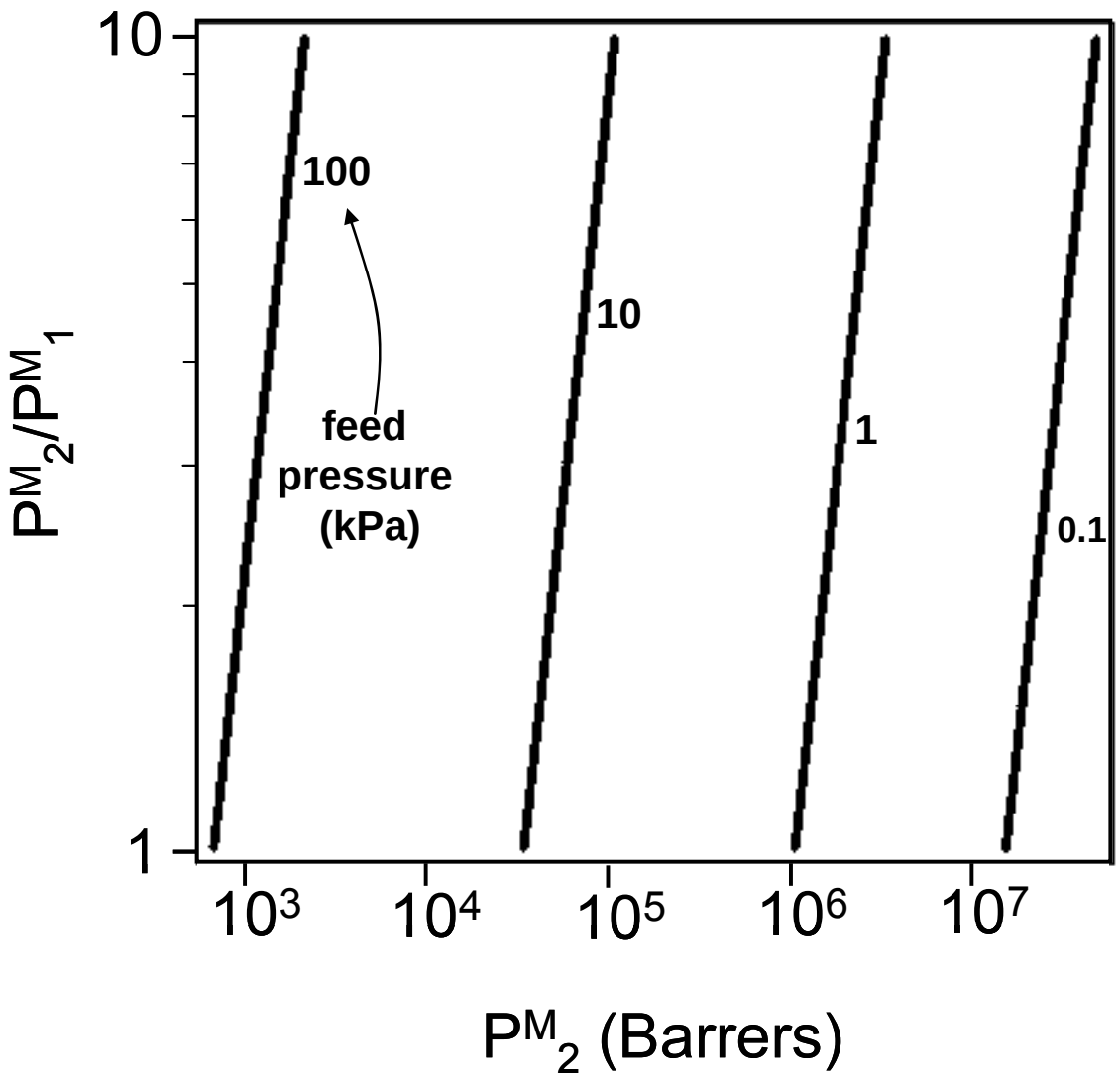

Figure 3.11: Selectivity ridgelines for a mixed matrix membrane containing flakes with an aspect ratio of α = 50 and loading of ϕ = 30% at various feed pressures for 50/50 feed composition and $p_t^{permeate}$ = 0 kPa according to the Cussler model.

Woo *et al.* reported normal and iso-butane permeability and selectivity for a mixed matrix membrane consisting of silicalite-1 flakes dispersed in PTMSP polymer [27]. These results can be compared with the predictions made here. The PTMSP permeability was measured in the experimental study, and Figure 3.12 shows these matrix properties as a data point on the selectivity surface for a membrane containing silicalite-1 flakes with an aspect ratio of five at 30 volume percent loading. As this

figure shows, the selectivity prediction for such a membrane is 13. A finite element calculation for this membrane using Maxwell-Stefan modeling for the flakes and the measured PTMSP permeabilities for the matrix yields a selectivity prediction of 15.6. Woo fabricated membranes of this approximate geometry, and the reported selectivities were in the neighborhood of 5. The agreement with the predictions presented here is not good, but given the uncertainties both in the modeling and the experiment, very close agreement can hardly be expected. The model, for instance, assumes perfect alignment and a regular flake arrangement, and while there is some evidence that this was achieved in part by the experiments, the real membranes at best approximate the idealized geometry. Perhaps more important is an issue not addressed at all by the modeling, and that is the effect of the dispersed particles on the permeability of the polymer. It is conceivable, and indeed has been suggested many times, that the presence of the dispersed phase in a mixed matrix membrane could affect the polymer matrix by creating significant amounts of interface region, which might have properties that are appreciably different from that of the neat polymer. The presence of a de facto third phase is not considered in the modeling presented here, but could be a contributing factor to the performance of the experimental membranes.

Apart from the model's relative degree of success for predicting the selectivity of the experimental membranes reported by Woo *et al*., this approach may still provide some interesting insights into design for this particular system. For instance, PTMSP is generally regarded as a very high-permeability polymer, and this high permeability is often considered a virtue because of its ability to yield high permeation fluxes. As Figure 3.12 shows, in this case it is possible that PTMSP is slightly *too* permeable, and a slight decrease in matrix permeability might be desirable for this application. The use of a different matrix polymer is one way to achieve this, but, as highlighted above, a change in operating pressure is another. For instance, at a feed pressure of 10 kPa, the selectivity prediction for this membrane is 22. Of course, a smaller feed pressure will result in a smaller flux, and how best to negotiate this compromise will depend on other considerations.

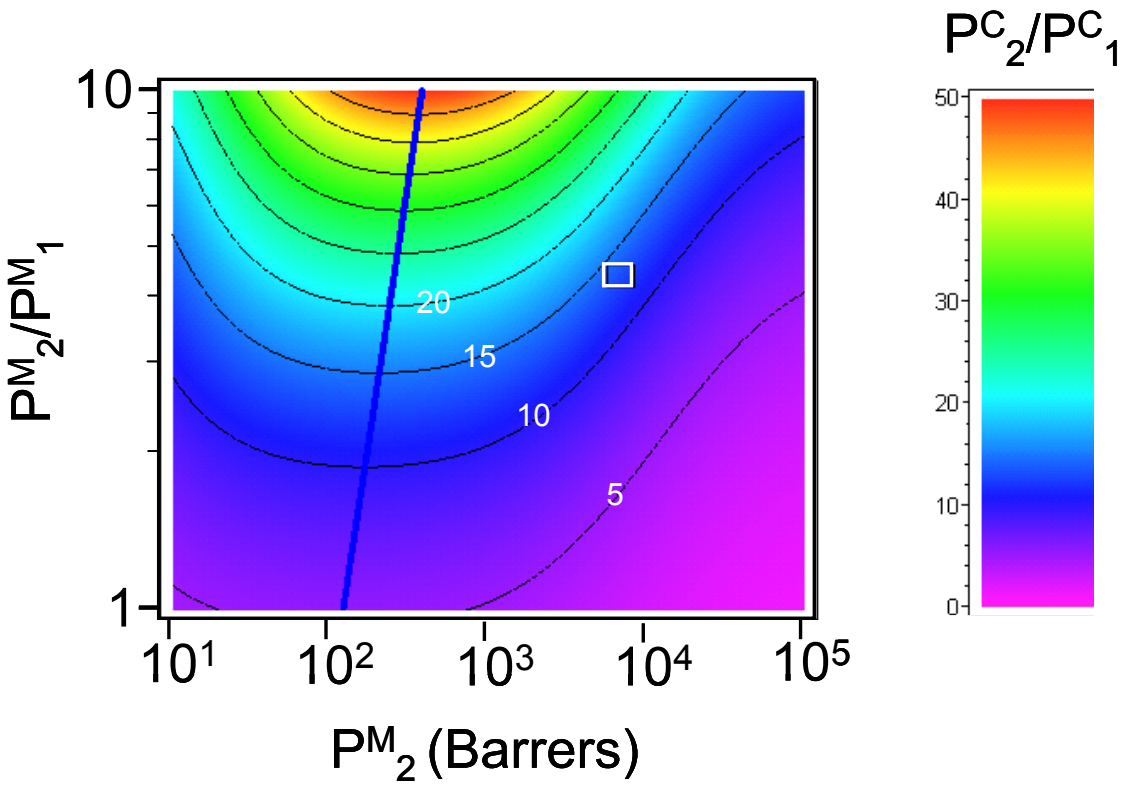

Figure 3.12 Predictions of the selectivity (P_2^C/P_1^C) of a mixed matrix membrane containing flakes with an aspect ratio of α = 5 and loading of ϕ = 30% as a function of matrix permeability (P_2^M) and selectivity (P_2^M/P_1^M). The feed composition is 50/50 and the total feed and permeate pressures are p_t^{feed} = 100 kPa and $p_t^{permeate}$ = 0 kPa. The flake permeabilities used in the modified Cussler model were those of a silicalite-1 membrane with a 50/50 feed and p_t^{feed} = 50 kPa and $p_t^{permeate}$ = 25 kPa. The white square corresponds to the permeability and selectivity of PTMSP at room temperature [27]. The corresponding mixed matrix membrane selectivity prediction is 13 according to the modified Cussler model, and the experimental membrane showed a selectivity of approximately 5.

Separation of carbon dioxide and methane by membranes containing CHA-type zeolite

Another opportunity for exploring the utility of this approach is present in the separation of carbon dioxide and methane by mixed matrix membranes containing CHA-type zeolites. The data necessary to calculate the permeability of CHA to carbon dioxide and methane is available in MD and GCMC simulations for all-silica CHA [84, 108] and in experimental permeation data for SAPO-34 membranes [45, 83]. (SAPO-

34 is an aluminophosphate material with the CHA structure type.) The data gathered from simulation studies on all-silica CHA is given in Tables 3.3 and 3.4. For this system, the loading dependence of the Maxwell-Stefan diffusivity is well predicted by the Reed-Ehrlich method [77, 80], as demonstrated in several publications [82-84]. The exchange coefficients, D_{ij}, can be assumed infinite [83, 84].

Table 3.3: Three-site Langmuir adsorption parameters for carbon dioxide and methane in CHA from [82, 108].

	q_A (mol g^{-1})	b_A (kPa^{-1})	q_B (mol g^{-1})	b_B (kPa^{-1})	q_C (mol g^{-1})	b_C (kPa^{-1})
CO_2	0.00693	5.21×10^{-3}	0.00173	1.02×10^{-4}	0.00173	1.17×10^{6}
CH_4	0.00277	1.72×10^{-3}	0.00416	2.70×10^{-5}	0.00139	9.00×10^{-7}

Table 3.4: Diffusion and Reed-Ehrlich parameters for carbon dioxide and methane in CHA from [84].

	$D_i(0)$ (m^2 s^{-1})	z	ϕ	q_i^{sat} (mol g^{-1})
CO_2	2.1×10^{-9}	5	1.47	0.01039
CH_4	2.1×10^{-11}	5	$4.55\exp(-0.98)$	0.00832

The already-mentioned challenge presented by the uncertainty of zeolite diffusivities values, which was illustrated in Figure 3.6 for butanes, is also a concern for this system. For example, consider the experimental data of Li *et al.* [45, 83] on SAPO-34 membranes. In a 2005 study, these authors calculated the Maxwell-Stefan diffusivities based on single-component permeation data, and the value for carbon dioxide (7.6×10^{-11} m^2 s^{-1}) is 27 times lower than the value listed in Table 3.4. In a 2007 report, "transport coefficients" were calculated, from which diffusion coefficients can be backed out, assuming an appropriate membrane thickness. The authors do not state the membrane thickness, but do comment that the membranes are thinner than those used in the 2005 study. Assuming a 2 μm-thick membrane (the 2005 membrane

was 5 μm), the corresponding carbon dioxide diffusivity is 2.0 x 10^{-11} m^2 s^{-1}, 100 times smaller than the value listed in Table 3.4. While this uncertainty in zeolite diffusivities is certainly a hindrance to the application of the method presented here for quantitative prediction of mixed matrix membrane performance, it is a hindrance to the more simple methods as well. In both cases, an estimate of zeolite permeability is necessary.

Uncertainties in the diffusivity data notwithstanding, the calculated permeability of CHA as a function of pressure (using the data from Tables 3.3 and 3.4) is shown in Figure 3.13. An interesting feature of this figure is that CHA selectivity under these conditions is a function of feed pressure. The minimum in the selectivity curve has its origins in the loading dependence of the Maxwell-Stefan diffusivity according to the Reed-Ehrlich model. As loading inside the framework increases from zero to around 4.5 molecules/unit cell (at a pressure of approximately 300 kPa), the diffusivity of methane increases while the diffusivity of carbon dioxide stays roughly the same (see Figure 7 in [84]). Meanwhile, adsorption selectivity remains constant up to a pressure of around 200 kPa, at which point it begins to increase (see Figure 5 in [108]). The overall membrane selectivity falls with diffusion selectivity at low pressure, and rises again as adsorption selectivity becomes dominant.

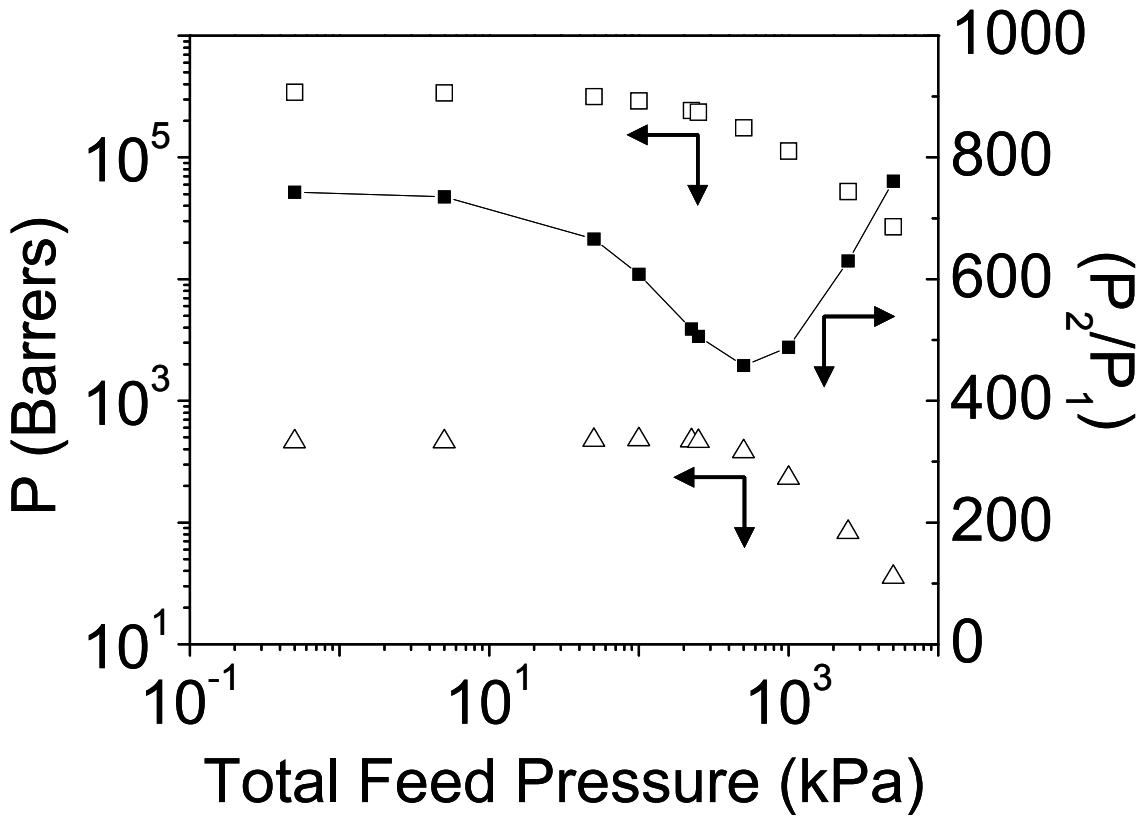

Figure 3.13: Calculated permeability of a CHA membrane to carbon dioxide and methane as a function of feed pressure for a 50/50 feed mixture and a 50% pressure drop across the membrane according to the Maxwell-Stefan model.

The CHA permeabilities shown in Figure 3.13 were used in conjunction with the Maxwell model to predict the performance of a mixed matrix membrane containing 15 volume percent flakes with an aspect ratio of one. At a feed pressure of 448 kPa and a 50/50 feed composition, the calculated selectivity surface is shown in Figure 3.14. Consistent with the approach used for butanes in silicalite-1, the CHA permeabilities were obtained from calculations for a CHA membrane with a 50/50 feed composition at 224 kPa and a total permeate pressure of 112 kPa.

Figure 3.14 can provide guidance about how to choose a matrix polymer in order to form a highly selective mixed matrix membrane. The carbon dioxide/methane permeability properties of known polymers are conveniently represented by Robeson's 1991 upper bound curve, which is shown as a red line on Figure 3.14. No polymers

with properties which fall above this line are known. Unfortunately, Figure 3.14 shows that there is no point below the upper bound curve for which a mixed matrix membrane with this geometry (ϕ = 15% and α = 1) and operating conditions (P_{total}^{feed} =448 kPa) is expected to offer significant selectivity improvements over the neat matrix polymer. The area of significant improvement lies entirely above Robeson's upper bound. While the use of the lower diffusivity values derived from SAPO-34 membranes will bring the selectivity ridgeline to lower values of matrix permeability, the overall situation is not significantly different.

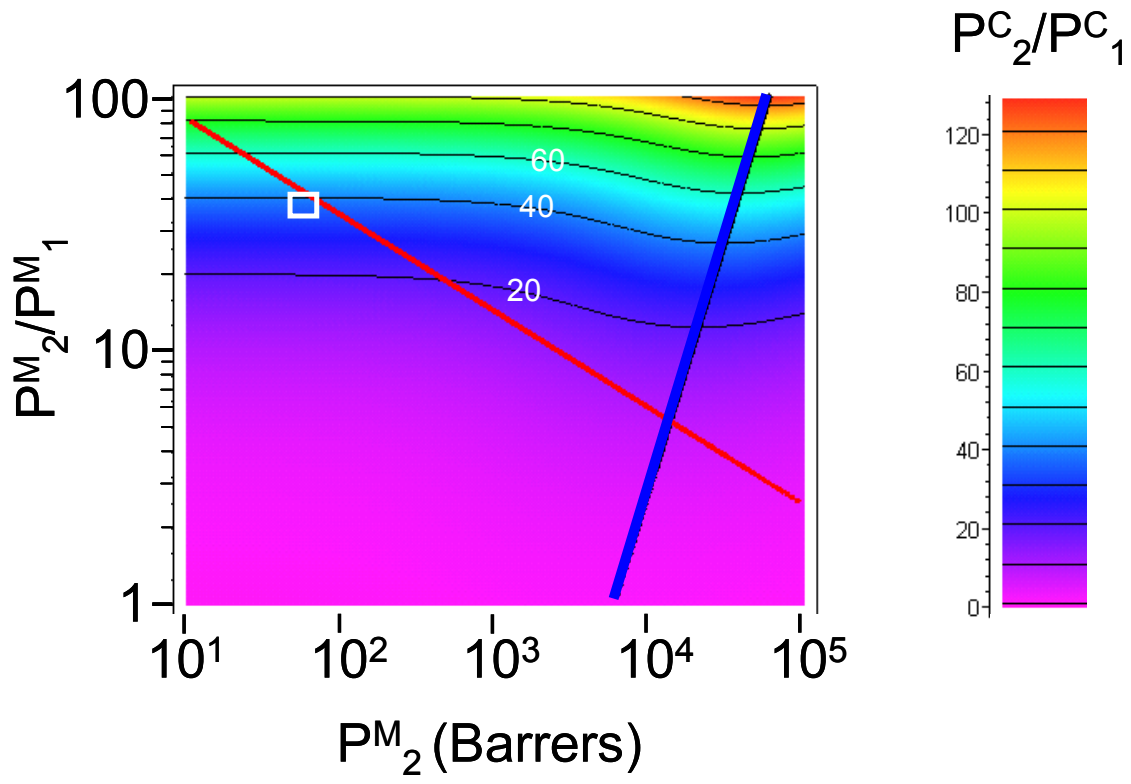

Figure 3.14: Predictions of the CO_2/CH_4 selectivity (P_2^C/P_1^C) of a mixed matrix membrane containing dispersed CHA particles at a loading of ϕ = 15% as a function of matrix permeability (P_2^M) and selectivity (P_2^M/P_1^M). The feed composition is 50/50 CO_2/CH_4 and the total feed and permeate pressures are p_t^{feed} = 448 kPa and $p_t^{permeate}$ = 0 kPa. The flake permeabilities used in the Maxwell model were those of a CHA membrane with a 50/50 feed and p_t^{feed} = 224 kPa and $p_t^{permeate}$ = 112 kPa. The white square corresponds to the permeability and selectivity of PDMC at room temperature [109]. The red line is Robeson's upper bound [36].

The principles already mentioned for the butanes case study provide some guidance about how to improve the chances of forming a mixed matrix membrane with CHA-type zeolite that offers dramatic selectivity enhancement. First, the aspect ratio of the particles should be increased. The importance of large aspect ratio particles to mixed matrix membranes is obvious and well known, but we wish to highlight the dire necessity of using large aspect ratio particles for this particular application. Without them, the selectivity improvements possible by adding CHA zeolite to an available

polymer are modest at best and perhaps negligible. Second, high permeability polymers should be used. (The 1991 Robeson curve is populated with polymers up to a permeability of about 3 x 10^4 Barrers.) Even with a high permeability polymer, significant improvements in selectivity will not be possible if the mixed matrix membrane is not operated at conditions which minimize the effective permeability of the zeolite. Therefore, high operating pressure is advisable, as suggested by Figure 3.13. Combining these insights, Figure 3.15 shows the predictions for a mixed matrix membrane containing 30 volume percent of CHA flakes with an aspect ratio of 30 operating at a feed pressure of 10^4 kPa. Under these conditions, it appears that significant selectivity enhancements are possible. For instance, a polymer with a carbon dioxide permeability of 3 x 10^4 Barrers and a selectivity of 4 offers the hope of a mixed matrix membrane with a selectivity of 80.

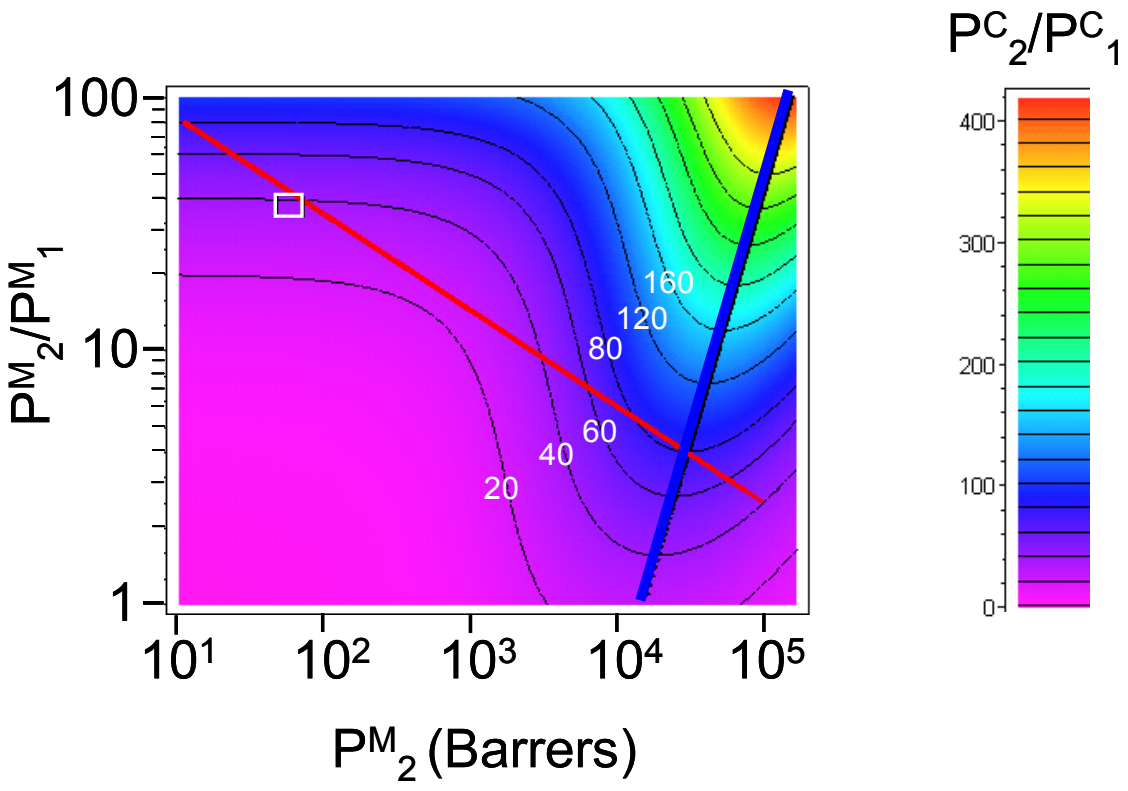

Figure 3.15: Predictions of the CO_2/CH_4 selectivity (P_2^C/P_1^C) of a mixed matrix membrane containing dispersed CHA particles at a loading of ϕ = 30% and an aspect ratio of α = 30 as a function of matrix permeability (P_2^M) and selectivity (P_2^M/P_1^M). The feed composition is 50/50 CO_2/CH_4 and the total feed and permeate pressures are p_t^{feed} = 10^4 kPa and $p_t^{permeate}$ = 0 kPa. The flake permeabilities used in the Maxwell model were those of a CHA membrane with a 50/50 feed and p_t^{feed} = 5,000 kPa and $p_t^{permeate}$ = 2,500 kPa. The white square corresponds to the permeability and selectivity of PDMC at room temperature [109]. The red line is Robeson's upper bound [36].

An opportunity to compare this analysis to an experimental study exists in the recent report by Hillock *et al.* [109] on the fabrication and permeation testing of an SSZ-13/crosslinked polymer (PDMC) mixed matrix membrane for the separation of carbon dioxide and methane. In this work, the authors fabricate a mixed matrix membrane containing SSZ-13 (an aluminosilicalte with CHA structure) dispersed in a crosslinked polymer with an inherent carbon dioxide/methane selectivity of 37.1. Data for two different membranes is presented – one made with SSZ-13 primed with

unmodified PDMC polymer and one made with a silane coupling agent. The first membrane shows a selectivity of 44 and no change in permeability from the neat polymer, and the other shows a selectivity of 42 along with a dramatic increase in permeability. The experimental membranes were operated at 448 kPa feed and can be compared to the predictions of Figure 3.14. The properties of the PDMC polymer are shown on this figure by a white box, and the associated selectivity prediction (37.2) is essentially identical to that of the matrix. The reason for this is the extreme mismatch in the matrix and flake permeabilities under these conditions, as explained above.

While these calculations predict negligible selectivity improvement for these mixed matrix membranes, the experimental membranes did show some enhanced selectivity (44 and 42, for the two different membranes). However, one of the experimental membranes showed a large permeability increase, from 57.5 Barrers for carbon dioxide in the neat matrix to 88 Barrers in the composite. This large permeability increase accompanied by a selectivity increase is difficult to explain by any model. For example, 88 Barrers is approximately equal to the Maxwell model prediction for the permeability of a membrane with 15 volume percent of uniformly distributed void space ($P_{CO_2}^F \to \infty$). This unexpected increase in permeability led the authors to speculate about the possibility of poor adhesion between the polymer matrix and the SSZ-13 particles. This, along with several of the factors mentioned for the case of Woo *et al.*, could contribute to the difference between the predictions of Figure 3.14 and the data of Hillock *et al.*

That some of the permeation data from this report cannot be qualitatively explained by either the model presented in this work or the more simple Maxwell analytical model highlights the fact that at this stage experimental membranes differ from the idealized models in many ways. There is work to do on both fronts. Theoretical models need to include both more of the relevant physics (as we try to contribute here) and a more accurate picture of experimental membrane geometry, perhaps including interfacial effects. Meanwhile, systematic studies that link well

characterized mixed matrix membrane microstructure to the experimental parameters that govern the formation of this microstructure will allow the rational design of membranes with the potential for exceptional performance.

3.5. Conclusions

Analytical equations for the prediction of mixed matrix membrane performance are limited in applicability by their various geometric assumptions. For the case of a uniform dispersion of oriented flakes with a selectivity of approximately 10,000, the regions of applicability of the Maxwell and Cussler models were mapped out according to flake aspect ratio and volume fraction. This was accomplished through comparison with two dimensional finite element calculations for mixed matrix membrane performance. It was found that for many moderate combinations of aspect ratio and volume fraction, neither model was accurate, and a modification to the Cussler model was proposed.

For zeolite flakes, permeability is a function of concentration. It was shown that an acceptable method of accounting for this concentration-dependence in mixed matrix membrane modeling involves finding an average flake permeability, this average permeability being a function of operating conditions. The mixed matrix membrane operating conditions and the conditions at which the flake properties are evaluated should not be the same but should in some sense be corresponding. A method for finding these corresponding conditions was illustrated for the case of mixed matrix membranes containing silicalite-1 flakes for the separation of normal and iso-butane. This method was verified by comparison with finite element calculations.

The utility of this model was discussed as it relates to mixed matrix membrane material as well as process design. The predictions of this approach were compared to experimental results for a PTMSP/silicalite-1 membrane for the separation of normal and iso-butane. Agreement was at best modest, and some reasons for this were proposed.

Finally, a second case study was presented, involving the separation of carbon dioxide and methane by mixed matrix membranes containing CHA-type zeolites. The permeability of CHA to these gases was calculated and used to predict the performance of mixed matrix membranes containing these materials. It was argued that very high permeability polymers should be used to fabricate membranes with the potential for dramatic selectivity improvements, and this requirement was considered in light of Robeson's upper bound curve of available polymer properties. Guided by principles developed earlier, the design of a potentially high performing mixed matrix membrane was given, containing high aspect ratio CHA flakes imbedded in a high permeability polymer and operated at high pressure. The predictions for mixed matrix membrane performance were compared to experimental results for an SSZ-13/crosslinked polymer membrane.

Chapter 4. Inorganic Mixed Matrix Membrane Fabrication

4.1. Abstract

Previous chapters have shown that for some separations, the use of zeolites as the selective phase in mixed matrix membranes will require matrix permeabilities that exceed the upper limit of available polymeric materials. Because it is available with various pore sizes and porosities, porous silica is a candidate matrix material in these cases. The deposition of alternating strata of zeolite particle layers and porous silica films by a layer-by-layer method could result in a desirable mixed matrix membrane microstructure. In this chapter, I describe efforts to fabricate a silicalite-1/mesoporous silica mixed matrix membrane using layer-by-layer deposition. Successful formation of *b*-oriented layers of very high aspect ratio silicalite-1 is reported, but deposition of defect-free silica films covering these layers proved elusive.

4.2. Introduction

While the mixed matrix membrane literature is dominated by reports of membranes composed of a selective phase dispersed in a polymer matrix, other choices of matrix material are available. Some of the results of Chapters 2 and 3 suggest that for some separations, very high permeability matrices (relative to the available polymers) are necessary in order to form optimized membranes with zeolite flakes. Porous inorganic materials could be an alternative to polymers for the matrix phase in mixed matrix membranes. Specifically, the vast body of literature surrounding porous silica (see, for example, the review by Brinker and references therein [110]) makes it an attractive candidate to fill this role. Because different sol formulations can be used to adjust the porosity of silica films over a wide range of pore sizes (from microporous to mesoporous) and pore structures [111, 112], the permeability of these films could be manipulated to the desired value for a desired mixed matrix membrane application. That is, the silica matrix could be formulated in such a way that it "matches" the flake transport properties for a specific separation.

The formation of a mixed matrix membrane where porous silica serves as the matrix phase requires a convenient way of achieving the desired mixed matrix microstructure with these components. The formation of silica/zeolite composite films for application to chemical sensing has been reported by dispersal of small (< 3 μm) zeolite particles in a silica sol followed by dip coating and film gelation and consolidation onto solid supports [33]. This approach has the advantage of simplicity, but sedimentation would likely hinder its extension to systems involving larger zeolite particles. Choi *et al.* recently reported a layer-by-layer method for the formation of MCM-22 zeolite/mesoporous silica mixed matrix films that showed corrosion resistance barrier properties and selectivity for H_2 over larger gas molecules [113]. This method consisted of the deposition of alternating layers of high aspect ratio zeolite particles (MCM-22) and mesoporous silica, resulting in strata of zeolite plate-like particles dispersed in a mesoporous silica matrix.

The layer-by-layer method separates the zeolite particle and mesoporous silica depositions steps, alternating each in order to build up a highly stratified microstructure. For deposition of the mesoporous silica layers, the layer-by-layer method described above employs a slip coating procedure adapted by Lai *et al.* [114] from a recipe and method first reported by Lu *et al.* [115]. Of course, other methods for depositing silica films are known, including an aerosol approach [116, 117], and these could be incorporated into the layer-by-layer scheme.

The formation of zeolite particle coatings involves two phenomena: deposition of particles *on* the substrate and attachment of particles *to* the substrate. (Admittedly, while these phenomena are distinct in most cases, there are certainly others where the method of deposition and the means of attachment are conceptually difficult to separate.) For attachment, Choi *et al.* [113] employed covalent linkage between the particles and substrate, mediated by the use of alkyl halide groups that were used to functionalize the support. Deposition was achieved by two different methods developed by Yoon's group [118, 119]: one that involved placing the functionalized support in a

dispersion of zeolite particles in toluene under reflux and one that involved placing the functionalized support in a dispersion of zeolite particles in toluene with sonication. Other available methods for attachment include ionic linkage, mediated either by particle/substrate functionalization or by a polyelectrolyte layer [120] and hydrogen bonding, either by functionalization [121], an intermediate hydrogen-bonding polymer [122, 123], or directly through naturally-present -OH groups on the particle and support [123]. Besides the methods already mentioned, particle deposition has been reported by solvent evaporation [124], dip coating [125, 126], convective assembly [127], and physical rubbing [123].

In this chapter, I describe my efforts to apply the method of layer-by-layer deposition to the fabrication of mixed matrix films composed of high aspect ratio silicalite-1 (MFI structure type) particles dispersed in a porous silica matrix. The plate-like silicalite-1 particles are polydisperse in size, and are obtained by breaking up highly intergrown as-synthesized particles. A significant fraction are as large as 10 μm along their largest dimension. This is in contrast to the MCM-22 particles that were used in the study mentioned above; they are relatively monodisperse and approximately 1 μm along their largest dimension. Slip coating, aerosol coating, and spray coating were all explored for deposition of the silica layer. The zeolite layers are formed by sonication-assisted deposition and attachment by covalent linkage.

4.3. Experimental

Silicalite-1 Flake Synthesis

Very high aspect ratio silicalite-1 (high-silica MFI) particles were used as the flake phase in these membranes. These particles, which were first reported by Bonilla *et al.* [78], were synthesized by first dissolving dimmer-C5 tetrapropylammonium (dC5 TPA) structure directing agent in aqueous potassium hydroxide (1.0 N solution in water, Aldrich). The dC5 TPA (chemical formula $(C_3H_7)_3N^+(CH_2)_5N^+(C_3H_7)_3$) was synthesized in our lab by Jungkyu Choi and was used in its iodide salt form. The silica

source, tetraethylorthosilicate (TEOS, 98%, Aldrich) was added next, followed by stirring for 24 hours. The molar recipe of the synthesis solution was 40 TEOS : 7.5 dC5 TPAI : 25 KOH : 19000 H_2O. After stirring, the resulting clear solution was filtered into Tefon®-lined stainless steel autoclaves and placed in a 175°C oven for 5 days with rotation. The product was recovered by repeated centrifugations and washing with water. The solid product was dried in air overnight in an 80°C drying oven and then calcined in flowing air at a temperature of 525°C for 10 hours with a ramp rate of 1°C/minute.

Porous Support Preparation

The porous alumina disks that were used as supports were fabricated in our lab according to an established procedure described by Lai *et al.* [114].

Mesoporous silica sol formulation

Two separate mesoporous silica sols were used for deposition. The first, a CTAB-templated silica sol, was adapted by Lai *et al.* [114] for coating porous alumina supports from a recipe originally reported by Lu *et al.* [115]. The method for preparing this sol is described in detail in references [114, 117]. The final step in preparing this sol is dilution with anhydrous ethanol. Diluted sols were stored in a refrigerator and used for coating over the course of several months.

The second mesoporous silica sol was templated by Brij-56 surfactant and has been described in detail by Mabande *et al.* for aerosol deposition of silica films onto porous stainless steel [117] (see also [116]). The sol is formed by mixing water, Brij-56 surfactant (Sigma), TEOS (98%, Aldrich), and 0.07 M nitric acid in the molar ratio 1 SiO_2 : 4 EtOH : 120 H_2O : 0.14 Brij-56 : 0.0060 HNO_3. This mixture is sonicated for three hours and further aged on the bench for approximately 1.5 hours before being used.

Mesoporous silica deposition by slip coating

Slip coating of the CTAB-templated silica sol onto the appropriate substrates was accomplished by the method developed by Lai *et al.* and described in detail in a number of publications from our group [114, 117]. To summarize, the surface to be coated is horizontally immersed in the silica sol and held for 20 seconds. It is then slipped away from the sol horizontally and raised to a vertical position where it is held while the solvent evaporates. Substrates thus coated are calcined at 480°C in flowing air for 4 hours with a ramp rate of 1°C/minute.

Mesoporous silica deposition by aerosol coating

Aerosol deposition of silica films was accomplished according to the method reported by Mabande *et al.* [117]. The aged Brij-56-templated sol was placed in a sonicating humidifier (Kaz Inc. Model 5520) equipped with a 2 L chamber (open at the top) connected to the humidifier outlet. An open grate was placed at the bottom of the 2 L chamber, the chamber's top vent was loosely covered, and the humidifier was run for 5 minutes. This was done to minimize and start-up effects associated with filling the chamber with aerosol and/or deposition of sol onto the chamber walls. With the humidifier still running, the sample was then placed on the grate near the bottom of the chamber and the cover was loosely replaced. The sample was maintained in this position for the desired amount of time, after which it was removed and dried in a laminar flow hood for 10 minutes. Repeated cycles of coating followed, if desired. Finally, the films were calcined according to the procedure already described for the slip coating films.

Mesoporous silica deposition by spray coating

The CTAB-templated silica sol was spray coated onto supports using a 1 oz. atomizer/spray bottle (Target) filled with sol. The substrate was held with large tweezers at a 15° angle to the horizontal, and the atomizer was held 8-14 inches from the support surface. Sol was sprayed onto the surface continually until it appeared visually wet (flooded). The support was then placed in a laminar flow hood until it was

dry by sight, at least 10 minutes. Repeated coatings were performed, if desired. Again, calcination was performed as described for the slip coating films.

Particle deposition by sonication-assisted covalent linkage

Deposition of high aspect ratio silicalite-1 particles began with a silica-coated, calcined porous alumina support. The support surface was first functionalized by immersing it in a mixture of 40 mL dry toluene (anhydrous, 99.8%, Sigma-Aldrich) and 4 mL 3-chloropropyltrimethoxysilane (3CPTMS, 97+%, Aldrich) and heating it to reflux (~110°C) for three hours under the flow of dry argon (to avoid moisture). The support was then removed, rinsed in fresh toluene, and placed in a 120°C drying oven. The functionalization process is summarized schematically in Figure 4.1.

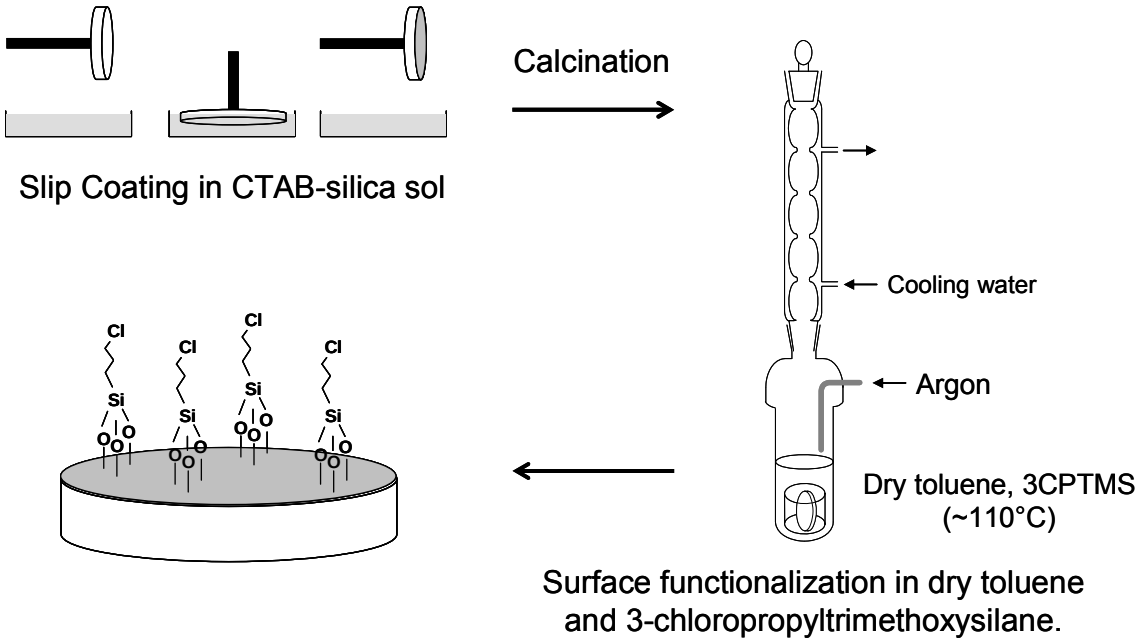

Figure 4.1: Schematic representation of support functionalization with 3-chloropropyltrimethoxysilane.

Next, a desired amount of calcined dC5-silicalite-1 was placed in 40 mL dry toluene and this mixture was sonicated (Branson 5510, 135 W, 42 kHz sonicator) for 1 hour to disperse the particles and break up large intergrowths. After sonication, the functionalized support was placed vertically in the toluene/zeolite suspension between

two glass cover-slips which were held in place by a home-made comb-like Teflon® holder. The support was sonicated for a desired amount of time in this position, after which it was placed in a horizontal position and sonicated again. This is summarized in Figure 4.2.

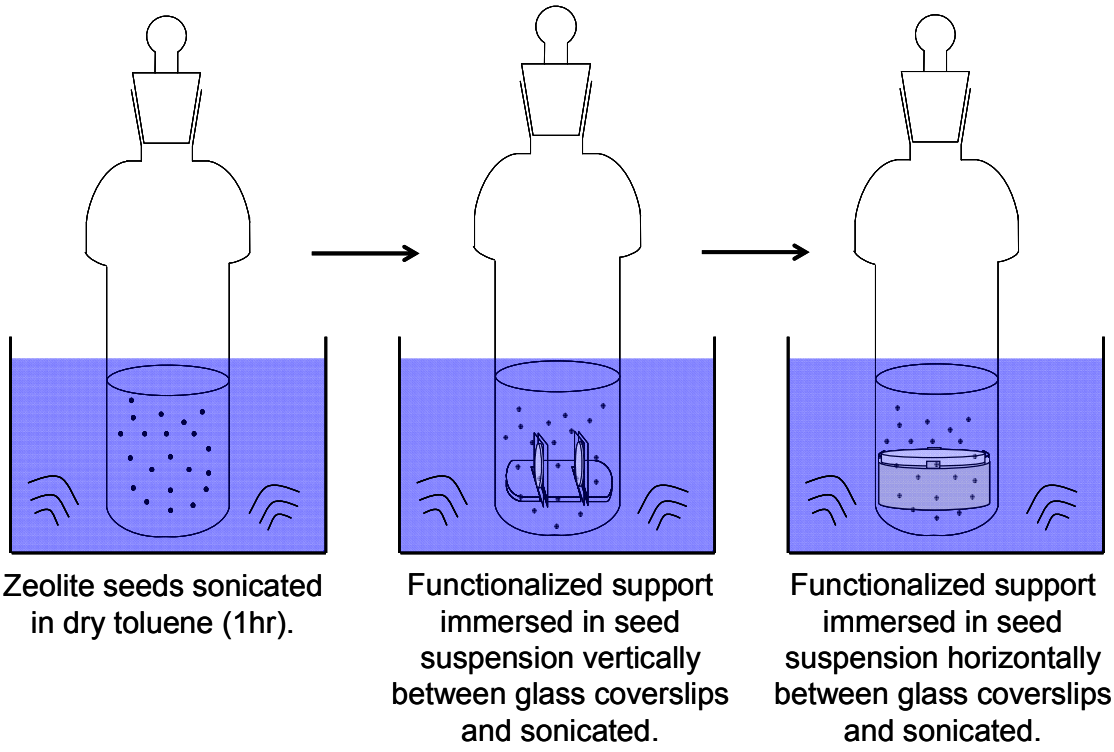

Figure 4.2: Schematic representation of particle deposition by sonication-assisted covalent attachment.

The support was rinsed by immersing it in fresh toluene several times and it was dried in a 120°C drying oven. Finally, supports were calcined at 480°C in flowing air for 4 hours with a ramp rate of 1°C/minute prior to further processing.

Permeation testing

Permeation testing of select membranes for mixed xylene isomers was performed in a permeation set-up described elsewhere [128]. Permeation tests were conducted in the Wicke-Kallenback mode. That is, the total pressure on both sides of the membrane (feed and permeate) was equal to 1 atm. Approximately 20 mL/min. of

He carrier gas was bubbled through separate 40°C *p*- and *o*-xylene bubblers, resulting in oversaturated streams. These streams were then passed through room-temperature condensers, resulting in saturated streams, with *p*- and *o*-xylene partial pressures of 0.5 and 0.4 kPa, respectively. Finally, these streams were mixed and fed to the permeation cell. The permeate stream was analyzed by an HP5890 GC equipped with a FID detector and a capillary column (EC-WAX, Alltech). CH_4 was used as an internal standard.

Characterization

X-ray diffraction (XRD) data was collected on Seimens D5005 diffractometer with a Cu source in a $\theta/2\theta$ geometry. Scanning electron microscope images were obtained using a JEOL 6500 FEG SEM. Some samples were Pt-coated before imaging.

4.4. Results and Discussion

Formation of dC5-silicalite-1 particle coatings

While complete monolayer coverage by zeolite particles is not absolutely vital to the fabrication of mixed matrix membranes (as it is for the formation of continuous zeolite membranes by secondary growth, for instance), good coverage by a near-monolayer of particles is the ideal. To determine the best conditions under which to achieve good coverage, the deposition parameters were explored. These parameters included the amount of time the functionalized support was sonicated with the particle suspension and the concentration of the particles in that suspension. Particle layers formed with various combinations of these parameters are shown in Figure 4.3. This figure shows that more concentrated solutions form more complete particle layers and that excessive sonication can be detrimental to the amount of coverage. Good coverage can be achieved with a particle suspension of 0.1 g silicalite-1 in 40 mL toluene and a sonication time of 4 minutes vertical/2 minute horizontal, as Figure 4.3E shows.

t \ c	0.01	0.05	0.1
1		B	
4	A	C	E
8		D	

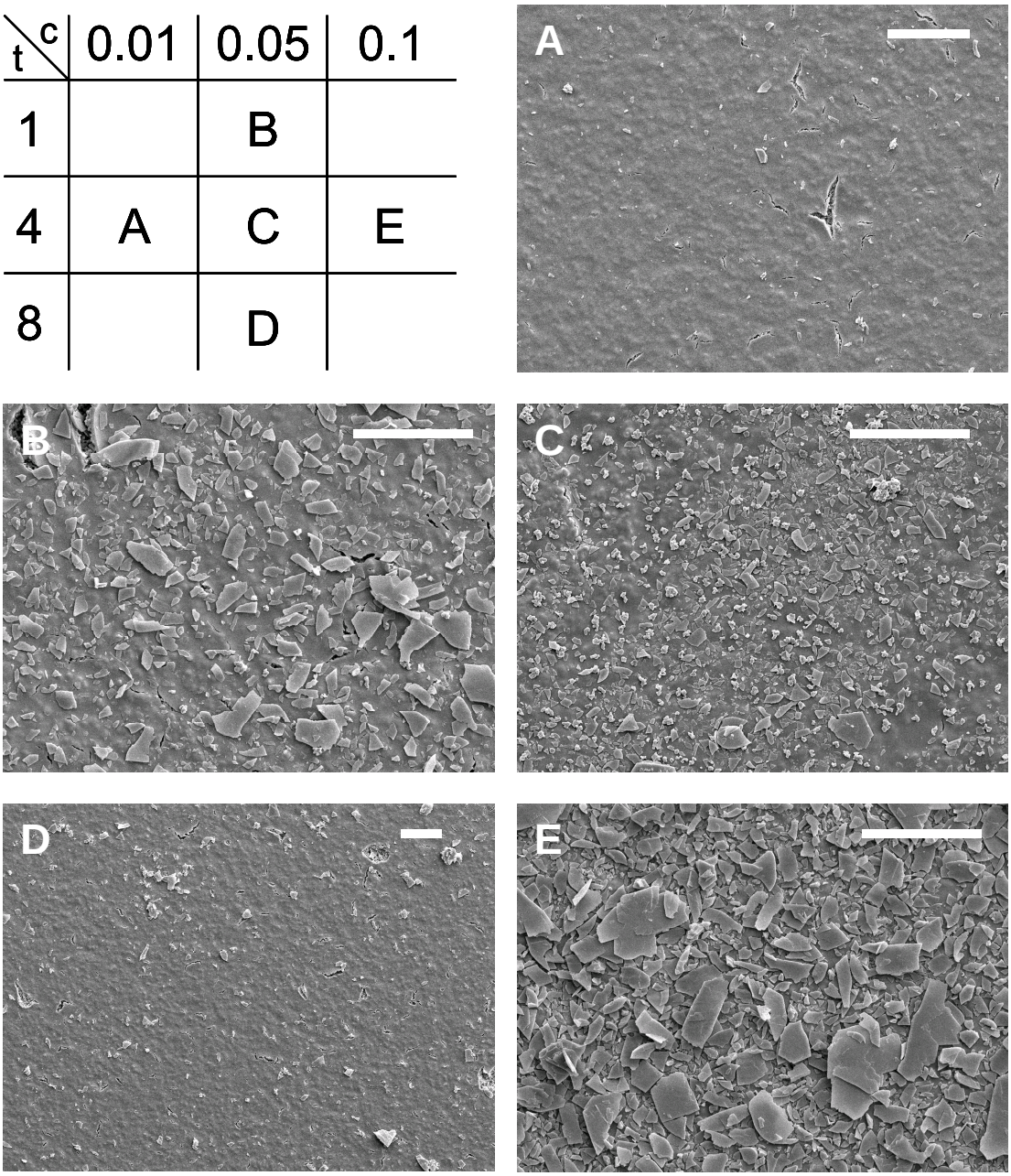

Figure 4.3: dC5-silicalite-1 particle layers formed by sonication-assisted covalent attachment under various conditions. The conditions corresponding to each image are indicated in the key, where the concentration of dC5-silicalite-1 particles used for deposition, c, is given in g silicalite-1/40mL toluene and the time of vertical sonication of the support is given in minutes. In every case, horizontal sonication was carried out for 2 minutes. All of the scale bars are 10 μm.

Because of the high aspect ratio of the dC5-silicalite-1 particles, it is not surprising that they appear to attach with their shortest dimension perpendicular to the support surface, as Figure 4.3 shows. A similar particle shape effect was shown to be important for forming oriented seed layers for subsequent formation of continuous, oriented zeolite films by secondary growth [73, 129]. In Figure 4.4 the *b*- orientation of these films is confirmed by x-ray diffraction, which is consistent with the fact that the *b*-axis of MFI runs along the thin dimension of dC5-silicalite-1 particles [78].

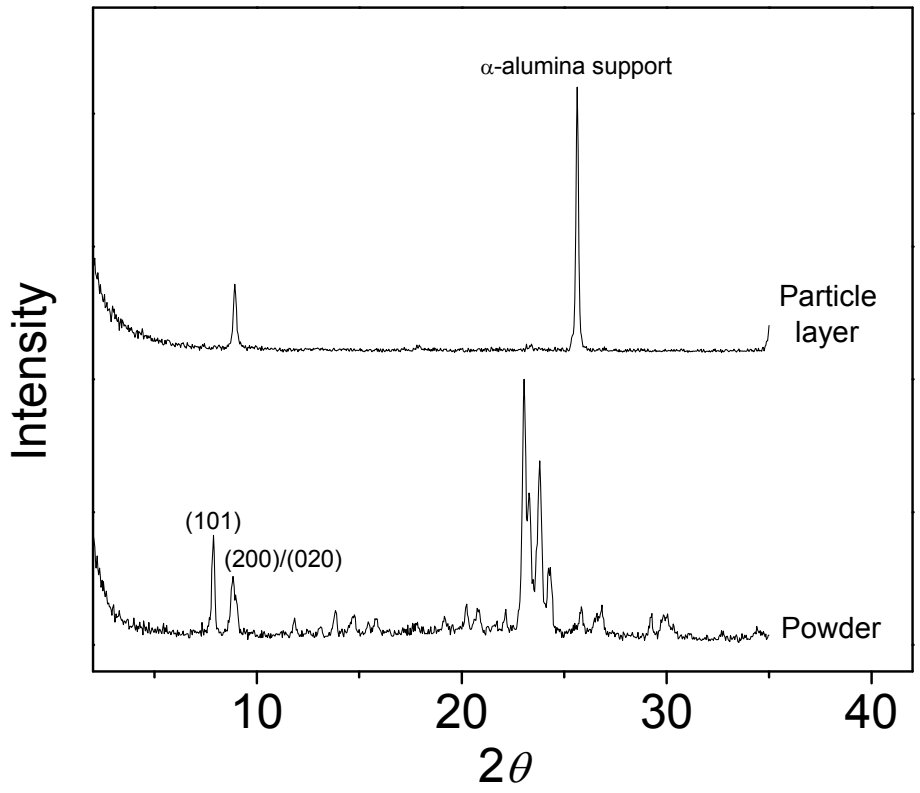

Figure 4.4: X-ray diffraction of dC5-silicalite-1 powder and a dC5-silicalite-1-coated support.

The formation of *b*-oriented particulate coatings of high aspect ratio silicalite-1 is an important component of the scheme outlined above for the formation of silica-MFI mixed matrix membranes.

Deposition of silica by slip coating

The deposition of surfactant templated silica onto dC5-silicalite-1 particulate coatings was attempted by three different methods: slip coating, aerosol coating, and spray coating. Because slip coating is the established method for depositing the very first silica layer (coating the porous supports prior to the first particle deposition), it is a natural choice for subsequent silica depositions as well. Figure 4.5 shows the SEM top views of three different particulate coatings that were treated according to the established slip coating procedure, using the CTAB-templated silica sol. This figure shows that slip coating results in a thin layer of silica which coats, but not completely cover, the silicalite-1 particles. This is particularly evident in Figure 4.5A, where it is clear that, while the particles appear to be somewhat coated as evidenced by a smoothening of their edges, the spaces between the particles are not filled. In places where particles overlap, defects in the silica coating appear to be present. Figure 4.5B is similar, if somewhat more severe. Figure 4.5C illustrates a second problem – the presence of small cracks around the particles' perimeters.

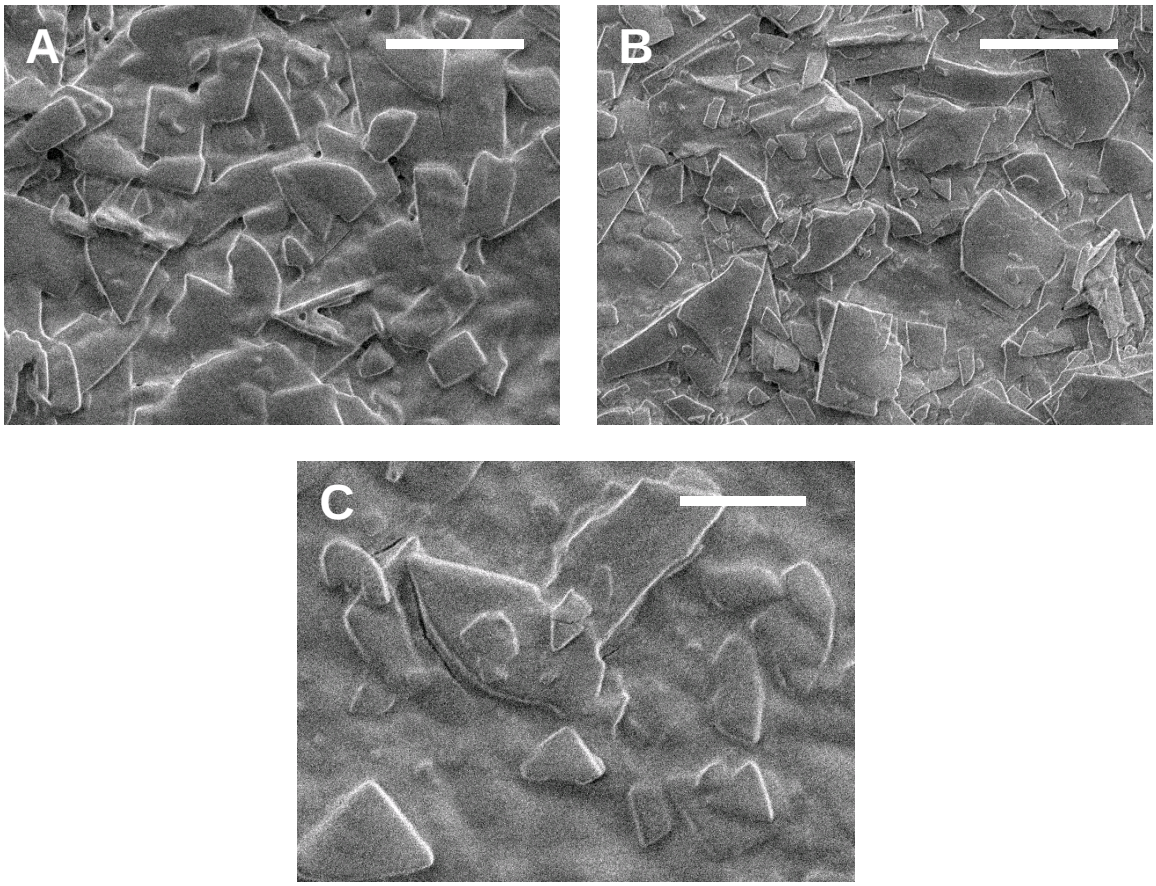

Figure 4.5: SEM images of silica films deposited by slip coating on top of dC5-silicalite-1 particulate coatings. All films have been calcined. All scale bars are 5 μm.

The problems evident from the top views of these films can be more fully appreciated by considering a slightly tilted side view, as shown in Figure 4.6. These images, taken at a different angle, are of the same film depicted in Figure 4.5C. Here it is obvious that the thin layer of silica deposited on top of the silicalite-1 particles is not sufficient provide a continuous covering. When silicalite-1 particles are overlapping, defects in the form of open pathways around and under the particles are present.

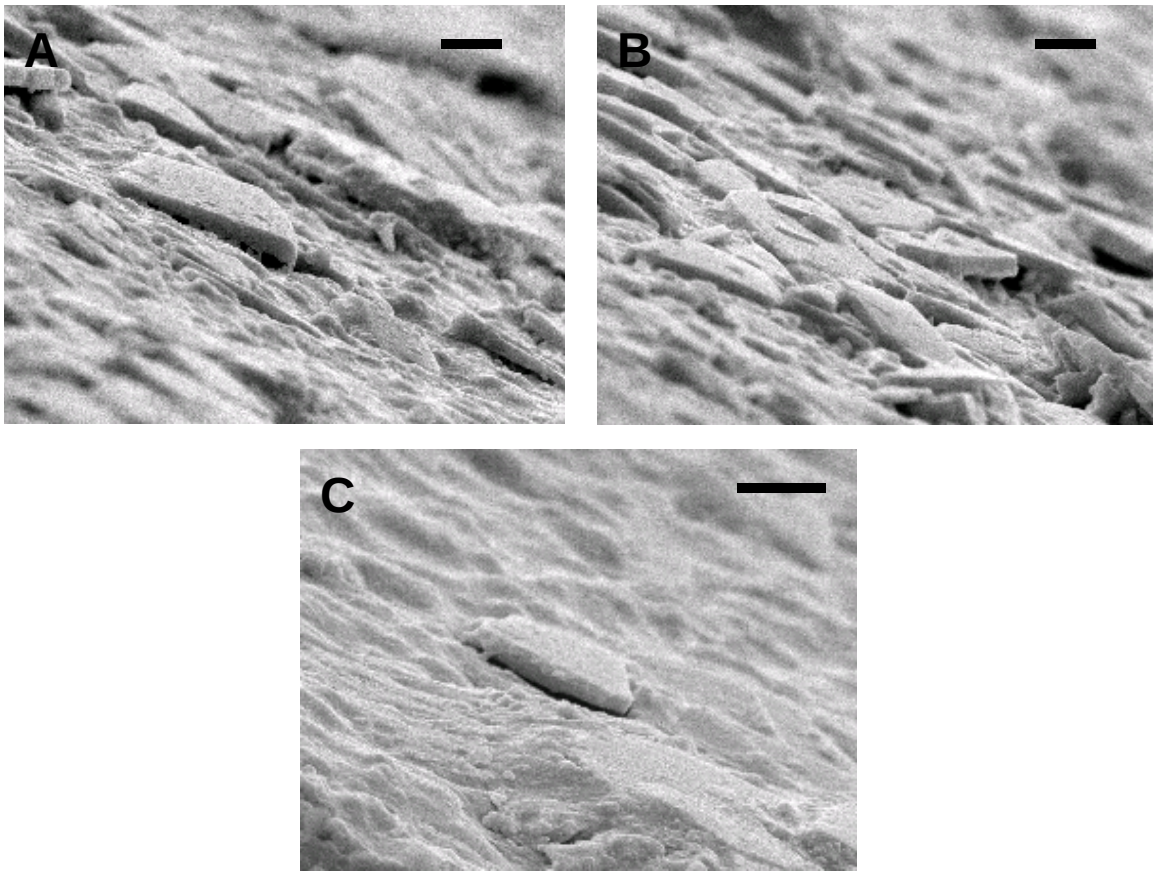

Figure 4.6: Tilted-view SEM images of a calcined silica film deposited by slip coating on top of a dC5-silicalite-1 particulate coating. All scale bars are 1 μm.

The defective nature of the slip coating-deposited films was further supported by permeation measurements. Figure 4.7 shows the permeation characteristics of five different films that were formed by depositing three alternating layers of dC5-silicalite-1 and slip coated silica onto silica-coated porous supports. Though silicalite-1 has been shown to be selective for *para*- over *ortho*-xylene [73, 130-134], Figure 4.7B and D illustrate that these films showed negligible selectivity for this system. The microstructure of the films, as revealed by SEM, is one very plausible explanation for this behavior. It should be stated that, had the films been free of defects, high separation performance can not be guaranteed because these are mixed matrix – not continuous – films. A severe mismatch between the matrix and flake permeabilities

could also cause very poor separation performance, no matter how good the microstructure, as we have seen in previous chapters.

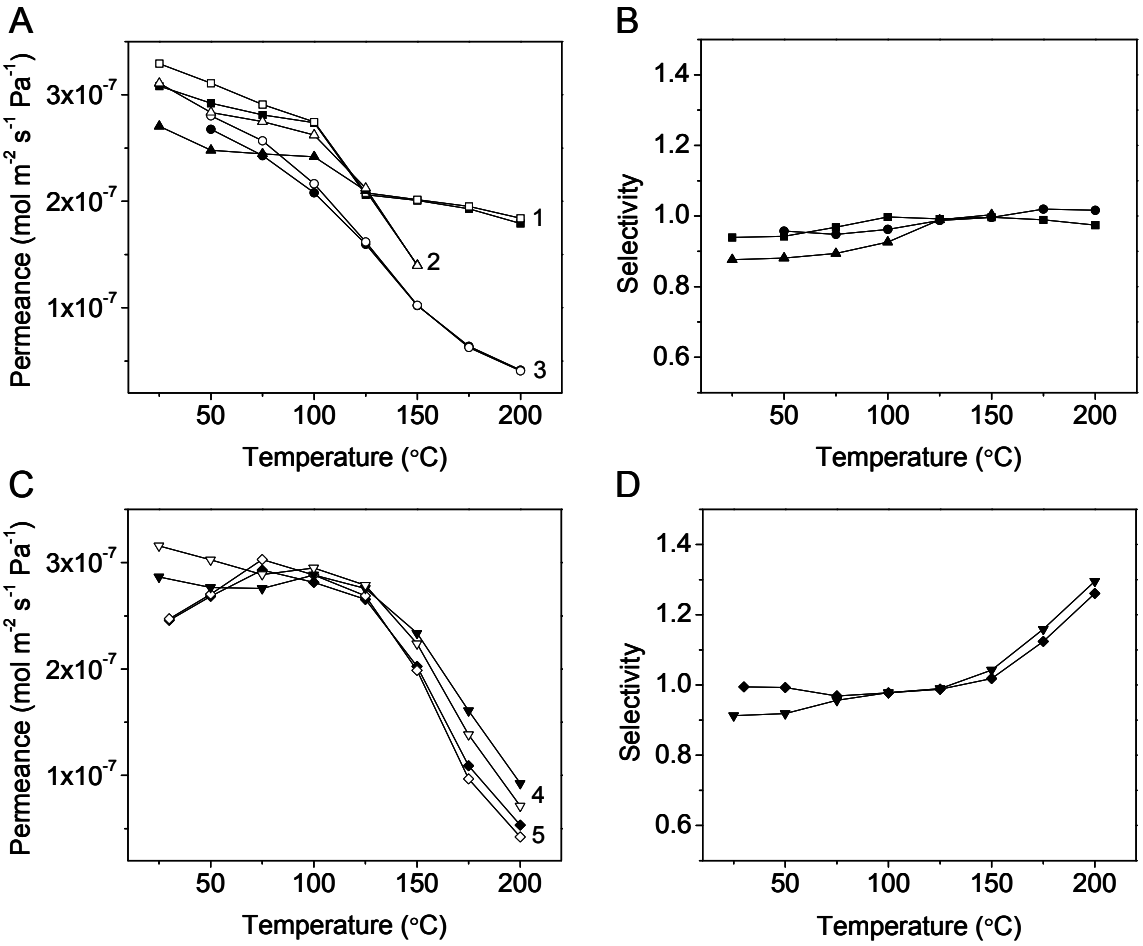

Figure 4.7: Permeance (A, C) and selectivity (C, D) of five silica/dC5-silicalite-1 films formed by successive slip coating of silica on top of zeolite particulate films. Open symbols are for *ortho*-xylene and filled symbols are for *para*-xylene. The particle layers in films 1-3 were formed using 0.05 g zeolite/40 mL toluene in the deposition step. Films 4 and 5 were formed using 0.1 g zeolite/40 mL toluene. All films consist of three alternating layers of zeolite and silica on top of a silica-coated porous support.

The SEM images of the slip coating-deposited silica layers suggests that a thicker deposit of silica is necessary to properly cover the silicalite-1 particle coating and seal any spaces created by less-than-perfect bonding between the particles and the support beneath. This is a challenge for the slip coating approach because the final film thickness is controlled by the amount of sol that "sticks" to the support when it is

immersed in and slipped away from the sol. Manipulation of sol viscosity by controlling the amount of dilution is one possible way to approach this, though the already imprecise nature of the sol formulation procedure poses a challenge to this approach. Aerosol and spray coating are methods that offer more direct control over the amount of sol deposited, and these were explored as alternatives to slip coating for formation of the silica layer.

Deposition of silica by aerosol coating

Figure 4.8 shows several examples of silica films deposited by aerosol coating, using the Brij-56-templated silica sol. The images in Figure 4.8A, C, E, and F are of uncalcined films, from which it can be seen that more complete coverage than that observed for slip coating can be achieved. Figure 4.8C and F both show silica coatings that cover the particulate coating and mostly fill in the gaps between particles. While the thickness of the silica layer seems acceptable in terms of providing good coverage of the particles, the drawbacks of this method are evident in Figure 4.8B and D, where calcined films are shown. Calcination can lead to excessive cracking and even pealing off of the silica layer, as seen in Figure 4.8B. Even when widespread peeling off of the silica layer is avoided, cracking around the perimeter of the coated particles is prevalent, as seen in Figure 4.8D. Figure 4.8F illustrates that even for an uncalcined film, cracking of the silica layer around the perimeter of the silicalite-1 particles can be a problem. Finally, Figure 4.8E illustrates the problems caused when an intergrown silicalite-1 particle is deposited as part of the film. Even when the silica layer is thick enough to cover the plate-like particles, large intergrowths protrude above the film surface, and these protrusions are likely to interfere with subsequent particle and silica layers and serve as nucleation sites for cracks and other defects.

The main problem with the aerosol-deposited films is excessive cracking, as illustrated in Figure 4.8. This is likely related to the thickness of the films, but it is possible that the Brij-56-templated silica itself could play a role. Unfortunately, the

CTAB-templated silica sol is ethanol-based, and is not amenable to aerosolization like the aqueous Brij-56-templated sol is.

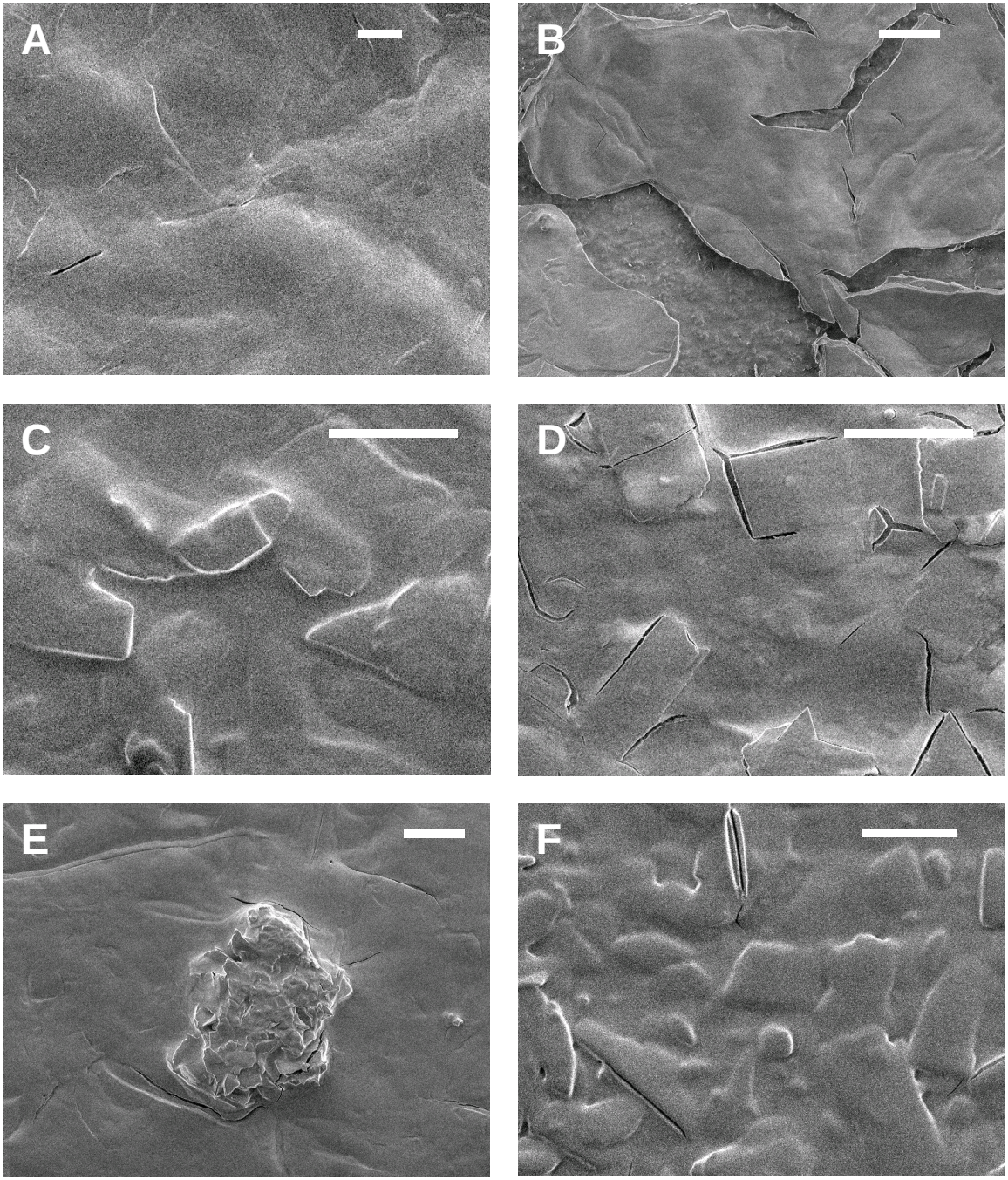

Figure 4.8: SEM images of silica coatings deposited by aerosol deposition on top of dC5-silicalite-1 particulate coatings. A, C are uncalcined films and B, D are the corresponding films following calcination. E, F are two more examples of uncalcined films. The scale bars are all 5 μm.

Deposition of silica by spray coating

Like aerosol coating, spray coating allows for direct control of the amount of silica deposited on the support. Moreover, spray coating allows the use of the ethanol-based CTAB-templated surfactant. Figure 4.9 shows three films formed by spray coating the CTAB-templated silica sol onto silicalite-1-coated supports. Figure 4.9A, C, and E, the uncalcined films, show that an appropriate amount of particle coverage can be achieved by this method. However, each of these images shows some intergrowths that protrude above the level of the silica layer. Also, some cracking is evident in Figure 4.9A and C. Following calcination, the cracking in D and F becomes more severe, with peeling off of the silica layer evident in Figure 4.9F.

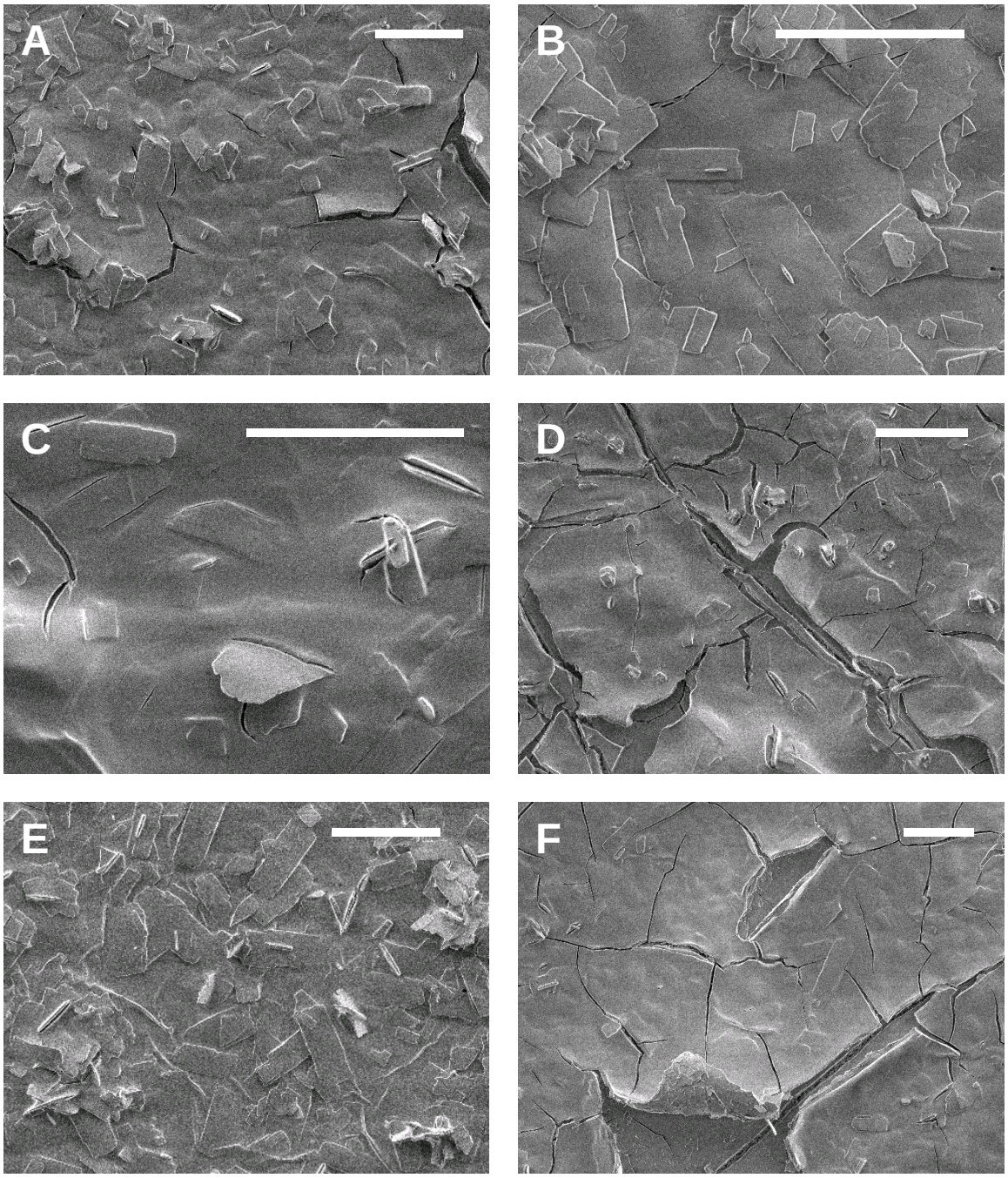

Figure 4.9: SEM images of silica films deposited by spray coating on top of dC5-silicalite-1 particulate coatings. A, C, and E are uncalcined films and B, D, and F are the corresponding films following calcination. The scale bars are all 10 μm.

4.5. Conclusions

Oriented coatings of very high aspect ratio silicalite-1 particles were formed on porous supports with good coverage and with [*0h0*] being the dominant orientation perpendicular to the support surface. Covering these particulate coatings with mesoporous silica was attempted in an effort to form mesoporous silca/silicalite-1 mixed matrix membranes through a layer-by-layer approach. Slip coating, aerosol coating, and spray coating were explored as possible approaches for deposition of the silica layer. The slip coating method was unsuccessful because the deposited silica layer was too thin to completely cover the particulate layer. While the aerosol and spray methods offer more direct control over the thickness of the silica layer, films formed by these approaches showed severe cracking and peeling off upon calcination. Furthermore, while the majority of the silicalite-1 particles in the particulate coating are high aspect ratio plates, the deposition of a small number of large intergrown particles could not be avoided, and these are not easily covered by the thin silica layer which is appropriate for covering the rest of the film.

Chapter 5. Synthesis of layered Aluminophosphates

5.1. Abstract

Layered aluminophosphates have the potential to provide high aspect ratio molecular sieve particles that could provide selectivity when included in mixed matrix membranes. The individual layers that stack up to form these crystalline materials contain apertures that are on the order of the size of small molecules. If these layers could be exfoliated without structural rearrangement within the layer, they would be candidates for the "selective flake" phase in mixed matrix membranes. Because these flakes would be about 1 nm thick, they could be appropriate for use in ultra-thin asymmetric polymer membranes, which are widely used for gas separation. In this chapter, I report synthesis studies of three layered aluminophosphates found in the literature. By changing synthesis time and/or composition, unknown phases result. One unknown phase appears as a mixture with the literature material, one is of low crystallinity, and one has been isolated and swollen with surfactant.

5.2. Introduction

Aluminophosphates are structurally similar to zeolites, but while zeolites are oxides of aluminum and silicon, aluminophosphates contain aluminum and phosphorous. The first porous aluminophosphate materials to be reported were built up from strict alternation of aluminum and phosphorous-centered tetrahedra – AlO_4 and PO_4 [135]. These 3D framework materials are electrically neutral and generally stable to calcination. Known as $AlPO_4$'s, these materials, like aluminosilicate zeolites, have found use as adsorbents and catalysts [136]. In addition to these neutral framework materials, further research has lead to the discovery of many materials with aluminum to phosphorous ratios less than one. Non-unity aluminum to phosphorous ratios are made possible by diverse coordination of the aluminum and phosphorous centers. For example, aluminophosphate materials have been reported that include 4-, 5-, and 6-coordinated aluminum centers, while only 4-coordinated aluminum is seen in $AlPO_4$'s.

Likewise, while phosphorous is always connected to four aluminum centers (through bridging oxygen atoms) in $AlPO_4$ materials, Al/P < 1 materials are known that contain phosphorous centers that are connected to 1, 2, 3, and 4, aluminum centers. These numerous coordination chemistries result in rich structural diversity in aluminophosphate materials – including 3D framework, 2D layer, 1D chain, and 0D cluster structures.

The class of 2D layered aluminophosphates has proven particularly fertile for the discovery of new materials. Numerous reports of layered aluminophosphates with unique structures and chemical compositions have appeared (see review by Yu and Xu and references therein [137]). These materials consist of anionic aluminophosphate sheets held together by electrostatic attractions between themselves and charge-balancing cations located in the gallery space between the layers. The layers themselves contain apertures formed by rings of the aluminum- and phosphorous-centered polyhedra. Depending on the number of polyhedra that make up the apertures, they are on the order of the size of small molecules. The existence of these apertures and the large number of available materials make layered aluminophosphates attractive candidates for use as the selective phase in mixed matrix membranes.

Like clays, some layered aluminophosphates can accommodate guest molecules into the gallery space between layers. Jeong *et al.* reported the swelling of a layered aluminophosphate with cetyltrimethylammonium bromide surfactant [18]. Intercalation of n-alkylamines and aromatic amines into layered aluminophosphates via a process that includes exfoliation and re-stacking of the aluminophosphate layers has been claimed [138-141]. Intercalation of n-alkylamines into layered aluminophosphates in a one-step sonication-assisted method was reported by Peng *et al.* [142]. Based on experience with the formation of polymer/clay composites, it is anticipated that these kinds of intercalation steps will precede the formation of polymer/aluminophosphate composites.

Almost all of the reported 2D layered aluminophosphates form large crystals, on the order of hundreds of microns. This is convenient for structure solution by single crystal x-ray diffraction, but is not ideal for use in mixed-matrix membranes. It is anticipated that swelling and exfoliation of layered materials will be more easily accomplished with smaller crystals, as the inner gallery space of small crystals will be more accessible to intercalates than the same space in larger crystals. While post-synthesis particle size reduction (for example, by grinding) is a possible solution, synthesis of monodisperse crystallites on the order of 1 micron would be ideal.

In this chapter, I explore the synthesis of three layered aluminophosphates reported in the literature by varying synthesis variables such as composition and digestion time, with an eye toward the synthesis of small crystallites. These synthesis studies resulted in new, unknown aluminophosphate phases which are characterized by scanning electron microscopy and powder x-ray diffraction. In one case the unknown phase has been successfully isolated and swollen with CTAB surfactant. Of the other two materials, one appears as a mixture with another phase, and the other appears to be of low crystallinity.

5.3. Experimental

Synthesis

The typical components of an aluminophosphate synthesis mixture include: (i.) an aluminum source, (ii.) a phosphorous source, (iii.) a structure directing agent, and (iv.) a solvent. In all syntheses reported here, the aluminum was supplied by aluminum tri-isopropoxide (98+%, Aldrich), and the phosphorous by phosphoric acid (85 wt% in water, Sigma-Aldrich). The structure directing agent – an organic molecule whose presence is necessary for the crystallization of the material – varied among the three synthesis recipes explored and included ethylamine (70% in water, Fluka), racemic 1,2-diaminopropane (99%, Acros), and racemic isopropanolamine (93%, Aldrich). The solvent also varied among the three syntheses and included ethylene glycol (99+%, Sigma-Aldrich), n-butanol (99.4+%, Aldrich), and water (deionized).

In a typical synthesis, the aluminum tri-isopropoxide and structure directing agent were added to a polyethylene bottle containing the solvent and the mixture was stirred until homogeneous (as long as overnight). Then the phosphoric acid was added dropwise with stirring, and the resulting synthesis mixture was placed in Teflon®-lined stainless steel autoclaves and digested quiescently in a synthesis oven at 180°C. At the end of digestion, the bombs were quenched in water, and the solid products were recovered either by filtration and washing with DI water or by multiple (at least three) centrifugations and re-dispersals in DI water. Finally, solids were dried in air in an 80°C drying oven. The three synthesis studies reported here were based on aluminophosphate materials reported in the literature. The molar recipes for these materials are given in Table 5.1, and the synthesis time and temperature are given in Table 5.2.

Table 5.1: Identities and molar amounts for the materials these synthesis studies were based upon. In LAlPO-3, isopropanolamine served as both the SDA and solvent.

LAlPO-X	$Al(i\text{-}PrO)_3$	H_3PO_4	SDA	Solvent
1 [143]	1	2	3 1,2-diaminopropane	139 Water
2 [144]	1	3	12 ethylamine	28 ethylene glycol / 28 n-butanol
3 [145]	1	1.67	51 isopropanolamine	None

Table 5.2: Synthesis conditions for the materials that these synthesis studies were based upon.

	Synthesis Temperature (°C)	Synthesis Time (days)
1 [143]	180	2
2 [144]	180	13
3 [145]	180	6

Swelling

For swelling, 0.5 g of cetyltrimethylammonium bromide (99%, Sigma) was dissolved in 40 mL of DI water with the aid of sonication. 0.2 g of the synthesized aluminophosphate powder was then added, and the mixture was sonicated for 45 minutes. The solids were recovered by centrifugation and re-dispersal in DI water three times and were dried in air in an 80°C drying oven.

Characterization

The powder x-ray diffraction (XRD) data was collected on Seimens D5005 diffractometer with a Cu source in a $\theta/2\theta$ geometry. Scanning electron microscope images were obtained using a JEOL 6500 FEG SEM. Samples were Pt-coated before imaging. Small angle x-ray scattering (SAXS) was performed with a SAXSess instrument (Anton PaarGmbH) with Cu-Kα radiation. Elemental composition was determined by inductively coupled plasma (ICP) analysis, performed by Galbraith Labs is Atlanta, Georgia.

5.4. Results and Discussion

LAlPO-1

The synthesis of LAlPO-1 was explored by holding the recipe constant and varying the reaction time between 2 and 12 days. The XRD results are summarized in Figure 5.1. These results are for two separate synthesis attempts, labeled (i) and (ii). These attempts were identical in terms of reagents used and molar recipe followed; they differed only in that they were conducted on different days. As can be seen by comparing the 2-day samples from (i) and (ii), the reproducibility of these syntheses was not good. Furthermore, none of the samples agree very well with the published powder XRD pattern of the expected product.

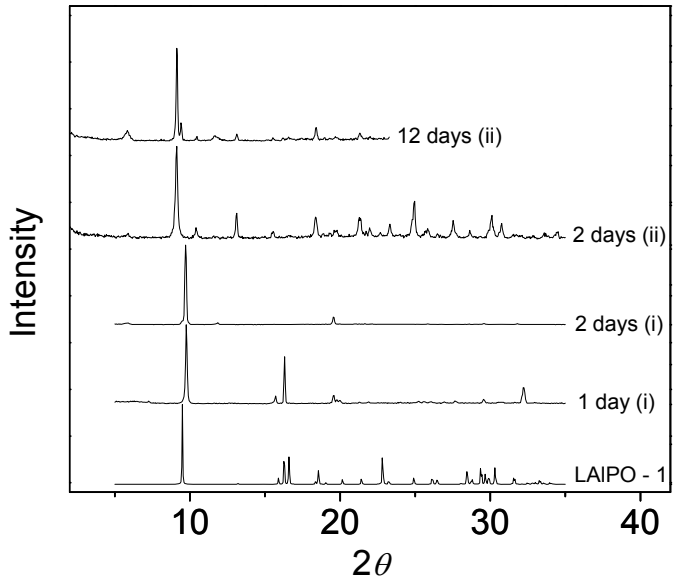

Figure 5.1: Normalized powder x-ray diffraction patterns of the products of syntheses based on the recipe for LAlPO-1 and the simulated powder pattern based on the reported single-crystal structure solution for the expected product [143]. Reaction times are shown beside the respective curves. Two separate synthesis gels were prepared and the resulting products are indicated by (i) and (ii).

Selected SEM images of the products of these syntheses are given in Figure 5.2. Figure 5.2a,b shows that the product of the 2 day (i) synthesis consists mainly of large, needle-like crystals, but that there is a minority product in the form of agglomerated, flake-like particles with a largest dimension of around 5 microns. Though the agglomeration is problematic, the flake-like morphology of these particles is close to ideal for use in mixed matrix membranes. The product of the 2 day (ii) synthesis also shows small plate-like and larger particles, as shown in Figure 5.2b,c, though the morphology of both is different from those obtained from the 2 day (i) synthesis. Finally, after 12 days, the relative amount of small, plate-like particles appears to be increased, as shown in Figure 5.2e and, especially, f.

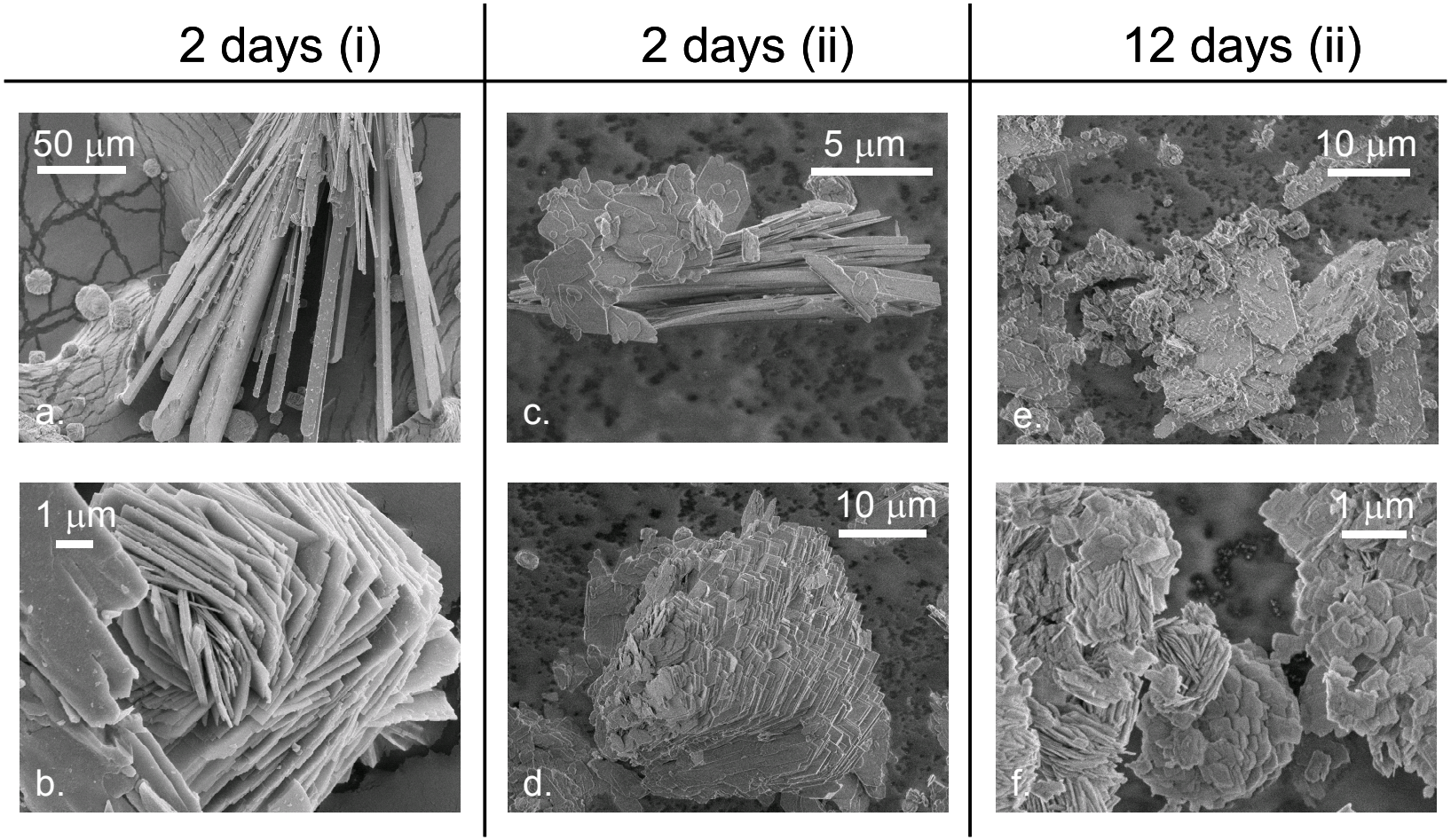

Figure 5.2: SEM images of the products of syntheses based on the recipe for LAlPO-1 as a function of reaction time. Two separate synthesis gels were prepared and the resulting products are indicated by (i) and (ii).

The imperfect match between any of the obtained powder x-ray diffraction patterns and that expected based on the reported structure makes these synthesis attempts less than ideal. On the other hand, the crystal morphology of the small, plate-like phase is desirable for the intended application – mixed matrix membranes. If the plate-like particles could be isolated, a structure solution might be of interest due to their potential use in mixed matrix membranes.

LAlPO-2

The use of LAlPO-2 to form a mixed matrix membrane for gas separations has been reported by our group [18]. Therefore, the synthesis of this material is of particular interest. Figure 5.3 shows the composition of the reported synthesis mixture for this material as well as many other compositions that were explored as part of this work. The ternary plot gives the mole fraction of solvent (a 50/50 mixture of ethylene glycol and n-butanol), SDA (ethylamine), and aluminum source (with Al/P ratio held constant) on the three axes.

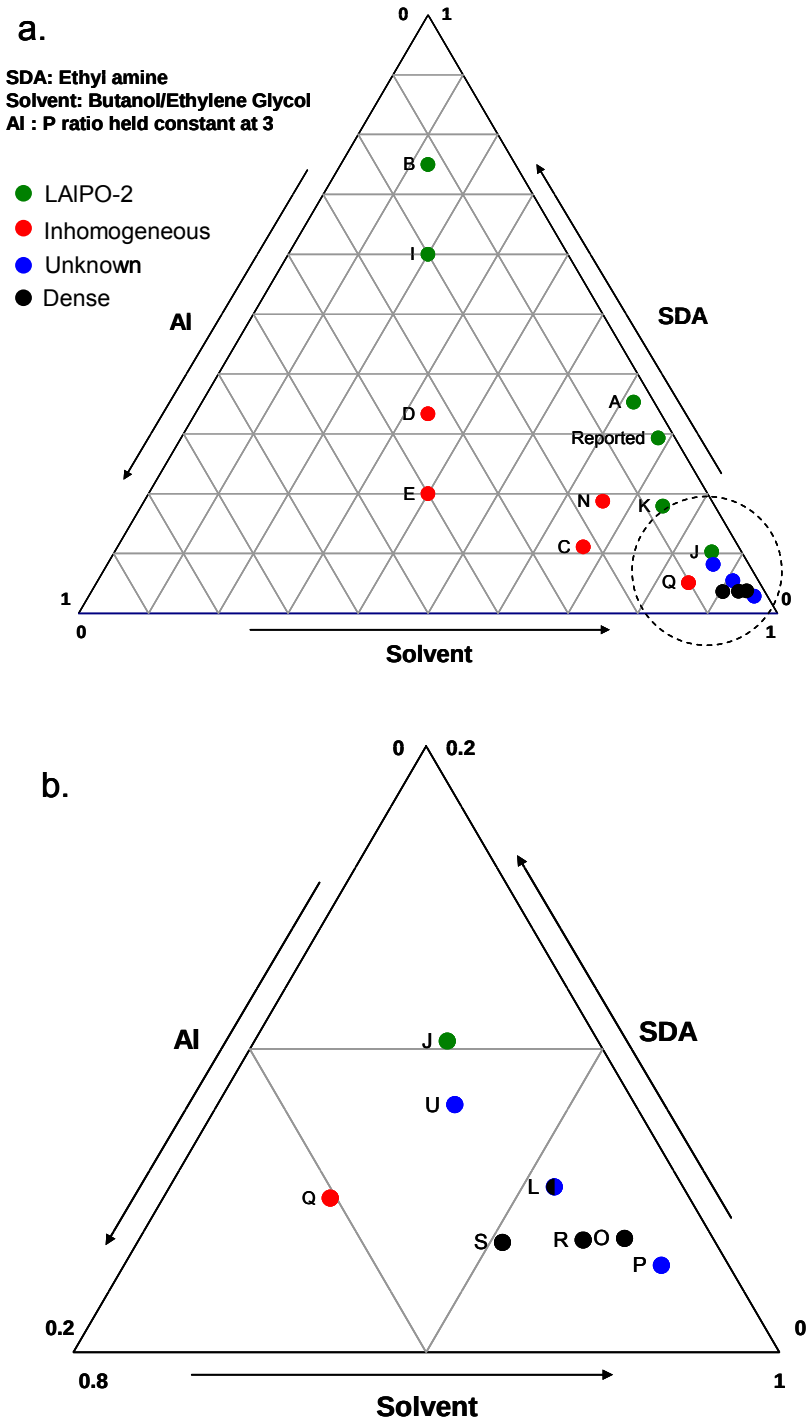

Figure 5.3: Molar composition (in terms of solvent, SDA, and Al) of synthesis mixtures explored, where the components are those used in the synthesis of LAlPO-2. Green points (A, B, I, and J) resulted in a product that was similar to LAlPO-2 by powder XRD, red points (C, D, E, N, and Q) represent synthesis mixtures which were phase separated (solid/liquid) before digestion, blue points (L, U, and P) resulted in an unknown phase, and black points (L, O, R, and S) resulted in a dense phase. The area highlighted by the circle in a. is magnified in b.

As Figure 5.3 suggests, exploration of the synthesis mixture composition lead to changes in the powder x-ray diffraction patterns of the products. These changes are shown in Figure 5.4, where the XRD patterns of the products, classified as LAlPO-2, unknown phase, and dense phase, are given. The labels in Figure 5.4 correspond to the labels given in Figure 5.3.

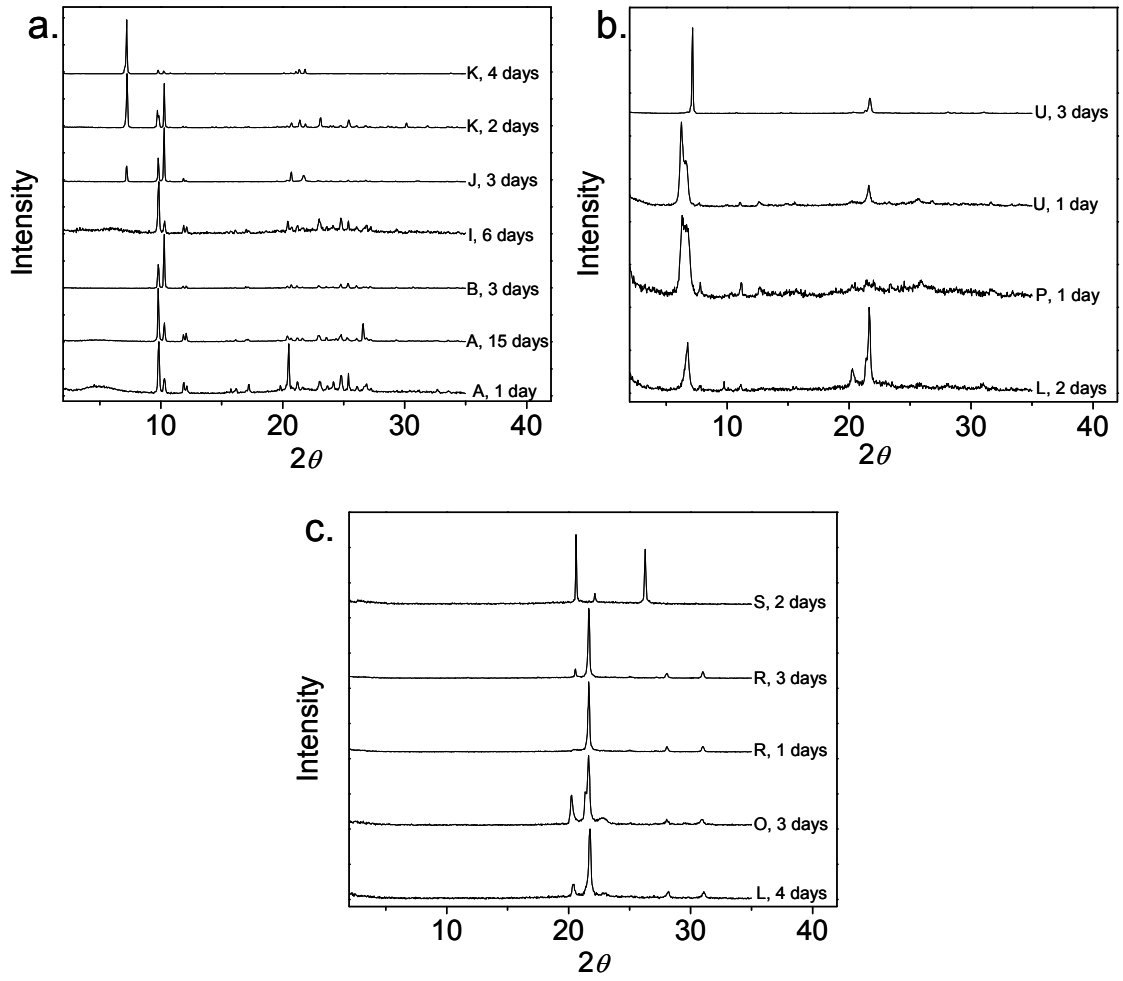

Figure 5.4: Powder x-ray diffraction patterns of the products of the synthesis mixtures shown in Figure 5.3. The synthesis time of each product at 180°C is given on the plot. The materials are classified as: a.) LAlPO-2, b.) unknown phase, and c.) dense phase.

As can be seen in Figure 5.4a, as the synthesis mixture composition strays from the reported value, especially for dilute (solvent-rich) recipes, a low-angle peak ($2\theta \approx 7$) becomes more and more prominent. For very dilute recipes, the characteristic peaks of the reported material do not appear, and the low angle peak becomes very

prominent, as shown in Figure 5.4b. On the other hand, as Figure 5.4c shows, very dilute recipes can also result in the crystallization of a dense phase, characterized by no peaks at $2\theta < 20°$.

The changes in crystal structure illustrated by Figure 5.4 are accompanied by changes in crystal size and shape, as shown by the SEM images in Figure 5.5. The crystals shown in Figure 5.5a,b are characteristic of LAlPO-2, with an intergrown rectangular shape and size on the order of 100 μm. The unknown material, shown in Figure 5.5c,d forms aggregates (tens of microns in size) of plate-like particles of a few microns in size. Finally, the dense phases form ~50 μm particles, with surfaces that can be either smooth or rough.

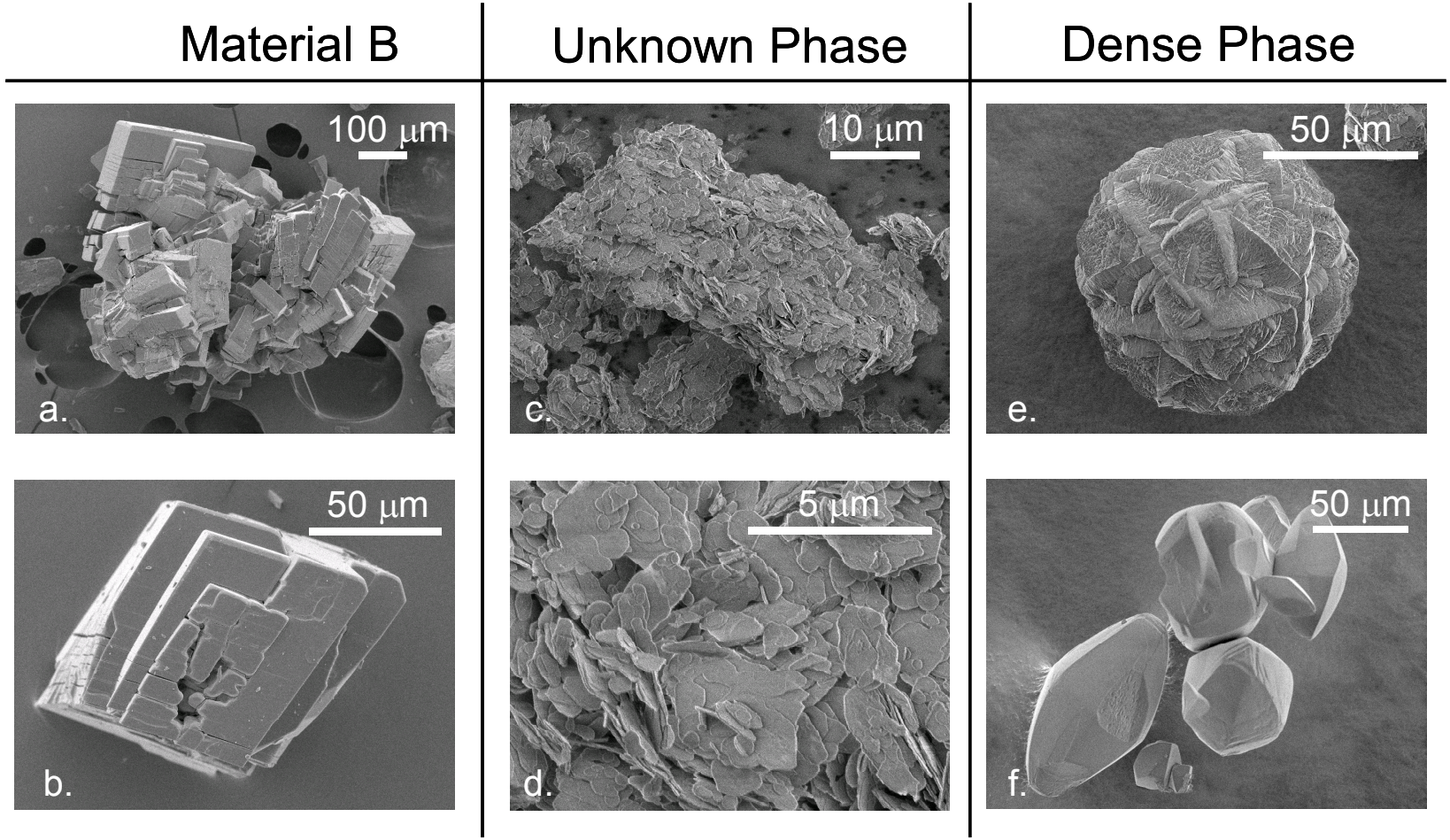

Figure 5.5: Representative SEM images of the products of the syntheses shown in Figure 5.3. The images correspond to the XRD patterns labeled: (a., b.) A, 15 days; (c., d.) L, 2 days; (e.) O, 3 days; and (f.) S, 2 days.

Like in the case of LAlPO-1, the unknown material from this synthesis study also forms what appear to be small plate-like particles. The powder XRD results for these materials include few peaks, with the most intense, low-angle peak often appearing broad. This could be evidence of low-symmetry in this unknown material. Further synthesis work is necessary to determined if a pure phase with a full set of peaks can be synthesized from this area of the recipe space. The small plate-like morphology of the products obtained thus far makes this material of some interest for potential use in mixed matrix membranes.

LAlPO-3

In the synthesis of LAlPO-3, isopropanolamine is used as both the solvent and SDA. Therefore, holding Al/P ratio constant, the only variable left in the synthesis mixture composition is the isopropanolamine/Al ratio. In this work, the isopropanolamine/Al ratio and the synthesis time were explored. Figure 5.6 shows the powder XRD patterns of the products of syntheses at the reported (given in Table 5.1) composition and various synthesis times. As can be seen, the obtained XRD patterns match reasonably well with the pattern calculated based on the single-crystal structure solution given in the original report [145] (the curve labled LAlPO-3 in Figure 5.6). The peak positions are matching, but the intensities evolve with synthesis time, with the peak at $2\theta = 9.8$ (the [003] peak) becoming ever more intense.

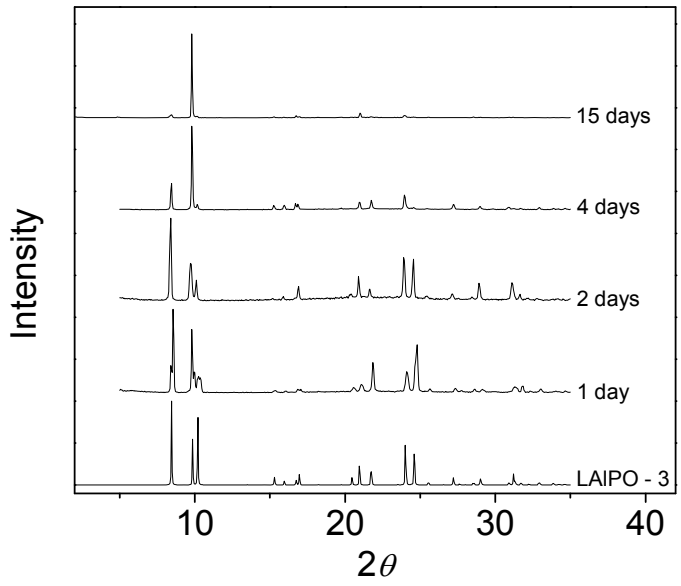

Figure 5.6: Powder XRD for the products of syntheses carried out with the LAlPO-3 recipe given in Table 5.1 as a function of synthesis time. The bottom curve is the calculated powder pattern of the material reported in the literature.

The crystal morphology of this material is shown in Figure 5.7, where it can be seen that, like the other layered aluminophosphates, this material forms crystals on the order of 100 μm in size.

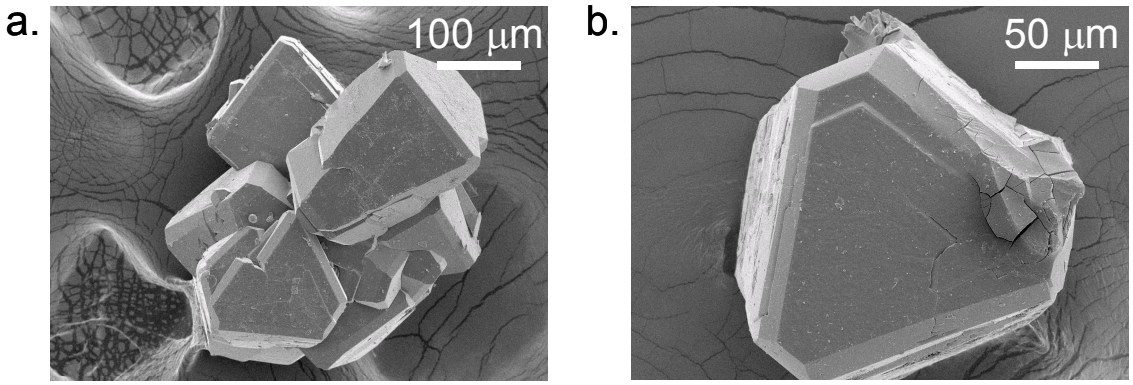

Figure 5.7: SEM images of the products synthesized from a mixture corresponding to the LAlPO-3 recipe. Synthesis times are: (a.) 1 day and (b.) 4 days.

Changing the isopropanolamine/Al ratio has a significant effect on the synthesis products at short reaction times, as shown in the XRD data of Figure 5.8. As this figure shows, when the isopropanolamine/Al ratio is decreased from 51 (in the original recipe)

to 25, a new phase is crystallized at short-to-moderate synthesis times. This new phase appears to be mixed with some LAlPO-3 material, as the magnified portion of the 1-day synthesis product XRD pattern highlights. After 15 days, the product transforms to LAlPO-3.

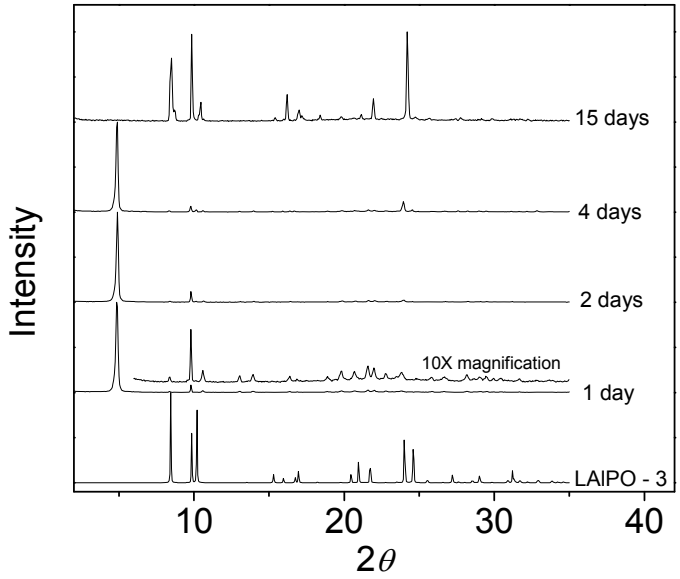

Figure 5.8: Powder XRD patterns for the products of syntheses based on the LAlPO-3 recipe, but with an isopropanolamine/Al ratio of 25. Synthesis times are indicated on the plot.

The crystal morphology of these synthesis products is shown in Figure 5.9. The unknown phase, crystallized after 1 and 4 days, is characterized by aggregated plate-like particles with a size of a few microns, as shown in Figure 5.9a-d. After 15 days, the crystal morphology changes to that of LAlPO-3.

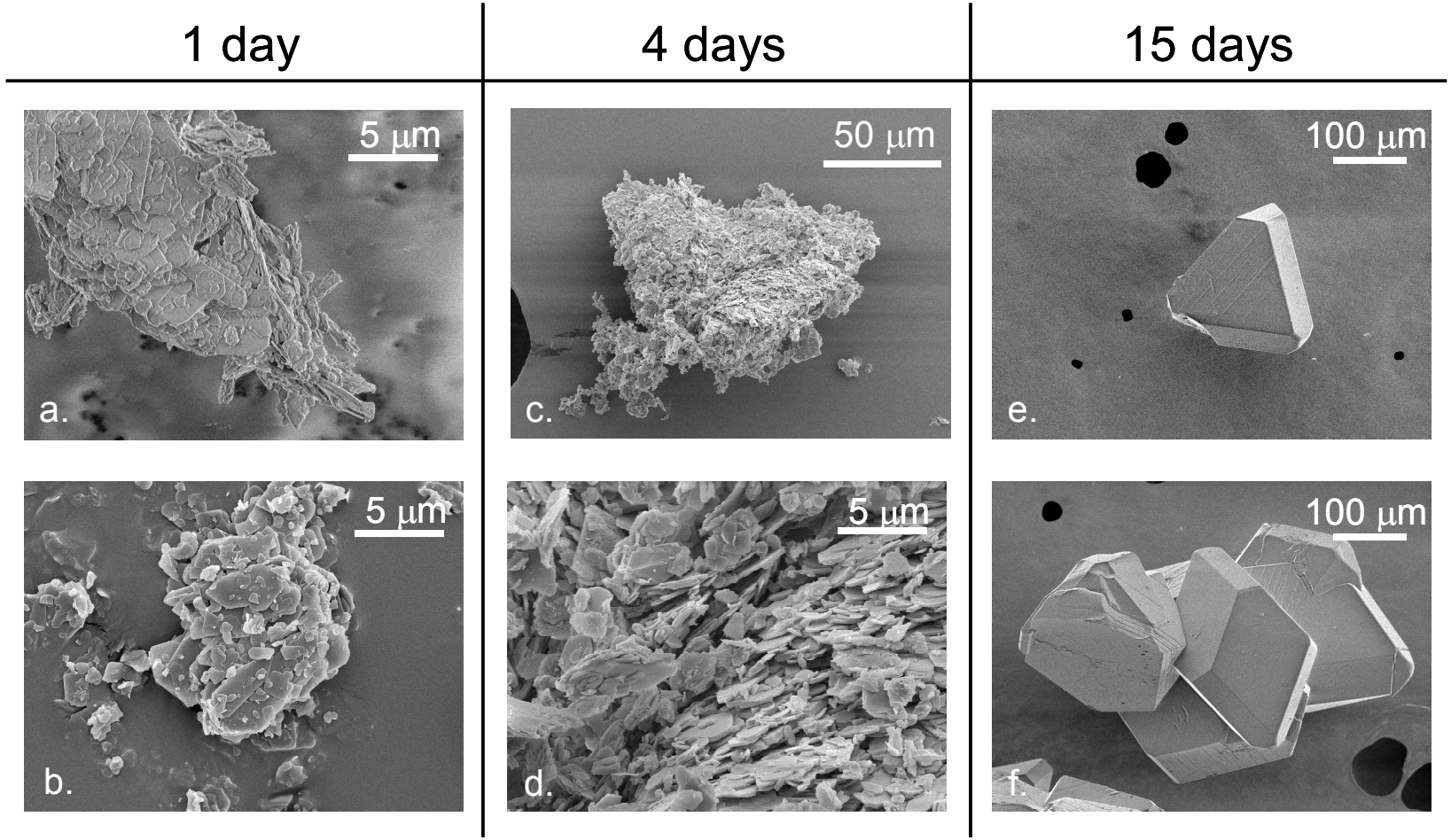

Figure 5.9: SEM images of the products of syntheses based on the LAlPO-3 recipe, but with an isopropanolamine/Al ratio of 25. Synthesis time is indicated on the figure.

While an isopropanolamine/Al ratio of 25 resulted in a mixture of LAlPO-3 and an unknown phase, an isopropanolamine/Al ratio of 35 yielded a purer unknown product. This is illustrated in Figure 5.10, where the powder XRD pattern of the product of a synthesis with isopropanolamine/Al = 35 is compared to that of a synthesis with isoporpanolamine/Al = 25. For isopropanolamine/Al = 35, the first two peaks of the LAlPO-3 material have disappeared, and many peaks that do not appear in LAlPO-3 are evident. Crystal morphology for this product is unchanged from that shown in Figure 5.9a-d.

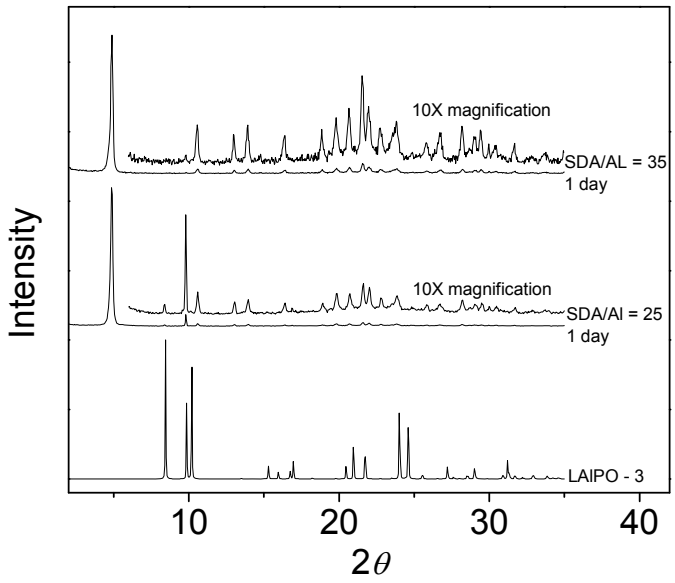

Figure 5.10: Powder XRD patterns of the products of syntheses based on the LAlPO-3 recipe, but with different isopropanolamine/Al ratios.

One day synthesis of a recipe with isopropanolamine/Al = 35 results in an apparently pure product with a crystal morphology characterized by micron-sized plate-like particles. As has been mentioned, this morphology is desirable for use in mixed matrix membranes. Also, this material shows many peaks in powder XRD, indicating high symmetry and making a structure solution, even from powder data, a potential possibility. For application in mixed matrix membranes, layered materials are desired, but without a structure solution we cannot be sure that this unknown product is layered.

It could be a 3D framework, 2D layered, 1D chain, or 0D cluster structure. One way to distinguish a 3D framework material from the lower dimensional structures is with surfactant intercalation. Lower dimensional materials can potentially accept guest molecules into their gallery spaces, expanding the unit cell. While 3D materials could possibly accept small molecules into their pore space, changes in the unit cell due to this would be small. Figure 5.11 shows the small angle x-ray scattering pattern of the unknown material following exposure to a solution of cetyltrimethylammonium bromide in water, as described in the Experimental section.

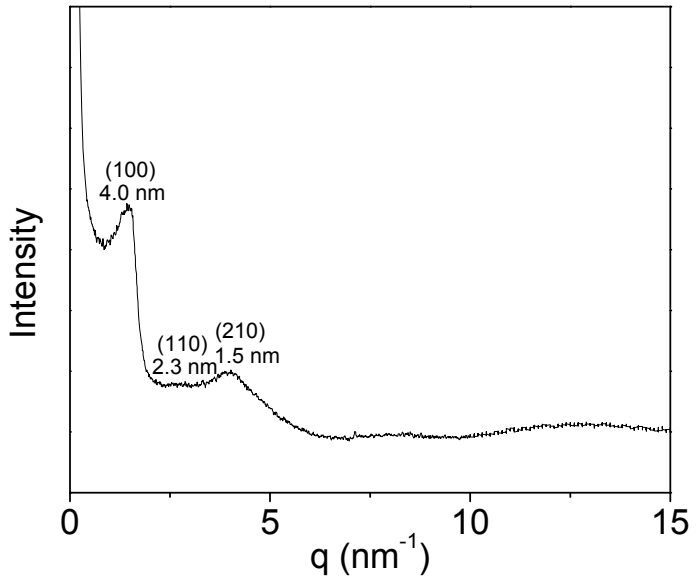

Figure 5.11: Small angle x-ray scattering from unknown LAlPO-3-related material swollen with CTAB surfactant. Peaks are labeled with their corresponding distances. The peaks are tentatively indexed according to a hexagonal arrangement of cylinders. This is one unit cell which is consistent with the pattern.

The characteristic peaks of the unknown material disappear upon contact with CTAB solution and new, lower-angle peaks appear. There are two obvious peaks corresponding to 4.0 and 1.5 nm and what could be a weak peak between them at 2.3 nm. These peaks can be indexed to a hexagonal unit cell, as shown on Figure 5.11. The fact that the unknown material can be swollen suggests that it is a lower-dimensional

structure. If the suggested hexagonal unity cell is correct, this could be consistent with a hexagonal packing of 1D AlPO chains with CTAB between the chains.

Elemental analysis indicates that the unknown material has an Al:P ratio of 1. This is in contrast to the LAlPO-3 material, which has an Al:P ratio of 3/4. The C:H:N composition of the unknown material is 9:32:3, while that of LAlPO-3 is 9:30:3. Layered materials with an Al:P ratio of 1 have been reported [143], but to our knowledge, no 1D or 0D materials with this Al:P ratio exist [137].

5.5. Conclusions

Three different materials with plate-like morphology and roughly micron size were crystallized from aluminophosphate synthesis mixtures. The products were obtained by manipulating the synthesis time and/or molar ratios of layered aluminophosphate recipes found in the literature. One material shows a full set of peaks in powder x-ray diffraction and has been swollen with cetyltrimethylammonium bromide surfactant. Of the other materials, one crystallizes as a mixture with another phase and the other shows limited crystallinity, as evidenced by powder x-ray diffraction peaks that are few in number and broad in shape. The characteristic morphology of these particles makes them interesting for use in mixed matrix membranes, but only if they are layered materials with appropriate apertures perpendicular to the layers. A full structure solution would provide this information.

Chapter 6. Closing Remarks

This dissertation has attempted to address a persistent and somewhat unrecognized obstacle to the development of mixed matrix membrane technology. While the literature in this area has seen many reports of mixed matrix membrane formation and microstructural characterization, with significant effort devoted to microstructural control, there has been little concern over mixed matrix membrane performance optimization through material design. The question of *how* to make a mixed matrix membrane has gotten much attention, while the question of *which* mixed matrix membrane to make has been relatively ignored. The latter is a question material design, and answering it requires accurate models for mixed matrix membrane performance.

Here I have presented a model for mixed matrix membrane performance that specifically addresses the most prominent class of mixed matrix membranes – those containing zeolite flakes. This model differs from its forebears in that it accounts for transport effects that are specifically relevant to diffusion in zeolites (and other microporous materials) – competitive adsorption and concentration-dependent diffusivities. It was shown that a model that accounts for these effects can yield predictions that are quantitatively and qualitatively different from those of models that do not. Because these effects are dependent on operating conditions (such as pressure), the importance of this modeling approach for process as well as material design was demonstrated.

Though the inclusion of competitive adsorption and concentration-dependent diffusivities was shown to be vital to the accurate prediction of the performance of mixed matrix membranes containing zeolite flakes, its rigorous application by numerical solution is impractical for routine use. In order to provide a tool that is widely accessible, I presented a semi-empirical approach to the prediction of mixed matrix membrane performance. This approach uses analytical equations for mixed matrix membrane performance that require constant matrix and flake permeabilities.

These permeabilities are obtained from one-dimensional solution of the Maxwell-Stefan equations for pure membranes of the flake materials at various operating conditions (feed pressure, feed composition, and permeate pressure) and are used for predicting the performance of mixed matrix membranes for which these operating conditions represent an average of what the flakes in a mixed matrix membrane would experience. The validity of this semi-empirical approach was tested by comparison with fully numeric calculations. Two case studies for experimentally relevant mixed matrix membranes were used to demonstrate the utility of this model for mixed matrix membrane design.

Guided by some of the modeling results, experimental attempts to fabricate mesoporous silica/silicalite-1 zeolite mixed matrix membranes were presented. A layer-by-layer approach was adopted, where zeolite particulate coatings and porous silica films are alternately deposited on a support to form a mixed matrix membrane. The formation of *b*-oriented particulate coatings of very high aspect ratio silicalite-1 particles with good coverage was described. Deposition of porous silica onto these coatings was explored by three different methods, but good coverage without cracking was not achieved.

Finally, the synthesis of layered aluminophosphates for potential use as selective flakes in mixed matrix membranes was described. The formation of micron-sized, plate-like particles was achieved by manipulating the synthesis conditions and recipes of three materials from the literature that normally crystallize as 100-micron particles. It is anticipated that monodisperse, micron-sized particles will be easier to use in ultra-thin polymer/selective flake mixed matrix membranes than either very large particles or polydisperse particles obtained from comminution of large particles.

Appendix A. Derivation of Select Equations

The derivation of Equations 2.28a,b are given here, beginning with the reproduction of Equations 2.27a,b:

$$-\rho \frac{b_1}{1+b_1 p_1 + b_2 p_2} \frac{dp_1}{dz} = \frac{N_1}{q_{1sat} D_1} \tag{A.1}$$

$$-\rho \frac{b_2}{1+b_1 p_1 + b_2 p_2} \frac{dp_2}{dz} = \frac{N_2}{q_{2sat} D_2} \tag{A.2}$$

These and subsequent equations can be made more compact by the introduction of the following non-dimensional variables:

$$\eta \equiv \frac{z}{z_{ii} - z_i} \tag{A.3}$$

$$\phi_i \equiv \frac{N_i \left(z_{ii} - z_i \right)}{\rho q_i^{sat} D_i} \tag{A.4}$$

$$\Pi_i \equiv b_i p_i \tag{A.5}$$

$$\Pi_t \equiv \Pi_1 + \Pi_2 \tag{A.6}$$

So that Equations 2.27a,b are written:

$$-\phi_1 = \left(\frac{1}{1+\Pi_t} \right) \frac{d\Pi_1}{d\eta} \tag{A.7a}$$

$$-\phi_2 = \left(\frac{1}{1+\Pi_t} \right) \frac{d\Pi_2}{d\eta} \tag{A.7b}$$

Summing Equations A.7a,b,

$$-\left(\phi_1+\phi_2\right)=\frac{1}{1+\Pi_t}\frac{d}{d\eta}\left(\Pi_1+\Pi_2\right)$$

$$-\phi_t=\frac{1}{1+\Pi_t}\frac{d\Pi_t}{d\eta} \qquad \text{A.8}$$

$$\text{where } \phi_t\equiv\phi_1+\phi_2$$

which is easily solved.

$$\ln\left(1+\Pi_t\right)=-\phi_t\eta+C_0$$

$$\left(1+\Pi_t\right)=C_1\exp\left(-\phi_t\eta\right) \qquad \text{A.9}$$

At $\eta=\eta_i$ $\Pi_t=\Pi_{t,i}$

$$\left(1+\Pi_{t,i}\right)=C_1\exp\left(-\phi_t\eta_i\right) \qquad \text{A.10}$$

$$\frac{\left(1+\Pi_t\right)}{\left(1+\Pi_{t,i}\right)}=\exp\left[-\phi_t\left(\eta-\eta_i\right)\right] \qquad \text{A.11}$$

At $\eta=\eta_{ii}$ $\Pi_t=\Pi_{t,ii}$

$$\frac{\left(1+\Pi_{t,ii}\right)}{\left(1+\Pi_{t,i}\right)}=\exp\left[-\phi_t\right] \qquad \text{A.12}$$

$$\frac{\left(\Pi_t-\Pi_{t,i}\right)}{\left(\Pi_{t,ii}-\Pi_{t,i}\right)}=\frac{\exp\left(-\phi_t\left(\eta-\eta_i\right)\right)-1}{\exp\left(-\phi_t\right)-1} \qquad \text{A.13}$$

It still remains to solve Equations A.7a,b, which is easy enough now that $\left(1+\Pi_t\right)$ is known through Equation A.11.

$$\frac{d\Pi_1}{d\eta}=-\phi_1\left(1+\Pi_{t,i}\right)\exp\left[-\phi_t\left(\eta-\eta_i\right)\right] \qquad \text{A.14}$$

$$\Pi_1 = \frac{\phi_1}{\phi_t}\left(1+\Pi_{t,i}\right)\exp\left[-\phi_t\left(\eta-\eta_i\right)\right]+C_2 \qquad \text{A.15}$$

At $\eta = \eta_i$ $\Pi_1 = \Pi_{1,i}$

$$\Pi_{1,i} = \frac{\phi_1}{\phi_t}\left(1+\Pi_{t,1}\right)+C_2 \qquad \text{A.16}$$

Subtracting A.16 from A.15:

$$\left(\Pi_1-\Pi_{1,i}\right) = \frac{\phi_1}{\phi_t}\left(1+\Pi_{t,i}\right)\left\{\exp\left[-\phi_t\left(\eta-\eta_i\right)\right]-1\right\} \qquad \text{A.17}$$

Likewise:

$$\left(\Pi_2-\Pi_{2,i}\right) = \frac{\phi_2}{\phi_t}\left(1+\Pi_{t,ii}\right)\left\{\exp\left[-\phi_t\left(\eta-\eta_i\right)\right]-1\right\} \qquad \text{A.18}$$

Evaluating at $\eta = \eta_{ii}$:

$$\frac{\left(\Pi_1-\Pi_{1,i}\right)}{\left(\Pi_{1,ii}-\Pi_{1,i}\right)} = \frac{\exp(-\phi_t\left(\eta-\eta_i\right))-1}{\exp(-\phi_t)-1} \qquad \text{A.19a}$$

$$\frac{\left(\Pi_2-\Pi_{2,i}\right)}{\left(\Pi_{2,ii}-\Pi_{2,i}\right)} = \frac{\exp(-\phi_t\left(\eta-\eta_i\right))-1}{\exp(-\phi_t)-1} \qquad \text{A.19b}$$

By the rearrangement of A.12, ϕ_t can be found.

$$\phi_t = \ln\left(\frac{1+\Pi_{t,i}}{1+\Pi_{t,ii}}\right) \qquad \text{A.20}$$

Given the pressures on the feed and permeate faces of the membrane, the pressure distribution within the membrane has been found. Substituting Equation A.20 into Equations A.19a,b, the pressure distribution is given by:

$$\Pi_1 = \left[\frac{\left(\frac{1+\Pi_{t,ii}}{1+\Pi_{t,i}} \right)^{(\eta-\eta_i)} - 1}{\left(\frac{1+\Pi_{t,ii}}{1+\Pi_{t,i}} \right) - 1} \right] \left(\Pi_{1,ii} - \Pi_{1,i} \right) + \Pi_{1,i} \qquad \text{A.21a}$$

$$\Pi_2 = \left[\frac{\left(\frac{1+\Pi_{t,ii}}{1+\Pi_{t,i}} \right)^{(\eta-\eta_i)} - 1}{\left(\frac{1+\Pi_{t,ii}}{1+\Pi_{t,i}} \right) - 1} \right] \left(\Pi_{2,ii} - \Pi_{2,i} \right) + \Pi_{2,i} \qquad \text{A.21b}$$

Substituting Equation A.21 into Equation A.7 yields the fluxes:

$$\begin{aligned}
-\phi_1 &= \left(\frac{1}{1+\Pi_t} \right) \frac{d\Pi_1}{d\eta} \\
-\phi_1 &= \left(\frac{1}{1+\Pi_{t,i}} \right) \exp\left[\phi_t \left(\eta - \eta_i \right) \right] \frac{d}{d\eta} \left\{ \left[\frac{\exp(-\phi_t \left(\eta - \eta_i \right)) - 1}{\exp(-\phi_t) - 1} \right] \left(\Pi_{1,ii} - \Pi_{1,i} \right) + \Pi_{1,i} \right\} \qquad \text{A.22} \\
-\phi_1 &= -\phi_t \left(\frac{\Pi_{1,ii} - \Pi_{1,i}}{1+\Pi_{t,i}} \right) \frac{\exp\left[\phi_t \left(\eta - \eta_i \right) \right]}{\exp(-\phi_t) - 1} \exp(-\phi_t \left(\eta - \eta_i \right)) \\
-\phi_1 &= -\left(\frac{\Pi_{1,ii} - \Pi_{1,i}}{1+\Pi_{t,i}} \right) \frac{\phi_t}{\exp(-\phi_t) - 1}
\end{aligned}$$

Which can be made simpler by substituting A.20.

$$-\phi_1 = -\left(\frac{\Pi_{1,ii} - \Pi_{1,i}}{1+\Pi_{t,i}} \right) \ln\left(\frac{1+\Pi_{t,i}}{1+\Pi_{t,ii}} \right) \frac{1}{\left(\frac{1+\Pi_{t,ii}}{1+\Pi_{t,i}} \right) - 1} \qquad \text{A.23}$$

$$\phi_1 = \left(\frac{\Pi_{1,ii} - \Pi_{1,i}}{\Pi_{t,ii} - \Pi_{t,i}}\right) \ln\left(\frac{1+\Pi_{t,i}}{1+\Pi_{t,ii}}\right) \quad \text{A.24a}$$

$$\phi_2 = \left(\frac{\Pi_{2,ii} - \Pi_{2,i}}{\Pi_{t,ii} - \Pi_{t,i}}\right) \ln\left(\frac{1+\Pi_{t,i}}{1+\Pi_{t,ii}}\right) \quad \text{A.24b}$$

Which can also be written dimensionally:

$$N_1 = \frac{\rho D_1 q_1^{sat}}{\left(z_{ii} - z_i\right)} \frac{b_1\left(p_{1,ii} - p_{1,i}\right)}{\left(b_1 p_{1,ii} + b_2 p_{2,ii}\right) - \left(b_1 p_{1,i} + b_2 p_{2,i}\right)} \ln\left(\frac{1 + b_1 p_{1,i} + b_2 p_{2,i}}{1 + b_1 p_{1,ii} + b_2 p_{2,ii}}\right) \quad \text{A.25a}$$

$$N_2 = \frac{\rho D_2 q_2^{sat}}{\left(z_{ii} - z_i\right)} \frac{b_2\left(p_{2,ii} - p_{2,i}\right)}{\left(b_1 p_{1,ii} + b_2 p_{2,ii}\right) - \left(b_1 p_{1,i} + b_2 p_{2,i}\right)} \ln\left(\frac{1 + b_1 p_{1,i} + b_2 p_{2,i}}{1 + b_1 p_{1,ii} + b_2 p_{2,ii}}\right) \quad \text{A.25b}$$

The species fractional loadings can be found from Equations A.19, A.11, and 2.22.

$$\theta_1 = \left\{\left[\frac{\exp\left(-\phi_t\left(\eta - \eta_i\right)\right) - 1}{\exp\left(-\phi_t\right) - 1}\right]\left(\Pi_{1,ii} - \Pi_{1,ii}\right) + \Pi_{1,i}\right\} \frac{1}{\left(1 + \Pi_{t,i}\right)} \exp\left(\phi_t\left(\eta - \eta_i\right)\right) \quad \text{A.26a}$$

$$\theta_2 = \left\{\left[\frac{\exp\left(-\phi_t\left(\eta - \eta_i\right)\right) - 1}{\exp\left(-\phi_t\right) - 1}\right]\left(\Pi_{2,ii} - \Pi_{2,i}\right) + \Pi_{2,i}\right\} \frac{1}{\left(1 + \Pi_{t,i}\right)} \exp\left(\phi_t\left(\eta - \eta_i\right)\right) \quad \text{A.26b}$$

Or, substituting Equation A.20,

$$\theta_1 = \left\{\left[\frac{\left(\frac{1+\Pi_{t,ii}}{1+\Pi_{t,i}}\right)^{(\eta-\eta_i)} - 1}{\left(\frac{1+\Pi_{t,ii}}{1+\Pi_{t,i}}\right) - 1}\right]\left(\Pi_{1,ii} - \Pi_{1,i}\right) + \Pi_{1,i}\right\} \frac{1}{\left(1 + \Pi_{t,i}\right)} \left(\frac{1+\Pi_{t,i}}{1+\Pi_{t,ii}}\right)^{(\eta-\eta_i)} \quad \text{A.27a}$$

$$\theta_2 = \left\{ \left[\frac{\left(\frac{1+\Pi_{t,ii}}{1+\Pi_{t,i}} \right)^{(\eta-\eta_i)} - 1}{\left(\frac{1+\Pi_{t,ii}}{1+\Pi_{t,i}} \right) - 1} \right] \left(\Pi_{2,ii} - \Pi_{2,i} \right) + \Pi_{2,i} \right\} \frac{1}{\left(1+\Pi_{t,i}\right)} \left(\frac{1+\Pi_{t,i}}{1+\Pi_{t,ii}} \right)^{(\eta-\eta_i)} \qquad \text{A.27b}$$

Appendix B. Diffusivity of Nitrogen and Methane in Microporous Silica

The paper by Moon and co-workers contained measured values for single-component equilibrium adsorption parameters, q_i^{sat}, b_i, but diffusivities were not explicitly given. However, single-component permeation data through membranes of TPABr silica was given as a function of feed pressure. Though the experimental setup was not described in sufficient detail to determine the conditions of the permeate side of the membrane, it was assumed that the permeate was at vacuum.

According to the authors, permeation through this membrane consisted of three contributions: surface diffusion, Knudsen diffusion, and viscous flow. Each of these effects has a different dependence on pressure drop, so the permeation data was fit to the following general form:

$$N_i = \frac{\rho q_i^{sat} D_i}{L} \ln\left(1 + b_i p_{feed}\right) + C_{Knudson} p_{feed} + C_{Poiseuille} p_{feed}^2 \qquad \text{B.1}$$

The coefficients for Knudsen and Poiseuille flow were held constant for both gases (nitrogen and methane). For Knudsen diffusion, this coefficient should go as the square root of molecular weight, but the current purposes, the approximation that $C_{Knudsen}$ is not a function of the diffusant was deemed acceptable. For Poiseuille flow, the coefficient should vary with gas viscosity, and the approximation that this is constant between nitrogen and methane was adopted. Results of the fitting are given in Figure B.1.

Once the data was fit with Equation B.1, the coefficients for the logarithmic term were used to extract the diffusivities, using the appropriate physical parameters (ρ, q_i^{sat}) and an assumed thickness of the membrane (L) of 1μm. Included in Figure A-1 are curves for the portion of the flux due only to Maxwell-Stefan diffusion. This is the flux that would be expected for a perfect, defect-free membrane.

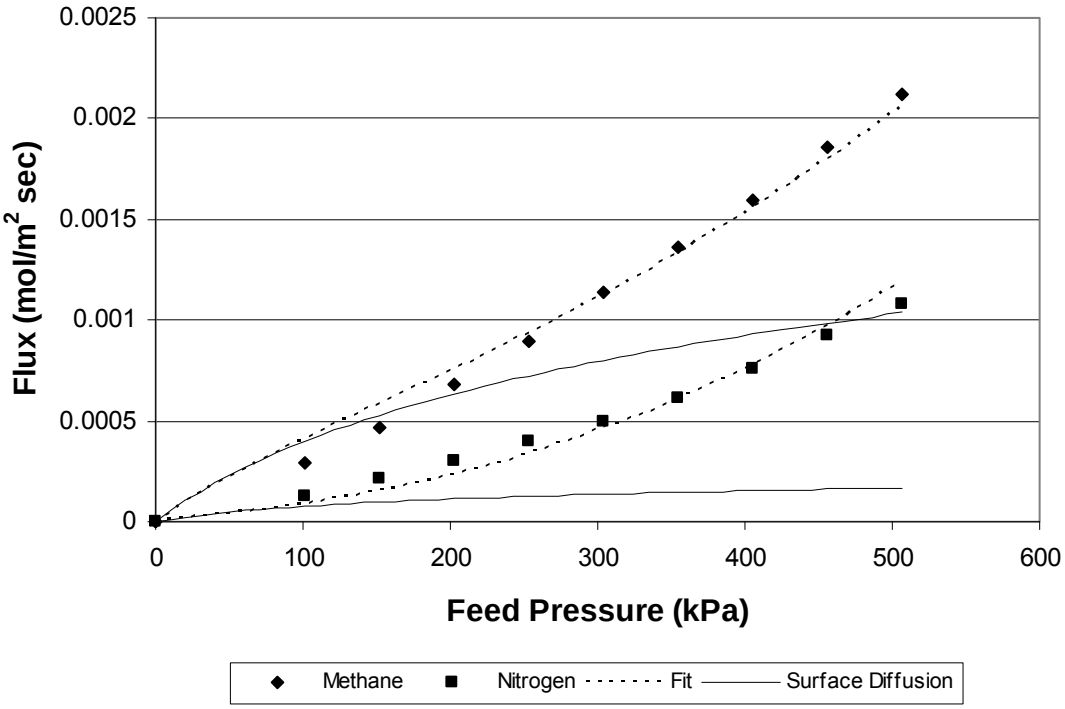

Figure B.1: Flux through microporous silica membrane reported by Moon *et al.* [71]. The data of Moon *et al.* is shown by closed symbols, while the dashed lines show a fit to the data that contains flux due to three mechanisms: viscous flow, Knudsen diffusion, and surface diffusion. Because we are only interested in surface diffusion (defect-free membranes), the solid lines shows this contribution to the overall flux.

Bibliography

1. Cussler, E.L., *Membranes containing selective flakes.* Journal of Membrane Science, 1990. **52**(3): p. 275-88.
2. Kemp, D.R. and D.R. Paul, *Gas sorption in polymer membranes containing adsorptive fillers.* Journal of Polymer Science: Polymer Physics Edition, 1974. **12**(3): p. 485-500.
3. Kulprathipanja, S., R.W. Neuzil, and N.N. Li, *Separation of fluids by means of mixed matrix membranes* 1988: US.
4. Paul, D.R. and D.R. Kemp, *The diffusion time lag in polymer membranes containing adsorptive fillers.* Journal of Polymer Science: Polymer Symposia, 1973. **41**(1): p. 79-93.
5. te Hennepe, H.J.C., et al., *Zeolite-filled silicone rubber membranes : Part 1. Membrane preparation and pervaporation results.* Journal of Membrane Science, 1987. **35**(1): p. 39.
6. Jia, M., K.-V. Peinemann, and R.-D. Behling, *Molecular sieving effect of the zeolite-filled silicone rubber membranes in gas permeation.* Journal of Membrane Science, 1991. **57**(2-3): p. 289.
7. Jia, M.-D., K.-V. Pleinemann, and R.-D. Behling, *Preparation and characterization of thin-film zeolite-PDMS composite membranes.* Journal of Membrane Science, 1992. **73**(2-3): p. 119.
8. Duval, J.M., et al., *Adsorbent filled membranes for gas separation. Part 1. Improvement of the gas separation properties of polymeric membranes by incorporation of microporous adsorbents.* Journal of Membrane Science, 1993. **80**(1): p. 189.
9. Gur, T.M., *Permselectivity of zeolite filled polysulfone gas separation membranes.* Journal of Membrane Science, 1994. **93**(3): p. 283.
10. Suer, M.G., N. Bac, and L. Yilmaz, *Gas permeation characteristics of polymer-zeolite mixed matrix membranes.* Journal of Membrane Science, 1994. **91**(1-2): p. 77.
11. Duval, J.M., et al., *Preparation of zeolite filled glassy polymer membranes.* Journal of Applied Polymer Science, 1994. **54**(4): p. 409-418.
12. te Hennepe, H.J.C., et al., *Zeolite-filled silicone rubber membranes Experimental determination of concentration profiles.* Journal of Membrane Science, 1994. **89**(1-2): p. 185.
13. Yong, H.H., et al., *Zeolite-filled polyimide membrane containing 2,4,6-triaminopyrimidine.* Journal of Membrane Science, 2001. **188**(2): p. 151.
14. Miller, S.J., et al., *Purification of p-xylene using composite mixed matrix membranes*. 2002, (Chevron U.S.A. Inc., USA; Medal, L.P.). Application: US. p. 12 pp.
15. Mahajan, R., et al., *Challenges in forming successful mixed matrix membranes with rigid polymeric materials.* Journal of Applied Polymer Science, 2002. **86**(4): p. 881-890.

16. Mahajan, R. and W.J. Koros, *Mixed matrix membrane materials with glassy polymers. Part 2.* Polymer Engineering & Science, 2002. **42**(7): p. 1432-1441.
17. Vu, D.Q., W.J. Koros, and S.J. Miller, *Mixed matrix membranes using carbon molecular sieves: I. Preparation and experimental results.* Journal of Membrane Science, 2003. **211**(2): p. 311.
18. Jeong, H.-K., et al., *Fabrication of Polymer/Selective-Flake Nanocomposite Membranes and Their Use in Gas Separation.* Chemistry of Materials, 2004. **16**(20): p. 3838-3845.
19. Clarizia, G., C. Algieria, and E. Drioli, *Filler-polymer combination: a route to modify gas transport properties of a polymeric membrane.* Polymer, 2004. **45**(16): p. 5671-5681.
20. Li, Y., et al., *The effects of polymer chain rigidification, zeolite pore size and pore blockage on polyethersulfone (PES)-zeolite A mixed matrix membranes.* Journal of Membrane Science, 2005. **260**(1-2): p. 45.
21. Hu, C.-C., et al., *Zeolite-filled PMMA composite membranes: influence of coupling agent addition on gas separation properties.* Desalination, 2006. **193**(1-3): p. 14.
22. Huang, Z., et al., *Enhanced gas separation properties by using nanostructured PES-Zeolite 4A mixed matrix membranes.* Journal of Applied Polymer Science, 2006. **101**(6): p. 3800-3805.
23. Sen, D., H. Kalipcilar, and L. Yimaz, *Development of polycarbonate based zeolite 4A filled mixed matrix gas separation membranes.* Journal Of Membrane Science, 2007. **303**(1-2): p. 194-203.
24. Husain, S. and W.J. Koros, *Mixed matrix hollow fiber membranes made with modified HSSZ-13 zeolite in polyetherimide polymer matrix for gas separation.* Journal of Membrane Science, 2007. **288**(1-2): p. 195-207.
25. Choi, S., et al., *Layered silicates by swelling of AMH-3 and nanocomposite membranes.* Angewandte Chemie - International Edition, 2008. **47**(3): p. 552-555.
26. Choi, S., et al., *Fabrication and gas separation properties of polybenzimidazole (PBI)/nanoporous silicates hybrid membranes.* Journal of Membrane Science, 2008. **316**(1-2): p. 145-152.
27. Woo, M., J. Choi, and M. Tsapatsis, *Poly(1-trimethylsilyl-1-propyne)/MFI composite membranes for butane separations.* Microporous and Mesoporous Materials, 2008. **110**(2-3): p. 330-338.
28. Wang, J.T., et al., *Effect of zeolites on chitosan/zeolite hybrid membranes for direct methanol fuel cell.* Journal of Power Sources, 2008. **178**(1): p. 9-19.
29. Vaughan, B.R. and E. Marand, *Transport properties of polymer-aluminophosphate nano-composites prepared by simple mixing.* Journal of Membrane Science, 2008. **310**(1-2): p. 197-207.
30. Wang, H.T., B.A. Holmberg, and Y.S. Yan, *Homogeneous polymer-zeolite nanocomposite membranes by incorporating dispersible template-removed zeolite nanocrystals.* Journal of Materials Chemistry, 2002. **12**(12): p. 3640-3643.

31. Pechar, T.W., et al., *Preparation and characterization of a poly(imide siloxane) and zeolite L mixed matrix membrane.* Journal of Membrane Science, 2006. **277**(1-2): p. 210-218.
32. Pechar, T.W., et al., *Fabrication and characterization of polyimide-zeolite L mixed matrix membranes for gas separations.* Journal of Membrane Science, 2006. **277**(1-2): p. 195-202.
33. Bein, T., et al., *Molecular-sieve sensors for selective detection at the nanogram level.* Journal Of The American Chemical Society, 1989. **111**(19): p. 7640-7641.
34. Kong, C.L., et al., *Thin carbon-zeolite composite membrane prepared on ceramic tube filter by vacuum slip casting for oxygen/nitrogen separation.* Carbon, 2007. **45**(14): p. 2848-2850.
35. Mulder, M., *Basic principles of membrane technology*. 2nd ed. 1996, Dordrecht ; Boston: Kluwer Academic. 564 p.
36. Robeson, L.M., *Correlation of separation factor versus permeability for polymeric membranes.* Journal of Membrane Science, 1991. **62**(2): p. 165-85.
37. Baker, R.W., *Future Directions of Membrane Gas Separation Technology.* Industrial & Engineering Chemistry Research, 2002. **41**(6): p. 1393-1411.
38. Chung, T.S., et al., *Mixed matrix membranes (MMMs) comprising organic polymers with dispersed inorganic fillers for gas separation.* Progress in Polymer Science, 2007. **32**(4): p. 483-507.
39. Zimmerman, C.M., A. Singh, and W.J. Koros, *Tailoring mixed matrix composite membranes for gas separations.* Journal of Membrane Science, 1997. **137**(1-2): p. 145.
40. Barrer, R.M. and J.H. Petropoulos, *Diffusion in heterogeneous media: lattices of parallelepipeds in a continuous phase.* British Journal of Applied Physics, 1961. **12**: p. 691-7.
41. Davis, H.T., *The Effective Medium Theory of Diffusion In Composite Media.* Journal of the American Ceramic Society, 1977. **60**(11-12): p. 499-501.
42. Petropoulos, J.H., *A Comparative Study of Approaches Applied to the Permeability of Binary Composite Polymeric Materials.* Journal of Polymer Science: Polymer Physics Edition, 1985. **23**(7): p. 1309-1324.
43. Gonzo, E.E., M.L. Parentis, and J.C. Gottifredi, *Estimating models for predicting effective permeability of mixed matrix membranes.* Journal of Membrane Science, 2006. **277**(1-2): p. 46-54.
44. Pal, R., *Permeation models for mixed matrix membranes.* Journal of Colloid and Interface Science, 2008. **317**(1): p. 191-198.
45. Li, S., et al., *High-Pressure CO2/CH4 Separation Using SAPO-34 Membranes.* Industrial & Engineering Chemistry Research, 2005. **44**(9): p. 3220-3228.
46. Martinek, J.G., et al., *Modeling Transient Permeation of Binary Mixtures through Zeolite Membranes.* Industrial & Engineering Chemistry Research, 2006. **45**(17): p. 6032-6043.
47. van den Broeke, L.J.P., *Simulation of diffusion in zeolitic structures.* AIChE Journal, 1995. **41**(11): p. 2399-2414.

48. Krishna, R. and J.A. Wesselingh, *The Maxwell-Stefan approach to mass transfer.* Chemical Engineering Science, 1997. **52**(6): p. 861-911.
49. Barrer, R.M. and J.H. Petropoulos, *Diffusion in heterogeneous media: lattice parallelepiped in continuous phase.* British Journal of Applied Physics, 1961. **12**: p. 691-7.
50. Maxwell, J.C., *Treatise on Electricity and Magnetism*. 1st ed. Vol. 1. 1873: Oxford: Clarendon Press.
51. Robeson, L.M., et al., *Physical property characteristics of polysulfone/poly-(dimethylsiloxane) block copolymers.* Angewandte Makromolekulare Chemie, 1973. **29**(1): p. 47-62.
52. Moore, T.T. and W.J. Koros, *Non-ideal effects in organic-inorganic materials for gas separation membranes.* Journal of Molecular Structure, 2005. **739**(1-3): p. 87.
53. Taylor, R. and R. Krishna, *Multicomponent mass transfer*. Wiley series in chemical engineering. 1993, New York: Wiley. xxxiv, 579 p.
54. Kapteijn, F., J.A. Moulijn, and R. Krishna, *The generalized Maxwell-Stefan model for diffusion in zeolites: sorbate molecules with different saturation loadings.* Chemical Engineering Science, 2000. **55**(15): p. 2923-2930.
55. Skoulidas, A.I., D.S. Sholl, and R. Krishna, *Correlation Effects in Diffusion of CH4/CF4 Mixtures in MFI Zeolite. A Study Linking MD Simulations with the Maxwell-Stefan Formulation.* Langmuir, 2003. **19**(19): p. 7977-7988.
56. Paschek, D. and R. Krishna, *Inter-relation between self- and jump-diffusivities in zeolites.* Chemical Physics Letters, 2001. **333**(3-4): p. 278.
57. Skoulidas, A.I. and D.S. Sholl, *Molecular Dynamics Simulations of Self-Diffusivities, Corrected Diffusivities, and Transport Diffusivities of Light Gases in Four Silica Zeolites To Assess Influences of Pore Shape and Connectivity.* Journal of Physical Chemistry A, 2003. **107**(47): p. 10132-10141.
58. Chempath, S., R. Krishna, and R.Q. Snurr, *Nonequilibrium molecular dynamics simulations of diffusion of binary mixtures containing short n-alkanes in faujasite.* Journal of Physical Chemistry B, 2004. **108**(35): p. 13481-13491.
59. van Baten, J.M. and R. Krishna, *Entropy effects in adsorption and diffusion of alkane isomers in mordenite: An investigation using CBMC and MD simulations.* Microporous and Mesoporous Materials, 2005. **84**(1-3): p. 179-191.
60. Krishna, R., et al., *Diffusion of CH4 and CO2 in MFI, CHA and DDR zeolites.* Chemical Physics Letters, 2006. **429**(1-3): p. 219.
61. Krishna, R. and J.M. van Baten, *Linking the loading dependence of the Maxwell-Stefan diffusivity of linear alkanes in zeolites with the thermodynamic correction factor.* Chemical Physics Letters, 2006. **420**(4-6): p. 545.
62. Auerbach, S.M., *Theory and simulation of jump dynamics, diffusion and phase equilibrium in nanopores.* International Reviews in Physical Chemistry, 2000. **V19**(2): p. 155.
63. Krishna, R., *A unified approach to the modeling of intraparticle diffusion in adsorption processes.* Gas Separation & Purification, 1993. **7**(2): p. 91-104.

64. Krishna, R. and R. Baur, *Analytic solution of the Maxwell-Stefan equations for multicomponent permeation across a zeolite membrane.* Chemical Engineering Journal (Amsterdam, Netherlands), 2004. **97**(1): p. 37-45.
65. Myers, A.L. and J.M. Prausnitz, *Thermodynamics of mixed-gas adsorption.* AIChE Journal, 1965. **11**(1): p. 121-7.
66. Rao, M.B. and S. Sircar, *Thermodynamic Consistency for Binary Gas Adsorption Equilibria.* Langmuir, 1999. **15**(21): p. 7258-7267.
67. Seader, J.D. and E.J. Henley, *Separation process principles*. 1998, Wiley: New York. p. p. 736.
68. Jayaraman, A., et al., *Tailored Clinoptilolites for Nitrogen/Methane Separation.* Industrial & Engineering Chemistry Research, 2005. **44**(14): p. 5184-5192.
69. Baerlocher, C. and L.B. McCusker, *Database of Zeolite Structures:* http://www.iza-structure.org/databases/. 2006.
70. Voltolini, M., G. Artioli, and M. Moret, *Molecular resolution images of the surfaces of natural zeolites by atomic force microscopy.* Microporous and Mesoporous Materials, 2003. **61**(1-3): p. 79.
71. Moon, J.H., et al., *Separation characteristics of tetrapropylammoniumbromide templating silica/alumina composite membrane in CO2/N-2, CO2/H-2 and CH4/H-2 systems.* Korean Journal Of Chemical Engineering, 2004. **21**(2): p. 477-487.
72. Xomeritakis, G., et al., *Organic-templated silica membranes: I. Gas and vapor transport properties.* Journal of Membrane Science, 2003. **215**(1-2): p. 225.
73. Lai, Z., et al., *Microstructural Optimization of a Zeolite Membrane for Organic Vapor Separation.* Science, 2003. **300**(5618): p. 456-460.
74. Shivaji, S., *Influence of adsorbate size and adsorbent heterogeneity of IAST.* AIChE Journal, 1995. **41**(5): p. 1135-1145.
75. Wu, P., A. Debebe, and Y.H. Ma, *Adsorption and diffusion of C6 and C8 hydrocarbons in silicalite.* Zeolites, 1983. **3**(2): p. 118.
76. Fredrickson, G.H. and J. Bicerano, *Barrier properties of oriented disk composites.* The Journal of Chemical Physics, 1999. **110**(4): p. 2181.
77. Krishna, R. and J.M. van Baten, *Diffusion of Alkane Mixtures in Zeolites: Validating the Maxwell-Stefan Formulation Using MD Simulations.* Journal of Physical Chemistry B, 2005. **109**(13): p. 6386-6396.
78. Bonilla, G., et al., *Zeolite (MFI) Crystal Morphology Control Using Organic Structure-Directing Agents.* Chem. Mater., 2004. **16**(26): p. 5697-5705.
79. Sheffel, J.A. and M. Tsapatsis, *A model for the performance of microporous mixed matrix membranes with oriented selective flakes.* Journal of Membrane Science, 2007. **295**(1-2): p. 50.
80. Reed, D.A. and G. Ehrlich, *SURFACE-DIFFUSION, ATOMIC JUMP RATES AND THERMODYNAMICS.* Surface Science, 1981. **102**(2-3): p. 588-609.
81. Krishna, R., D. Paschek, and R. Baur, *Modeling the occupancy dependence of diffusivities in zeolites.* Microporous and Mesoporous Materials, 2004. **76**(1-3): p. 233-246.

82. Krishna, R., et al., *Incorporating the loading dependence of the Maxwell-Stefan diffusivity in the modeling of CH4 and CO2 permeation across zeolite membranes.* Industrial & Engineering Chemistry Research, 2007. **46**(10): p. 2974-2986.
83. Li, S.G., et al., *Modeling permeation of CO2/CH4, CO2/N-2, and N-2/CH4 mixtures across SAPO-34 membrane with the maxwell-stefan equations.* Industrial & Engineering Chemistry Research, 2007. **46**(12): p. 3904-3911.
84. Krishna, R. and J.M. van Baten, *Insights into diffusion of gases in zeolites gained from molecular dynamics simulations.* Microporous and Mesoporous Materials, 2008. **109**(1-3): p. 91-108.
85. Myers, A.L. and J.M. Prausnitz, *Thermodynamics of mixed-gas adsorption.* AIChE Journal, 1965. **11**(1): p. 121-127.
86. Zhu, W., F. Kapteijn, and J.A. Moulijn, *Adsorption of light alkanes on silicalite-1: Reconciliation of experimental data and molecular simulations.* Physical Chemistry Chemical Physics, 2000. **2**(9): p. 1989.
87. Geier, O., et al., *Interference Microscopy Investigation of the Influence of Regular Intergrowth Effects in MFI-Type Zeolites on Molecular Uptake.* J. Phys. Chem. B, 2001. **105**(42): p. 10217-10222.
88. Pampel, A., et al., *New options for measuring molecular diffusion in zeolites by MAS PFG NMR.* Chemical Physics Letters, 2005. **407**(1-3): p. 53-57.
89. Kortunov, P., et al., *Influence of Defects on the External Crystal Surface on Molecular Uptake into MFI-Type Zeolites.* Chem. Mater., 2004. **16**(18): p. 3552-3558.
90. Zhu, W., et al., *Concentration-dependent diffusion of isobutane in silicalite-1 studied with the ZLC technique.* Chemical Engineering Science, 2004. **59**(18): p. 3827-3835.
91. Jiang, M. and M. Eic, *Transport properties of ethane, butanes and their binary mixtures in MFI-type zeolite and zeolite-membrane samples.* Adsorption - Journal of the International Adsorption Society, 2003. **9**(3): p. 225-234.
92. Hufton, J.R. and R.P. Danner, *Chromatographic Study of Alkanes in Silicalite: Transport Properties.* AIChE Journal, 1993. **39**(6): p. 962-974.
93. Shah, D.B., S. Chokchalacha, and D.T. Hayhurst, *Measurements of Transport Rates of C4 Hydrocarbons across a Single-crystal Silicalite Membrane.* Journal of the Chemical Society, Faraday Transactions, 1993. **89**(16): p. 3161-3167.
94. Bakker, W.J.W., et al., *Temperature dependence of one-component permeation through a silicalite-1 membrane.* AIChE Journal, 1997. **43**(9): p. 2203-2214.
95. Millot, B., et al., *Permeation of linear and branched alkanes in ZSM-5 supported membranes.* Microporous and Mesoporous Materials, 2000. **38**(1): p. 85.
96. Nijhuis, T.A., et al., *Measurement and modeling of the transient adsorption, desorption and diffusion processes in microporous materials.* Chemical Engineering Science, 1999. **54**(20): p. 4423-4436.

97. Runnebaum, R.C. and E.J. Maginn, *Molecular Dynamics Simulations of Alkanes in the Zeolite Silicalite: Evidence for Resonant Diffusion Effects.* J. Phys. Chem. B, 1997. **101**(33): p. 6394-6408.
98. Goodbody, S.J., et al., *Molecular Simulation of Methane and Butane in Silicalite.* Journal Of The Chemical Society, Faraday Transactions, 1991. **87**(13): p. 1951-1958.
99. June, R.L., A.T. Bell, and D.N. Theodorou, *Molecular dynamics studies of butane and hexane in silicalite.* J. Phys. Chem., 1992. **96**(3): p. 1051-1060.
100. Maginn, E.J., A.T. Bell, and D.N. Theodorou, *Dynamics of Long n-Alkanes in Silicalite: A Hierarchical Simulation Approach.* J. Phys. Chem., 1996. **100**(17): p. 7155-7173.
101. Shen, D., et al., *Diffusion of C4 Hydrocarbons in Silicalite-1.* Journal of the Chemical Society, Faraday Transactions, 1990. **86**(23): p. 3943-3948.
102. Hayhurst, D.T. and A.R. Paravar, *Diffusion of C-1 to C-5 normal paraffins in silicalite.* Zeolites, 1988. **8**(1): p. 27-29.
103. Heink, W., et al., *High-temperature Pulsed Field Gradient Nuclear-Magnetic-Resonance Self-diffusion Measurements of n-Alkanes in MFI-type Zeolites.* Journal Of The Chemical Society, Faraday Transactions, 1992. **88**(23): p. 3505-3509.
104. Jobic, H., *Diffusion of linear and branched alkanes in ZSM-5. A quasi-elastic neutron scattering study.* Journal of Molecular Catalysis A: Chemical, 2000. **158**(1): p. 135.
105. Gergidis, L.N. and D.N. Theodorou, *Molecular dynamics simulation of n-butane-methane mixtures in silicalite.* Journal of Physical Chemistry B, 1999. **103**(17): p. 3380-3390.
106. Talu, O., M.S. Sun, and D.B. Shah, *Diffusivities of n-alkanes in silicalite by steady-state single-crystal membrane technique.* AIChE Journal, 1998. **44**(3): p. 681-694.
107. Datema, K.P., et al., *Fourier-transform Pulsed-field-gradient H1 Nuclear Magnetic Resonance Investigation of the Diffusion of Light n-Alkanes in Zeolite ZSM-5.* Journal Of The Chemical Society, Faraday Transactions, 1991. **87**(12): p. 1935-1943.
108. Krishna, R. and J.M. van Baten, *Using molecular simulations for screening of zeolites for separation Of CO2/CH4 mixtures.* Chemical Engineering Journal, 2007. **133**(1-3): p. 121-131.
109. Hillock, A.M.W., S.J. Miller, and W.J. Koros, *Crosslinked mixed matrix membranes for the purification of natural gas: Effects of sieve surface modification.* Journal of Membrane Science, 2008. **314**(1-2): p. 193-199.
110. Raman, N.K., M.T. Anderson, and C.J. Brinker, *Template-based approaches to the preparation of amorphous, nanoporous silicas.* Chemistry of Materials, 1996. **8**(8): p. 1682-1701.
111. Bollmann, L., V.N. Urade, and H.W. Hillhouse, *Controlling Interfacial Curvature in Nanoporous Silica Films Formed by Evaporation-Induced Self-*

Assembly from Nonionic Surfactants. I. Evolution of Nanoscale Structures in Coating Solutions. Langmuir, 2007. **23**(8): p. 4257-4267.
112. Urade, V.N., et al., *Controlling Interfacial Curvature in Nanoporous Silica Films Formed by Evaporation-Induced Self-Assembly from Nonionic Surfactants. II. Effect of Processing Parameters on Film Structure.* Langmuir, 2007. **23**(8): p. 4268-4278.
113. Choi, J.Y., et al., *Layer-by-layer deposition of barrier and permselective c-Oriented-MCM-22/silica composite films.* Industrial & Engineering Chemistry Research, 2007. **46**(22): p. 7096-7106.
114. Lai, Z.P., M. Tsapatsis, and J.R. Nicolich, *Siliceous ZSM-5 membranes by secondary growth of b-oriented seed layers.* Advanced Functional Materials, 2004. **14**(7): p. 716-729.
115. Lu, Y.F., et al., *Continuous formation of supported cubic and hexagonal mesoporous films by sol gel dip-coating.* Nature, 1997. **389**(6649): p. 364-368.
116. Xomeritakis, G., et al., *Aerosol-assisted deposition of surfactant-templated mesoporous silica membranes on porous ceramic supports.* Microporous And Mesoporous Materials, 2003. **66**(1): p. 91-101.
117. Mabande, G.T.P., et al., *Preparation of b-oriented MFI films on porous stainless steel substrates.* Industrial & Engineering Chemistry Research, 2005. **44**(24): p. 9086-9095.
118. Ha, K., et al., *Facile assembly of zeolite monolayers on glass, silica, alumina, and other zeolites using 3-halopropylsilyl reagents as covalent linkers.* Advanced Materials, 2000. **12**(15): p. 1114-+.
119. Lee, J.S., et al., *Ultrasound-aided remarkably fast assembly of monolayers of zeolite crystals on glass with a very high degree of lateral close packing.* Advanced Materials, 2005. **17**(7): p. 837-+.
120. Lee, G.S., Y.J. Lee, and K.B. Yoon, *Layer-by-layer assembly of zeolite crystals on glass with polyelectrolytes as ionic linkers.* Journal of the American Chemical Society, 2001. **123**(40): p. 9769-9779.
121. Park, J.S., et al., *Organization of microcrystals on glass by adenine-thymine hydrogen bonding.* Journal of the American Chemical Society, 2002. **124**(45): p. 13366-13367.
122. Kulak, A., et al., *Polyamines as strong molecular linkers for monolayer assembly of zeolite crystals on flat and curved glass.* Journal of the American Chemical Society, 2000. **122**(38): p. 9308-9309.
123. Lee, J.S., et al., *Manual assembly of microcrystal monolayers on substrates.* Angewandte Chemie-International Edition, 2007. **46**(17): p. 3087-3090.
124. Laine, P., et al., *Convenient preparation of close-packed monograin layers of pure zeolite A microcrystals.* New Journal of Chemistry, 1997. **21**(4): p. 453-460.
125. Boudreau, L.C., J.A. Kuck, and M. Tsapatsis, *Deposition of oriented zeolite A films: in situ and secondary growth.* Journal of Membrane Science, 1999. **152**(1): p. 41-59.

126. Ban, T., et al., *Preparation of a completely oriented molecular sieve membrane.* Angewandte Chemie-International Edition, 1999. **38**(22): p. 3324-3326.
127. Lee, J.A., et al., *Colloidal crystal layers of hexagonal nanoplates by convective assembly.* Langmuir, 2006. **22**(12): p. 5217-5219.
128. Choi, J., et al., *MFI zeolite membranes from a- and randomly oriented monolayers.* Adsorption, 2006. **12**(5-6): p. 339-360.
129. Choi, J., et al., *Uniformly a-oriented MFI zeolite films by secondary growth.* Angewandte Chemie-International Edition, 2006. **45**(7): p. 1154-1158.
130. Hedlund, J., et al., *High-flux MFI membranes.* Microporous and Mesoporous Materials, 2002. **52**(3): p. 179-189.
131. Xomeritakis, G., Z.P. Lai, and M. Tsapatsis, *Separation of xylene isomer vapors with oriented MFI membranes made by seeded growth.* Industrial & Engineering Chemistry Research, 2001. **40**(2): p. 544-552.
132. Keizer, K., et al., *Two component permeation through thin zeolite MFI membranes.* Journal of Membrane Science, 1998. **147**(2): p. 159-172.
133. Gump, C.J., et al., *Aromatic permeation through crystalline molecular sieve membranes.* Industrial & Engineering Chemistry Research, 2001. **40**(2): p. 565-577.
134. Hedlund, J., et al., *A masking technique for high quality MFI membranes.* Journal of Membrane Science, 2003. **222**(1-2): p. 163-179.
135. Wilson, S.T., et al., *Aluminophosphate molecular sieves: a new class of microporous crystalline inorganic solids.* Journal of the American Chemical Society, 1982. **104**(4): p. 1146-1147.
136. Martens, J.A. and P.A. Jacobs, *Crystalline Microporous Phosphates: A Family of Versatile Catalysts and Adsorbents*, in *Studies in Sufrace Science and Catalysis, Vol. 85*, J.C. Jansen, et al., Editors. 1994.
137. Yu, J.H. and R.R. Xu, *Rich structure chemistry in the aluminophosphate family.* Accounts of Chemical Research, 2003. **36**(7): p. 481-490.
138. Wang, C., et al., *Delamination and aromatic amine intercalation of layered aluminophosphate with [Al3P4O16](3-) stoichiometry.* Journal of Colloid and Interface Science, 2005. **285**(2): p. 731-736.
139. Huang, Q., et al., *Delamination and intercalation of layered aluminophosphate with [Al3P4O16](3-) stoichiometry in water/alcohol/amine solutions.* Journal of Colloid and Interface Science, 2003. **257**(2): p. 268-275.
140. Wang, C., et al., *Controlled delamination and intercalation of layered microporous aluminophosphate by a novel two-step method.* Microporous and Mesoporous Materials, 2005. **84**(1-3): p. 297-301.
141. Huang, Q., et al., *Delamination and alkylamine intercalation of a layered microporous aluminophosphate [Al3P4O16][CH3(CH2)(3)NH3](3).* Microporous and Mesoporous Materials, 2004. **67**(2-3): p. 189-194.
142. Peng, L., et al., *Lamellar mesostructured aluminophosphates: Intercalation of n-alkylamines into layered aluminophosphate by ultrasonic method.* Chemistry of Materials, 2005. **17**(8): p. 2101-2107.

143. Yuan, H.-M., et al., *Synthesis and structural characterization of a new layered aluminophosphate [C3H12N2][Al2P2O8(OH)2].H2O.* Dalton, 2000(13): p. 1981-1984.
144. Gao, Q., et al., *Nonaqueous synthesis and characterization of a new 2-dimensional layered aluminophosphate [Al3P4O16]3-.3[CH3CH2NH3]+.* Journal of Solid State Chemistry, 1997. **129**(1): p. 37-44.
145. Yuan, H.-M., et al., *Dual Function of Racemic Isopropanolamine as Solvent and as Template for the Synthesis of a New Layered Aluminophosphate: [NH3CH2CH(OH)CH3]3.Al3P4O16.* Journal of Solid State Chemistry, 2000. **151**(1): p. 145-149.